Optique intégrée sur verre pour la génération de fréquences radio

Nisrine Arab

Communauté
UNIVERSITÉ Grenoble Alpes

THÈSE

Pour obtenir le grade de

DOCTEUR DE LA COMMUNAUTE UNIVERSITE GRENOBLE ALPES

Spécialité : **Optique et Radiofréquence**

Arrêté ministériel : 25 mai 2016

Présentée par

Nisrine ARAB

Thèse dirigée par **Julien POËTTE, Maître de conférences, Université Grenoble Alpes**, et
codirigée par **Lionel BASTARD, Maître de conférences, Université Grenoble Alpes.**
préparée au sein du l'**Institut de Microélectronique Electromagnétisme et Photonique – Laboratoire d'Hyperfréquence et de Caractérisation (IMEP-LAHC)**
dans **l'École Doctorale Electronique, Electrotechnique, Automatisme et Traitement du Signal (EEATS)**

Optique intégrée sur verre pour la génération de fréquences radio

Thèse soutenue publiquement le **09 novembre 2018**,
devant le jury composé de :

Pr Jean-Emmanuel BROQUIN
Professeur des Universités à l'UGA, Grenoble, président du jury
Pr Pascal BESNARD
Professeur des Universités à l'ENSSAT, Institut Foton, Lannion, rapporteur
Dr Sonia GARCIA BLANCO
Maître de conférences à University of Twente, Enschede, rapporteur
Pr Béatrice CABON
Professeur des Universités à l'UGA, Grenoble, examinatrice
Dr Stéphane BLIN
Maître de conférences à IES, Université de Montpellier, examinateur
Dr Julien POËTTE
Maître de conférences à l'UGA, Grenoble, Directeur de thèse
Dr Lionel BASTARD
Maître de conférences à l'UGA, Grenoble, co-directeur de thèse, invité

Résumé

Les futurs systèmes de communication utiliseront des porteuses de fréquences d'ondes millimétriques (mm) (30 GHz - 300 GHz) et au-delà pour surmonter la saturation des différentes bandes de fréquence et atteindre des débits élevés. Les systèmes radio sur fibre (RoF) ont attiré l'attention grâce à leur faible coût et à la faible atténuation des fibres. Dans le cadre de cette thèse, différentes configurations et plusieurs conceptions de lasers ont été proposées pour la génération de fréquences radio par voie optique. L'amélioration du processus de fabrication de laser développé au laboratoire a permis d'obtenir des sources monomodes émettant autour du pic d'erbium (1534 nm) jusqu'à des puissances optiques de sortie de 41 mW avec une efficacité de 9,8%. Leur largeur de raie optique a été mesurée égale à 2 kHz et leur bruit d'intensité relatif (RIN) égal à -145 dB/Hz après 50 MHz. Avec ces lasers, des signaux électriques à des fréquences millimétriques de largeur de raie de quelques kHz ont été générés. Trois configurations hétérodynes ont été proposées pour améliorer la stabilité thermique des signaux générés afin de répondre aux normes IEEE. Des lasers co-intégrés ont été de plus fabriqués pour générer des porteuses comprises entre 5 GHz et 165 GHz. Une étude comparative a montré que les comportements des porteuses ainsi générées étaient indépendants de la fréquence produite. Enfin, les conceptions de structures intégrant coupleur, adaptation de modes et de plusieurs lasers sur verre pompés par une unique source ont été étudiées. En utilisant les porteuses générées par ces dernières réalisations, des transmissions de données ont été accomplies répondant aux normes requises.

Abstract

Future communication systems will use millimeter-wave (mm) (30 GHz - 300 GHz) frequency carriers and beyond to overcome the saturation of different frequency bands and achieve high data rates. Radio-over-Fiber (RoF) systems have gained attention thanks to their low cost and low fiber attenuation. In this thesis, different configurations and several laser designs have been proposed for radio frequency generation by photonic based technique. The Improvement of the laser fabrication process developed in the laboratory resulted in single-mode sources emitting around the erbium peak (1534 nm) up to 41 mW optical output power with 9.8 % efficiency. Their optical linewidth was measured equal to 2 kHz and their relative intensity noise (RIN) equal to -145 dB/Hz after 50 MHz. Using these lasers, electrical signals at millimeter frequencies having linewidths of few kHz have been generated Three heterodyning configurations have been proposed to improve the thermal stability of the generated signals in order to meet the IEEE standards. Co-integrated lasers have been further fabricated to generate carriers between 5 GHz and 165 GHz. A comparative study showed that the behavior of the carriers thus generated was independent of the produced frequency. Finally, the designs of structures integrating coupler, tapers and several lasers on glass pumped by a single source were studied. By using the carriers generated by these latest implementations, data transmissions have been accomplished meeting the required standards.

Table of Contents

Acknowledgments

At first, I would like to thank Jean-Emmanuel Broquin, the lab director during my stay in IMEP-LAHC as a PhD student for welcoming me in the lab and having the good conditions for work. Also, thanks for accepting to be the president of my jury.

Many thanks go to Professor Pascal Besnard and Doctor Sonia Garcia Blanco for accepting to review my manuscript and to Professor Béatrice Cabon and Doctor Stéphane Blin for being the examiners during my defense.

My warmest thanks go to my supervisors Julien Poëtte and Lionel Bastard. Your scientific rigor, your dynamism, your involvement and your availability have been a fundamental support to my thesis work. Julien thank you for the long days you spent with in the ground floor for almost “ALL” the data transmission measurements I did. Thanks also for the long long hours of discussion. Lionel, thanks for training me on all the fabrication process and characterization benches, for all the time you spent doing AFM images for the Bragg grating, for all the round trips you did to Teem Photonics sometimes for a small 8° ferrule… I wouldn’t imagine myself advancing that much without your constant support scientifically as well as morally. I was lucky to work with both of you!! Sorry for complicating your days sometimes just because I was too motivated and because a very good result was never enough…

A special thank you for Béatrice Cabon for her constant advices and support.

Thanks for all the platforms responsible: Aude, Nicolas, Xavier and Gregory. I am glad, that my work did the tour in the four platforms! Aude, thanks for your kindness and smile every time I called you declaring a problem in the clean room. Nicolas thanks for your availability and will to help whenever I needed help, and thanks for the small discussions! Xavier, I am sure I wouldn’t be able to do the AFM images without the daily help during the measurements.

Thanks for TEEM photonics that helped me many times via my supervisor Lionel Bastard. Thanks for providing me with several 8° fibered ferrules and a fiber array. Thanks also for the fiber-glass connectorization process! Your help was critical many times during my work.

For all the administrative people thanks! Dahlila, Fabienne, Isabelle, Valérie, Brigitte and Annaïck.

Thanks for all my officemates: Sandie, Louison, Romain and Fatoumata. Sandie and Louison, thanks especially for your help after my arrival to Grenoble, for all the dinners, laughs, 9GAG breaks in the office, Lebanese and German languages courses… These days are unforgettable!! Also, thanks for the scientific discussions! Romain, my French language consultant, thanks for all the translations. I approve you are not that bad in French even if sometimes you forget that "requirements" is "exigences" :P Also thanks for all the political and cultural discussions. Fatoumata, thanks for all the lunches we had together in BBQ Damas and 231st Burger. Mr. Cazimajou (Thibauld), I am confused, were you an officemate? I am sure for a while you used to spend a lot of hours hours per day in the A306 office. Thank you for all the discussions, fun, dinners and mostly thanks for being my friend and making me laugh during my bad days.

It's true that, officially I was in the A306 office, but I had another office 😊 the A307. Mohamad and Ali Thank you. Both of you in addition to Zaynab, Mahrukh and cutie Abdullah: you were my family in Grenoble. Thanks for all the dinners at your places and the restaurants. Mohamad, thanks for being ready with your tissues when I needed them!!

Thanks to Dimitrios Daminaos for his help many times in the clean room.

During my three years as a PhD student, I have passed through different very good, good bad and very bad moments. I would like to thank my lab friends who were beside me when I really needed them. Thank you so much Mohamad, Thibauld, Robert, Victoria and Romain for your support!!

Thanks to all the people with whome I had some discussions in the lab: Theano, Christoforos, Furat, Habib, Timothée, Thomas, Elodie, Hassan, Mathieu, Licinius…

Thanks for the FIWIN5G ESRs especially Robert, Ahmad, Andrzej, Marc, Igor, Maria, Mu-Chieh and Muhsin. I really enjoyed hanging out with you in Madrid, Copenhagen, Duisburg, London…after long days of lectures.

Thanks for my main travel-mate Diana. Sorry for missing some streets in Toulouse, Avignon, Nîmes, Annecy, Marseille, Montélimar and…, hopefully we will visit more places and miss more places. Rita and Isabelle, thanks for hosting me XX times in Lyon and Paris sometimes with very short notices.

Since August 27th 2018, I started a new job in kapteos. Thanks for everyone there for their support during the preparations for my defense. Thanks Lionel Duvillaret (CEO of Kapteos) for your presence the day of my defense.

The sincerest thank you is for my family, mamati, papati, aloubi, nahoulti and charboulti. Thanks for all your support and love. Sorry for making you sad each time I leave but hopefully I made you proud of me.

General introduction

The electromagnetic spectrum at the millimeter wave (mm-wave) band extends from 30 GHz to 300 GHz, and the terahertz (THz) or submillimeter band ranges from 300 GHz to 3 THz. For a long time, these parts of the electromagnetic spectrum have not been used, but recent advances in mobile telecommunication systems have made them very attractive. However, only few devices are able to generate signals at these frequencies.

The first experimental demonstration of electromagnetic wave generation took place in 1890, when Hertz generated, for the first time, electromagnetic waves traveling in free-space and thus confirmed Maxwell's theory. His apparatus produced waves in the MHz frequency regime. Researches have continued, and in the 1930s new coherent microwave sources based on vacuum tubes, such as the klystron have been developed. These sources emitted in the K band (18-26.5 GHz) and have been widely used for radar applications during the World War II.

Later on, oscillators generating mm-waves have been developed based on the electronic frequency multiplication. This technique has been used till now for THz generation. Simultaneously, there was an interest in the field of spectroscopy which lead to the development of Fourier Transform Spectroscopy (FTS) and the Fabry-Perot interferometer. Later, Backward Wave Oscillators (BWO) (named also "O-Carcinotrons") working up to 150 GHz were developed in France by Thomson CSF and then extended to up to 1 THz in Russia.

The development of compact continuous-wave (CW) and coherent electric sources with large bandwidth has taken a big interest in research for microwave and mm-wave generation. Such sources are useful in many applications such as radar and spectroscopy. Since 1970, compact electronic oscillator that can generate microwave signals exist like Gunn oscillator, which are semi-conductor devices made in GaAs or InP, the transistor oscillators and IMPATT (Impact-Avalanche and Transit-Time) oscillators. However, these microwave sources show bad performances in terms of noise. Moreover, at high frequencies, these oscillators have low output power.

In the turn of the century, telecommunication systems requiring high carrier frequencies and optical signal transport such as "radio-over-fiber" (RoF), emerged. These applications required devices able to generate these frequencies using photonics sources. Unfortunately, direct generation of mm-wave and THz waves using photonic sources is limited by the lack of semiconductor materials that have a gap band sufficiently small to be able to generate optical frequencies lower than a few THz. Quantum

cascade lasers however, which have been first proposed in 1971 and fabricated in 1994, can generate THz wave, but without any tunability.

Photomixing is an indirect photonic approach to generate tunable carriers both in the mm-wave and THz frequency ranges. It consists of mixing two optical signals at different wavelengths on a photodiode. The nonlinearity of the photodiode allows the generation of a sinusoidal electrical current, whose frequency is the frequency difference between the two optical signals.

The goal of this thesis is the fabrication and characterization of single mode DFB lasers on glass designed for mm-wave and THz generation in Radio-over-Fiber (RoF) systems. This manuscript is composed of four chapters. In the first chapter, we present the figures of merit in RoF systems to set the objectives in term of performances for the devices we want to fabricate. Then, photonics-based techniques for mm-wave generation are listed while highlighting their advantages and drawbacks. As glass integrated technology will be used in this work, we summarize the works already achieved using this technology for the fabrication of single mode DFB lasers on glass in the laboratory.

Each laser is composed of an amplifying medium and a feedback function. In the second chapter, we present the fabrication and characterization of each of these two elements. Our lasers amplifying medium is a waveguide fabricated in an Er/Yb co-doped phosphate glass and the feedback is ensured by a Bragg grating etched on top of the amplifiers. Our lasers are designed to emit at 1.5 µm using 980 nm optical pumping. After optimizing the fabrication process, our lasers are characterized in terms of optical output power, linewidth and relative intensity noise (RIN).

In chapter three, carriers at mm-wave frequencies are generated using the fabricated DFB lasers on glass. At first, the results of some simulations are presented to show the accuracy of our technology, and its capability to generate mm-wave and THz carriers. The stability of the generated carriers is investigated by comparing three different configurations using independent free-running lasers. Moreover, this comparison is accompanied by data transmission measurements for an evaluation of the signal transmission performance in RoF systems.

In chapter four, co-integrated lasers with three different designs are presented. Using each of them, radio frequency carriers are generated and evaluated in RoF systems.

1 State of the art: Millimeter wave generation

1.1 Introduction

This first chapter is the state of the art of millimeter wave (mm-wave) (30 GHz-300 GHz) band generation for RoF systems. At first, the RoF principle of operation is presented. Then, to understand how to characterize signals used in RoF systems, the figures of merit for generated carriers devoted to communication systems are introduced. The mostly used photonic techniques for mm-wave carrier generation are listed. Their advantages and disadvantages are highlighted.

In this work, single mode DFB lasers on glass are proposed as substitutes to semi-conductor lasers for mm-wave generation. An overview of the lasers that have already been fabricated using the ion-exchanged glass integrated technology is given.

In the end of this chapter, the outline and the aims of the works presented in this manuscript are presented.

1.2 Radio over Fiber

This thesis is a part of and has been funded by the European project FIWIN5G (Fiber-Wireless Integrated Networks for 5th Generation delivery) [1], in which the main application is the study of potential solution for next generation RoF communication systems.

Mobile communication has gone deep into people's everyday lives. The personal communication industry is confronting a huge growth in the number of users worldwide and in the demand for high data rates. Based on Cisco, mobile data traffic is expected to grow to 49 exabytes per month by 2021, a sevenfold increase over 2016 as shown on Figure 1-1 [2]. A new generation of mobile wireless technology using new frequency bands is thus needed.

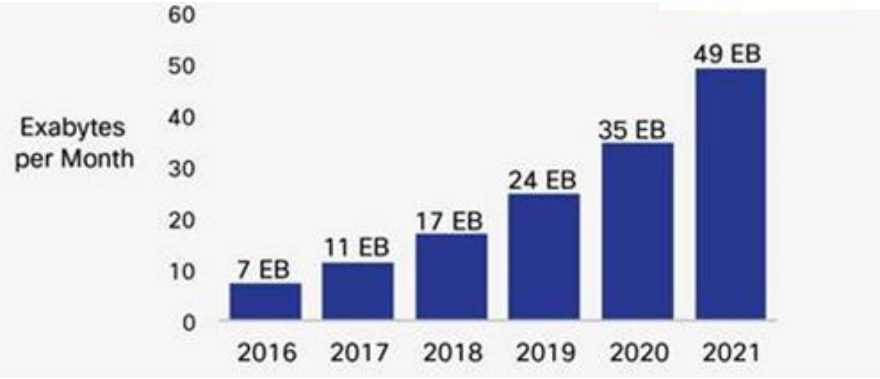

Figure 1-1. Cisco mobile data traffic previsions, 2017 [2]

The smartphones and other electronic devices use very specific frequencies on the radiofrequency spectrum. Typically, they were lower than 6GHz for telecommunication. But as more devices come online, these frequencies bands are getting crowded. In order to fulfill this demand and the wish to reduce the latency, a solution is to open new and higher frequency bands. Currently, the 5th generation is planned to include 26 GHz and or 28 GHz bands, while millimeter wave frequencies between 30 GHz and 300 GHz are experimented for further generations. This section of the spectrum has never been employed before for mobile services. However, mm-waves cannot travel well through building and other obstacles and tend to be absorbed by plants and rain [3] [4]. For this reason, RoF systems gained attention.

To extend the geographical coverage of radio frequency signals, and to respond to the constantly increasing demand for high bandwidth and high data rates, the use of hybrid solutions combining fiber optics technology with the radio frequencies was proposed. These solutions are known as RoF [5] [6]. RoF is devoted to the optical transmission of analog microwave signals. Indeed, instead of distributing digital signals to communicate between each access point, which requires signal processing for

analog/digital then digital/analog conversions, RoF systems can be transparent by distributing analog radio signals. The radio signals are transposed on an optical carrier by modulating the intensity or the phase of a laser source optical signal. Low loss propagation is then possible thanks to the optical fibers that have low attenuation (0.2 dB/km) and wide bandwidth.

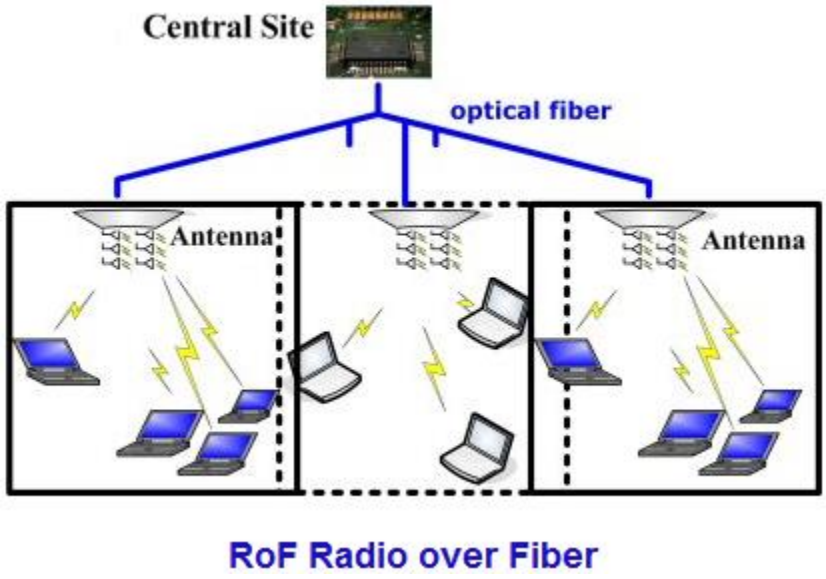

Figure 1-2. Example of a radio over fiber architecture [7].

Figure 1-2 illustrates an example of RoF architecture. The optical sources allowing the conversion of the signal containing the data on an optical carrier are placed in the central site. Then, the optical signals are coupled, if needed, and sent over long distance in the optical fiber. The transported signal can be split before being sent to the receivers composed of the photodiode and the antenna. The optical/electrical conversion occurs in the photodiode. The signal can be converted to the desired frequency on the central station or on the receiver, depending on the solution selected to generate the radio signal to be transmitted. The antenna ensures the wireless transmission at a certain distance, close to the final user.

RoF systems present many advantages over conventional coaxial cables or wireless systems:

- Low propagation attenuation thanks to the use of optical fibers.
- High capacity because higher frequencies can be accommodated thanks to the high bandwidth of the optical fibers and wavelength division multiplexing.
- Immunity to electromagnetic interferences.
- Low cost and light weight of fiber solution compared to copper.

- High losses of the airborne signals from walls and obstacles, which limits interferences from two adjacent rooms (cells) and increases security.

Several mm-wave bands have been subject of research using RoF systems [8] [9]. However, the frequency band that attracted the most attention is around 60 GHz, mainly for two reasons:

1) This frequency coincides with the oxygen absorption peak, which results in high atmospheric attenuation [10]. This will help to reuse identical frequencies as the cell sizes will be small.
2) There is 7 GHz of unlicensed spectrum around the 60GHz in North America that overlaps with unlicensed spectrum in Europe, Japan and Australia, which is an opportunity for a worldwide standardization and commercial products [11].

The main drawbacks of RoF systems at high frequencies are the need for high-speed optical components and potential chromatic dispersion effects that can impact the transmission, even when using short fibers. Therefore, advanced modulation and transmission schemes are required. Numerous techniques have been developed to generate frequencies with characteristics that meet the requirements of specific applications.

1.2.1 Modulation formats

Before starting the state of the art of the existing techniques allowing us the generation of mm-wave frequencies for RoF systems, the different modulation formats that will be used are defined. In digital communications, the data signal is represented by a stream of the binary numbers of “0” and “1”, called bits. The simplest modulation scheme directly translates these bits into light pulses is termed On-Off Keying (OOK). OOK can be used with or without extinction of the light at the end of each bit: Return to Zero (RZ) or Non-Return to Zero (NRZ). In radio over fiber, this signal must be modulated by an analog radio frequency carrier signal which is a continuous sinusoidal signal with a given frequency. The modulation can occur on the phase, frequency or amplitude of the carrier signal, they are called phase-shift keying (PSK), frequency-shift keying (FSK) or amplitude-shift keying (ASK) respectively. In case at least two-phase states and at least two amplitudes are combined, such a signal can be represented by two sinusoidal waves in quadrature, therefore such modulations are called quadrature amplitude modulation (QAM). Each particular combination of phase, frequency and amplitude of the signal is called a state and encodes one symbol. A given modulation scheme allows representing M bits per symbol, depending on the number of symbol used for the transmission. The encoded symbols per second is the symbol-rate of the modulation. We can also talk about data-rate, which is defined by the number of encoded bits per second.

- Binary phase shift keying (BPSK)

BPSK is a simple phase shift keying where the symbols are encoded in two phase values (0 and π) of the carrier signal. Here, one symbol contains one bit and the spectral efficiency is 0.5 bit/s/Hz. This efficiency is calculated from the bandwidth of the main spectral lobe in case of modulating the carrier with square pulses, we use the same method in the following formats for comparison. Spectral efficiency shows the number of bits that is transmitted per second per bandwidth in Hz. This parameter is particularly useful to compare the required bandwidth for different modulation format, which is an important criterion in the context of crowded and/or limited available spectrum. The low efficiency of BPSK means that the required frequency bandwidth in Hz is equal to the double of the data-rate.

The use of BPSK requires a stable optical carrier over a duration much longer than the bit duration. Therefore, the spectral linewidth of the source laser and the local oscillator is critical. On the other hand, as the number of symbol to be coded is reduced, the requirement on the signal to noise ratio is relaxed compared to more complex formats.

- Quadrature phase shift keying (QPSK)

Doubling the number of possible phase values $\left(\frac{\pi}{4}, \frac{3\pi}{4}, \frac{5\pi}{4}, \frac{7\pi}{4}\right)$ we can have 2 bits per symbol. This modulation has a spectral efficiency of 1 bit/s/Hz. In case of modulation formats with constant carrier frequency, the signal can be represented by the contribution of an in-phase signal and a quadrature signal. Therefore, those two contributions can describe the possible states in a 2-dimensional diagram, called the constellation diagram. This complex diagram is showing the amplitude and the phase of the modulation states. The x axis, called the In-phase (I) axis represents the zero-phase shift, and the y axis, called the Quadrature (Q) axis represents the $\pi/2$ phase shift. Each state can be positioned in this diagram, its coordinates corresponding to the amplitudes the in-phase and quadrature signals. Figure 1-3-a and Figure 1-3-b show the constellation diagram of the BPSK and QPSK modulations with the represented symbols for each state.

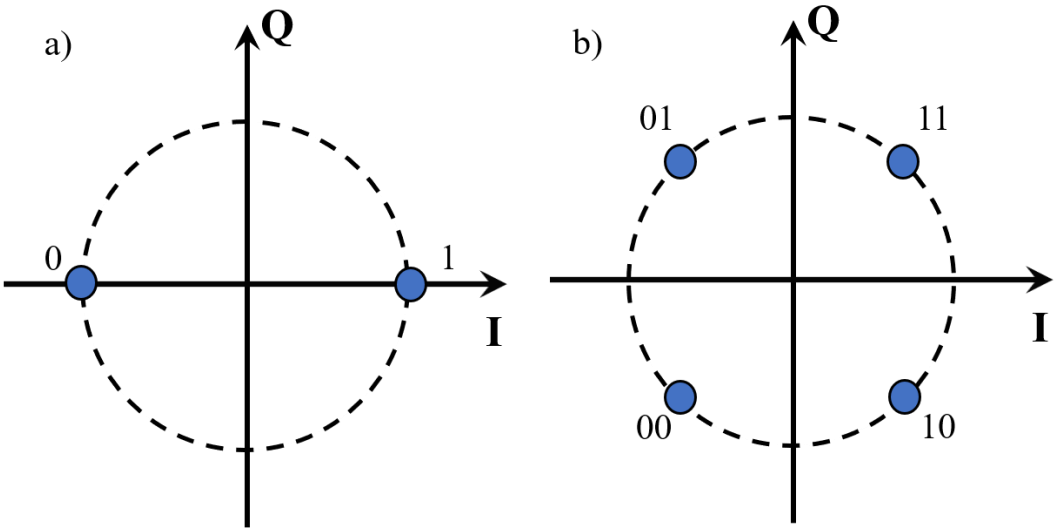

Figure 1-3. Constellation of a) BPSK and b) QPSK modulation formats.

- Quadrature amplitude modulation (QAM)

Higher spectral efficiency modulation formats can be achieved by adding more levels of amplitudes and more phase shift to the reference signal. Those formats are called QAM for Quadrature Amplitude Modulation. QPSK is a basic 4 state QAM modulation with a single amplitude level and can thus also be called 4-QAM. The number of states (M) in M-QAM are following the $M=2^N$ rule, where N is the number of bits in one symbol. The states are generally arranged in circle, in order to reduce the number of possible amplitudes, and can be arranged in a square grid in the constellation diagram, as it is shown in Figure 1-4 for 16 QAM, to keep the inter symbol distance constant on the constellation.

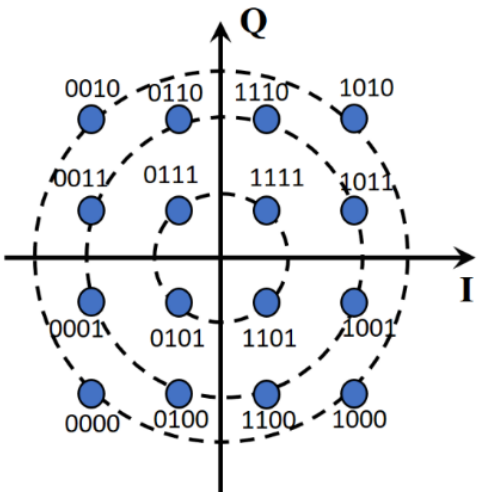

Figure 1-4. 16QAM constellation diagram.

The achievable spectral efficiency is increasing with the number of bits per symbol, it is 2 bit/s/Hz for 16-QAM. Higher order modulations can transfer more bits per symbol, but the symbol amplitudes are getting closer to each other. So, for a constant mean energy of the constellation, higher order modulation formats will be more sensitive to noise. To achieve the same level of error with higher modulation formats, a higher signal-to-noise ratio (SNR) is thus needed.

1.2.2 Figures of merit in RoF systems

Mm-wave RoF systems should answer to requirements to be considered as possible candidates for communication systems. In such systems, the evaluation is performed through data transmission measurements. During these measurements one of two parameters is extracted, the bit error rate (BER) or the error vector magnitude (EVM). BER is the number of errors divided by the number of transmitted bits in a transmitted sequence in a given time interval, and the EVM is the average of the magnitude difference between the reference and the received symbols. BER is an absolute figure of merit that tells us whether a system meets the good performance limits. If the specified limit is not met, BER does not allow meaningful conclusions on the nature of the cause of the errors. In order to know the cause of the error, EVM and constellation diagram can be measured as it qualifies the analog transmission of the symbol. Measured EVM values can also be compared to communication standards such as those provided by ECMA [12] and IEEE [13] to know if they fulfill the requirements.

Measured EVM and constellation diagrams are figures of merit for the accuracy of transmission systems utilizing advanced modulation formats. It provides a way to measure and evaluate the transmission quality when using modulation formats like BPSK, QPSK and 16QAM. Using phasors in the I/Q plane, EVM measures the difference between the reference or ideal symbol vector location and the actual measured vector location. The EVM can be measured on transmitter modulator (it is then referred as back-to-back (b-b) EVM measurement) or receiver demodulator circuits (it is then the total EVM of the system).

EVM is the ratio of the average of the error vector power (P_{error}) to the ideal reference vector power (P_{ref}) (see Figure 1-5). The averages are taken over multiple symbol periods:

$$\mathrm{EVM} = \sqrt{(\mathrm{P_{error}} - \mathrm{P_{ref}})} \times 100 \tag{1.1}$$

It can also be expressed in terms of the constellation (1.2)

$$\mathrm{EVM} = \sqrt{\frac{1}{1000 P_{avg}} \sum_{i=1}^{1000} [(I_i - I_i^*)^2 + (Q_i - Q_i^*)^2]} \tag{1.2}$$

The EVM values measured during our experiments are expressed in %.

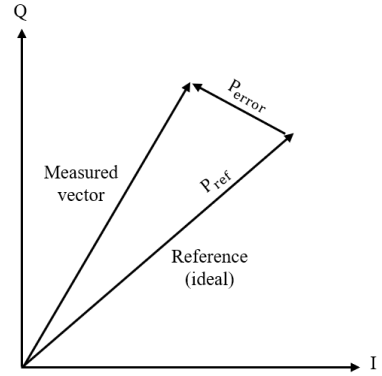

Figure 1-5. the distance of error vector (evaluated from reference and measured vectors) to the reference vector.

Different parameters contribute to the degradation of the measured EVM values. Mainly, these parameters are the signal to noise ratio (SNR) of the transmitted signal and the variance phase noise σ of the carrier and impact the EVM as given in equation (1.1) [14]:

$$\mathrm{EVM} = \sqrt{\frac{1}{\mathrm{SNR}} + 2 - 2\exp\left(\frac{\sigma^2}{2}\right)} \tag{1.3}$$

Based on equation (1.1), to enhance the EVM values, the SNR has to be high and the σ value has to be low. However, in [14], it was demonstrated that the phase noise impact can be seen as a limiting factor, in a way that for a certain value of σ, there is a limit value of EVM that cannot be better even with high SNR.

In addition to these parameters, the cost and simplicity of the system, the capacity in generating high frequencies and the stability are also considered as figure of merits for RoF systems.

- Cost and simplicity: to be attractive for communication, a system has to be cost effective. It is important to select the adequate technology for each subsystem in a RoF system to reduce the expenses. In case complex solution is required, the architecture should benefit from the sharing of the complex structure by placing it in the baseband for example. That's why, it is welcome

to choose if possible the simplest techniques that can answer the requirements of the system without adding multiple expensive or complex electronic and optical components.

- High frequency generation: this figure of merit represents the capability of the system to generate a carrier at a specific frequency with the required bandwidth, and therefore to propose a solution to the problem.
- Stability of mm-wave carrier: the phase noise is related to short term phase fluctuations and can impact the signal quality as already shown. Longer-term stabilities over milliseconds (ms), second or even hour can also impact the system and be caused by the unprecise temperature control of the optical sources or deviationing parameters. The stability of a carrier is evaluated by comparison to IEEE standards [13] that require for a carrier at 60 GHz a maximum frequency deviation equal to ± 20 ppm (particle per million), which is equal to a total deviation of 2.4 MHz.

1.3 Mm-wave generation using photonic based techniques

In this work, we aim at developing an optical system for mm-wave generation. Radio frequency generation can be achieved using either electrical or optical techniques. Mm-wave signals are conventionally generated with complex and/or expensive electronic circuits, after which they are distributed along electrical distribution lines, such as coaxial cables, which intrinsically have high propagation losses. Compared with the electronic solutions, photonic generation of mm-wave carriers has many advantages, such as low power consumption, low cost and the distribution of the optical carrier signals via low loss, inexpensive optical fibers over large distances. The following state of art includes only photonic based solutions. We can classify the techniques for mm-wave generation into 3 categories: Electro-optic techniques where modulators are used, heterodyning techniques using single mode lasers and photonic techniques using multimode lasers.

In this section, the state-of-art of the mostly used techniques is presented.

Optical generation of radio frequencies is based on optical heterodyning technique. The radio signal is generated through the beating of two optical signals on a non-linear optoelectronic converter. Photodiode is the most logical and widely used component for this application. The difference of the optical frequencies corresponds to the generated radio frequency.

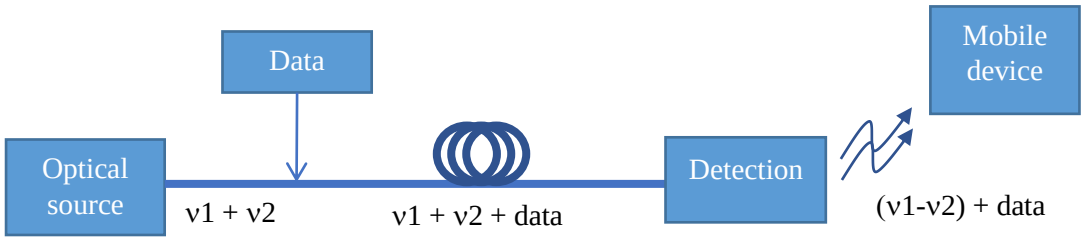

Figure 1-6 Optical radio frequency generation.

Figure 1-6 illustrates the optical radio frequency generation. One or more optical sources are needed to emit optical signals with a particular optical frequency shift. At least one optical signal is modulated to transmit the data in fibers for a long distance. The fiber is finally connected to a photodetector where the optical to electrical (O/E) conversion occurs, and the electrical carrier is generated and then transmitted via cables or wireless to mobile devices. In this work, we are interested in the optical sources that can be used in such systems.

Let us consider two optical fields described as:

$$E_1 = E_{01}\cos(w_1 t + \varphi_1) \tag{1.1}$$

$$E_2 = E_{02}\cos(w_2 t + \varphi_2) \tag{1.2}$$

where E_{01} and E_{02} are the amplitude field terms φ_1 and φ_2 are the instantaneous optical phase and w_1 and w_2 are the angular frequencies of the individual optical waves respectively. After mixing the two optical waves on the rapid PD having a limited bandwidth, the photocurrent generated at the output of the PD is:

$$I_{PD} = I_{DC} + A\cos[(w_1 - w_2)t + (\varphi_1 - \varphi_2)] \tag{1.3}$$

where A is a constant dependent on the amplitudes E_{01} and E_{02} and the responsivity of the photodetector, and I_{DC} is the average photocurrent related to $|E_{01}|^2+|E_{02}|^2$. The term containing $(w_1 - w_2)$ is of interest and it represents the beating signal in the radio frequency range. The terms at higher frequency w_1+w_2 are neglected due the limited bandwidth of the photodetector.

1.3.1 Mm-wave generation by electrical modulation

The simplest method for frequency generation is to modulate the intensity of a single mode laser with a radiofrequency signal. A direct detection on a photodetector after fiber transmission will allow

the production of the electrical radio frequency signal. The laser intensity can be modulated directly by applying the modulating signal or externally by inserting an optical intensity modulator.

Directly modulated laser

Figure 1-7 shows an example of a direct modulation setup. A RF signal is used to modulate the bias current of the laser at the desired frequency. Two optical side bands are generated on the laser spectrum. These side bands are phase locked to the optical signal. This technique is limited by the laser cut-off frequency and can reach a maximum of 30GHz [15], which is not enough to cover mm-wave band.

Figure 1-7.Frequency generation using direct modulation technique.

Externally modulated laser

To overcome the impairments of the direct modulation, external modulation can be used. The simplest setup, shown in Figure 1-8, consists of a continuous wave (CW) laser followed by an external electro-optic modulator that modulates the laser light with an intermediate frequency f_i. The external modulator can be a Mach-Zehnder Modulator (MZM) [16], an Electro Absorption Modulator (EAM) [17] or a Phase Modulator (PM) [18] [19]. The optical components are strongly phase locked together, making this technique largely employed for generating RF signal with good spectral properties. In this case, the impairments derive from the modulator. Non-linearities result in the generation of higher order harmonics that can be undesired. The maximum frequency that can be generated is still limited by the external modulator limited bandwidth and the need for a RF source.

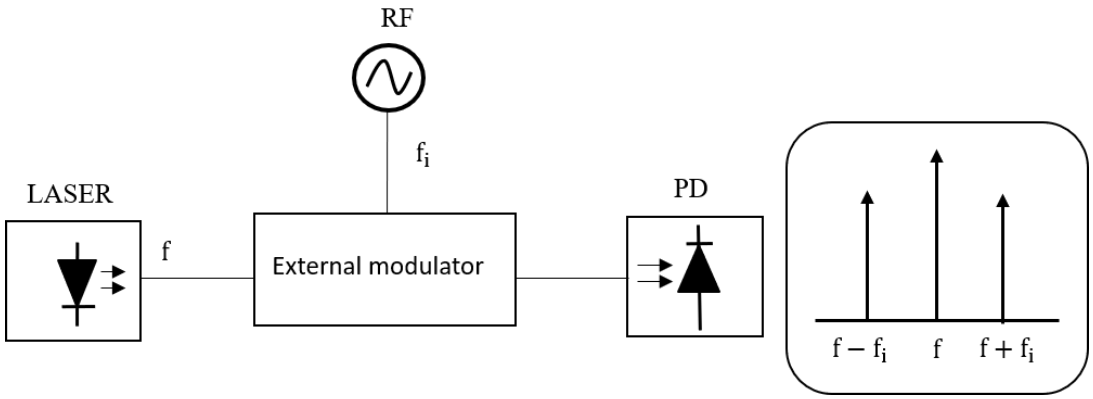

Figure 1-8 Frequency generation using an external modulator.

Since the cost of the modulator and the electrical equipment increases as the mm-wave frequency does, optical frequency multiplication (OFM) has been proposed to generate frequencies above the external modulator bandwidth by profiting from the generation of higher order harmonics [20]. The laser is externally modulated with f_i that is a sub-harmonic of the desired mm-wave frequency. With proper bias and/or modulator configuration, higher order harmonics can be generated. These harmonics are separated by n x f_i with n the order of the generated harmonic. Then the two sidebands that are separated by the desired mm-wave frequency are filtered out.

This technique is limited by the maximum efficient order that can be achieved, the losses due to the filtering and depends on the insertion losses of the used external modulator [21] [22]. A major drawback of this technique is that it leads to complex setups, thus increasing the cost and reducing the reliability of the solution.

Gain switching

Gain switching technique is based on the strong modulation of one single mode semiconductor laser to generate an optical comb. This technique provides a good signal to noise ratio. However, when using this comb source to generate a carrier in the mm-wave band, the phase noise of the mm-wave carrier due to the optical phase decorrelation between the optical modes caused by the chromatic dispersion has already been demonstrated. To reduce the phase noise, the gain switched laser has to be externally injected with a low linewidth laser [23]. This technique still requires a RF reference signal at a subharmonic frequency as modulation source.

Optoelectronic Oscillator (OEO)

The concept of OEO was firstly proposed in 1990 by the NASA's Propulsion laboratory to produce microwave signals with low phase noise [24]. An OEO consists of an optical storage (long fiber loop) and RF feedback parts, including a light source, electro-optic modulator, high Q optical storage element, RF filter and amplifiers. Due to the long optical fiber in the loop, the OEO is typically a multi-mode source. The mode spacing is inversely proportional to the optical fiber length, so if several kilometers of fiber are used, there will be an ultra-narrow mode spacing of hundreds or tens of kHz with a high cavity quality. OEO can generate signals with high frequencies and low phase noise [25]. However, it consists of many electrical and optical components, including a limited bandwidth electro-optic component, which makes it difficult to be used in practical applications for high frequency generation.

1.3.2 Heterodyning using single mode lasers

Two single mode lasers with emission frequencies separated by the desired mm-wave frequency can be mixed to generate mm-wave carriers. Those sources can be free-running lasers, or they can be correlated using a control loop.

Free running lasers:

Mode beating setup using two free running lasers is shown in Figure 1-9. The wavelength of each laser can be either controlled using a temperature controller or adjusted during the fabrication process to obtain a target frequency difference between the two lasers. The two optical signals are injected into an optical fiber using a directional coupler and transmitted to a photodiode. At the output of the photodiode, an electrical signal is generated with a frequency equal to the frequency difference between the two optical signals.

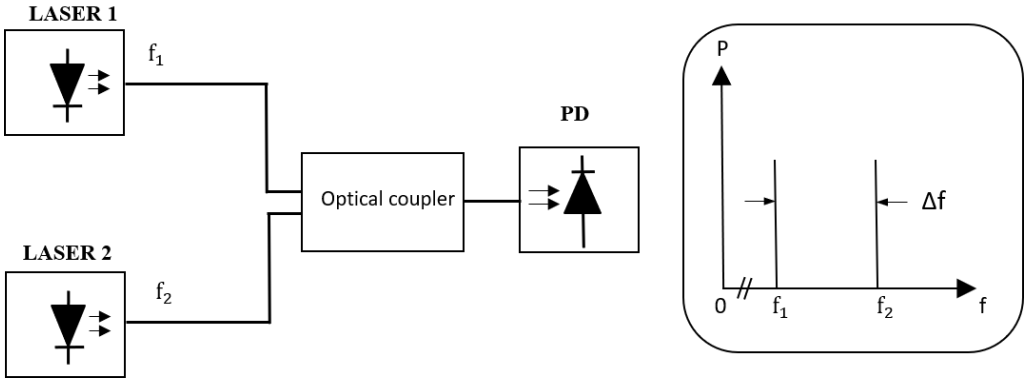

Figure 1-9 Single mode lasers heterodyning setup.

This is the simplest technique for mm-wave generation, and it is suitable to generate high frequencies. The main drawback of this technique is the limitation of the spectral purity and the frequency inaccuracy of the generated carrier highly depending on the respective optical field properties. The spectral purity is mainly determined by the linewidth of the lasers. In the heterodyne process, and as the lasers electrical fields are not coherent, the phase noise of the generated beating is directly related to the combination of the two lasers optical phase noise. Such phase noise can be large when using semiconductor lasers due to their large linewidth (in the order of MHz). Whereas the frequency inaccuracy is due to the temperature laser emission deviation at a slower time scale (> 100 ms) [26].

Some strategies have been proposed to address the frequency inaccuracy issue encountered with semiconductor lasers. Narrow-linewidth lasers such as fiber grating lasers [27] have been proposed to replace the semiconductor lasers. In [27], two fiber grating lasers have been used to generate a mm-

wave carrier at 39.2GHz. The linewidth of the generated carrier was estimated to be less than 50kHz. However, even though the two lasers were thermally controlled, a deviation of 75MHz over 30min has been measured. This technique is thus not sufficient in term of required ±20 ppm (± 1.2MHz around a 60 GHz carrier) frequency accuracy.

On the other hand, different techniques have been used to stabilize the generated mm-wave signals using semiconductor lasers. They have been introduced since the early 1990s [28] such as optical phase-locked loop [29] and optical injection locking [30]. We describe them hereafter.

Optical phase lock loop (OPLL)

OPLL is a technique to achieve phase synchronization between the optical sources signals. As shown in Figure 1-10, the phase error between an RF source reference and the carrier generated using the two lasers is detected through an RF mixer followed by a low-pass filter. This error signal is then sent back to modulate the injection current of one laser in order to adjust its frequency. With specific feedback condition, the generated carrier can be locked to the RF source, which results in a much lower phase noise than the signal obtained without feedback.

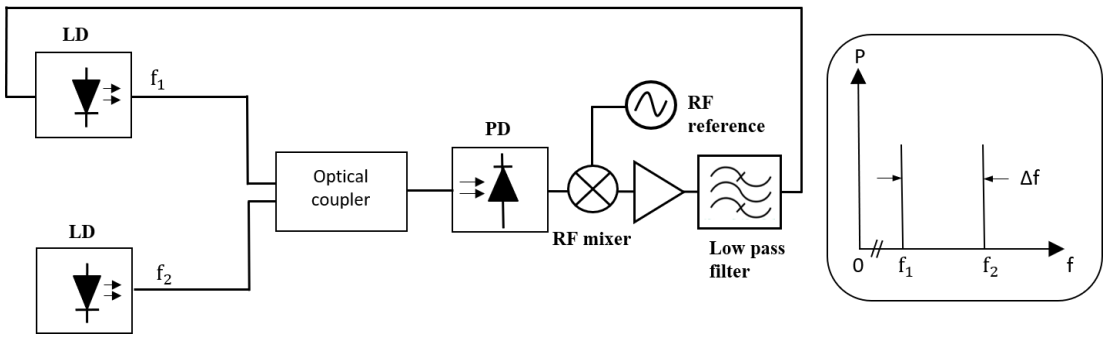

Figure 1-10 Optical phase lock loop setup.

In such systems, a stable carrier can be generated with low phase noise. The spectral purity is determined by the spectral purity of the source reference and the control loop performances. Frequency tuning is achieved by varying thermally the wavelength of one or both lasers [31]. The main drawback is the complexity of the setup and the need for a reference RF oscillator.

Optical injection locking (OIL)

OIL is another method used for phase synchronization, and thus generating carriers with high spectral purity. As depicted in Figure 1-11, using this technique, a master laser is modulated by an RF source. Consequently, multiple side bands appear around the central wavelength at the output of the master laser. Using a fiber optical splitter, this signal is injected in two slave lasers, and then the

wavelengths of the lasers are chosen to be near the n^{th} order side band, so that the two slave lasers are locked at the desired frequencies.

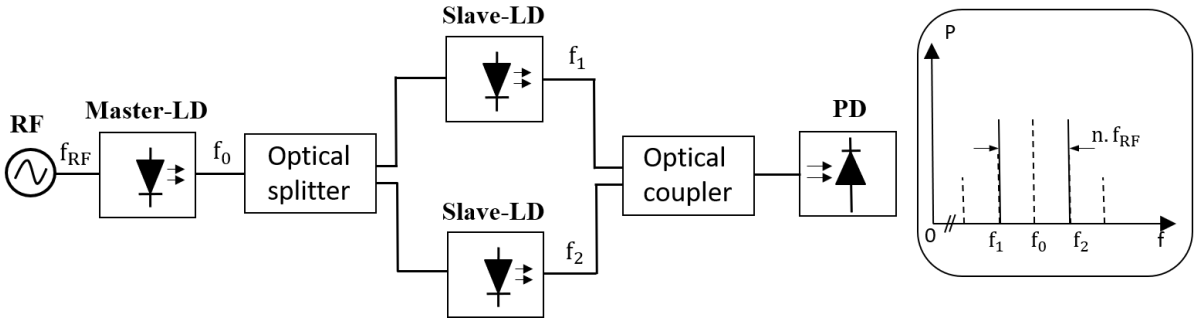

Figure 1-11 Optical injection locking setup.

OIL has relatively a simple setup and it can generate high frequencies with low phase noise. However, the non-linear distortion and the noise of the directly modulated laser limit its performance [32].

1.3.3 Heterodyning multimode laser

In addition to the modulation techniques and the heterodyning of two single mode lasers for mm-wave generation, Multimode lasers such as mode locked lasers (MLL) and dual mode lasers (DML) have attracted attention for high frequency generation as a cost-effective solution compared to modulation techniques since the use of modulator and RF signal oscillator is avoided. Moreover, only one optical source is needed.

- Mode locked lasers

Mode locked lasers emit a comb of ultrashort pulses separated by a repetition period pre-determined during the laser cavity fabrication. Its corresponding optical spectrum is a comb containing peaks separated by the laser free spectral range (FSR). This FSR corresponds to the fundamental frequency that can be generated with such lasers.

As illustrated in Figure 1-12, the setup is simple, since it requires only one MLL, powered with a DC signal. Thanks to the generation of the heterodyned modes in the same laser and the phase locking mechanism of such laser, these modes are correlated and thus the phase noise of the generated electrical signal is smaller when compared to free running multimode or heterodyned single mode semiconductor lasers. MLL have already been widely used for mm-wave generation at different frequencies [33] [34]. The main drawback is the chromatic dispersion in the optical fiber linking the MLL to the photodiode

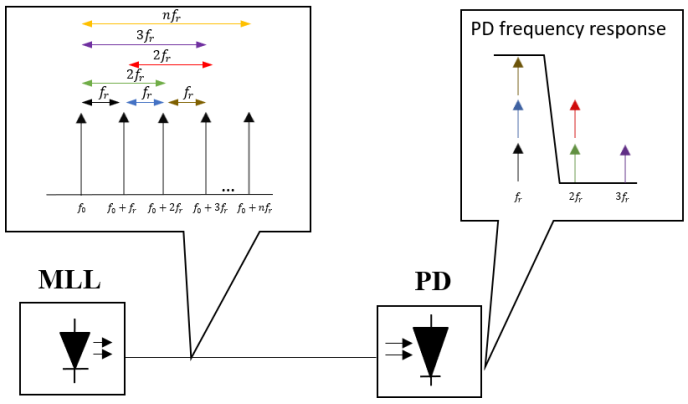

Figure 1-12: Mm-wave generation using an MLL.

[35]. Indeed, since the spectrum of the MLL spans over a quite large region, chromatic dispersion in the optical fiber modifies the relative phase shift between the modes of the MLL. This results in lower values or even cancellation of the RF power on the photodiode depending on the fiber length. To reduce this effect, an optical filter can be used to filter the used optical modes but then the available optical power decreases dramatically.

Dual mode laser (DML)

DML can generate simultaneously two wavelengths from the same optical cavity. The cavity is pre-designed to have a specific difference between the two wavelengths that corresponds to the desired frequency. A low phase noise of the generated signal is expected as the optical modes are produced in the same cavity. As shown in Figure 1-13 the setup is quite simple, the optical output signal of the laser is sent via a fiber to a photodiode where the electrical signal is generated.

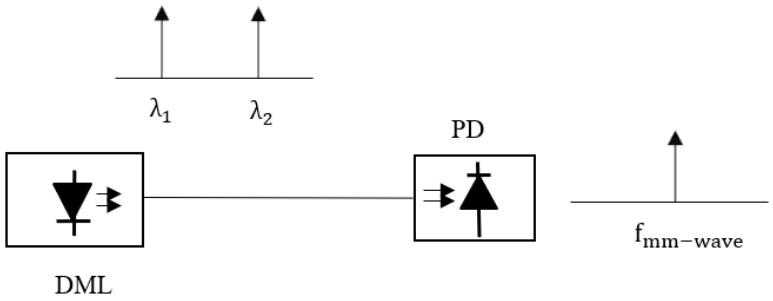

Figure 1-13 Dual mode laser setup.

Works reported using DML can be classified in two categories, the dual mode fiber lasers and the dual mode semiconductor lasers. In [36], using a dual mode fiber laser, a carrier at 40.95GHz having an electrical linewidth of 80 kHz has been generated. However, such dual mode fiber laser is composed

of a fiber ring laser with an optical band pass filter having two narrow pass bands in order to filter out the undesired cavity modes. It is not easy to fabricate a band pass filter with an accurate wavelength control. Moreover, the tunability of such laser is not easy.

Dual mode semiconductor lasers gained more attention with their compactness, low power consumption and wide tuning range. Two different structures have been reported. In [37], two DFB sections coupled into a Y-junction in order to obtain a monolithically integrated dual-frequency source. The mm-wave frequency is obtained by setting a different current I_{DFB1} and I_{DFB2} in each laser (see Figure 1-14).

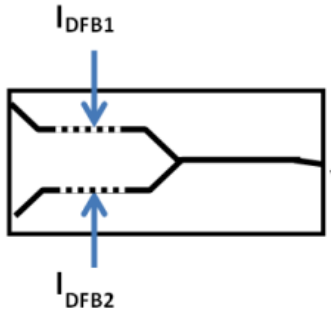

Figure 1-14 Dual mode semiconductor lasers [37].

Note that this device is not really a dual-mode laser, based on our definition, since the two laser cavities are not optically coupled. A carrier was successfully generated at 146 GHz using this structure, but its phase noise is not given. Moreover, the generated RF signal is very weak and requires an electrical amplification of 50 dB, preceded by the use of two erbium doped fiber amplifiers, to be measured.

In [38], a device containing two DFB sections separated by a taper is presented. In this case, the cavities are optically coupled since the signal emitted by one DFB passes through the other (see Figure 1-15)

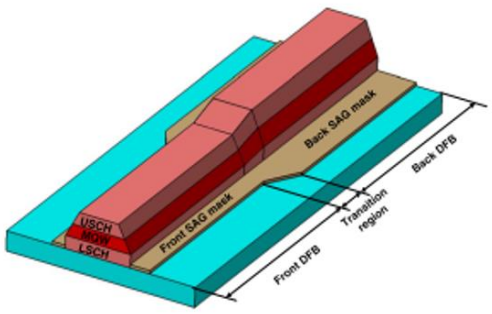

Figure 1-15 Dual mode DFB laser [38].

This device allows the generation of two optical frequencies separated by frequencies ranging from 42 GHz to 1 THz. However, no signal is generated in the mm-wave or THz domain and the phase noise of the laser modes is not given.

1.3.4 Summary

Table 1-1 summarizes all the cited techniques with their advantages and disadvantages.

		Ref.	Advantages	Disadvantages
Modulation techniques	Direct	[15] [39]	Simple and low cost	Limited generated frequency (< 30 GHz)
	External	[20] [21] [22]	Mm-wave generation	• Complexity of the utilized electronics. • Frequency limited by the modulator bandwidth
	Gain switching	[23]	Good signal to noise ratio	• Large spectrum and number of modes • Sensitive to dispersion
	Optoelectronic oscillator	[25]	Low phase noise (− 95 dBc/Hz at 1 kHz for a carrier at 90 GHz)	• Complex setup • Frequency limited by the modulator bandwidth
Single mode lasers	Free-running lasers	[26] [27]	• Simple • Linewidth < 50 kHz with fiber lasers	• Linewidth > 1 MHz with semiconductor lasers • Deviation = 75 MHz /30 min with fiber lasers
	OPLL	[31]	Low phase noise	Complex setup
	OIL	[32]	Low phase noise	• Non—linear distortion • Noise of the directly modulated laser • Difficult tuning
Multimode lasers	MLL	[33] [34]	Low phase noise	Chromatic dispersion
	DML	[36]	Linewidth equal to 80 kHz with fiber lasers	• Complexity linked to the band pass filter fabrication • Difficult tuning

Table 1-1 Comparison of simple photonic techniques for mm-wave generation.

1.4 Glass integrated optics

Up to before this work, ion-exchanged glass integrated lasers were never used for mm-wave generation. However, CW single mode lasers on glass have already been fabricated in our laboratory during the thesis of Sylvain Blaize [40], Lionel Bastard [41] and Marco Casale [42].

The fabrication of lasers operating in the C band (1530 nm – 1560 nm) is possible thanks to the use of Erbium/Ytterbium doped glasses specifically engineered for silver sodium ion exchange [43]. Optical pumping needed to obtain a laser effect is achieved using semiconductor laser diode emitting at 980 nm.

Laser sources fabricated by ion exchange present interesting characteristics over semiconductor lasers. DFB lasers on glass prove to be stable sources with optical linewidth equal to 8 kHz [41]. In [40] and [41], a matrix of co-integrated DFB lasers on Er/Yb co-doped glass has been fabricated as shown in Figure 1-16 [44]. A Bragg grating is etched on the surface of the sample, with 150 nm depth and a grating step of 500 nm. The implementation of waveguides with different aperture widths allows the emission at distinct wavelengths. These lasers emit a single wavelength around 1534 nm with an optical power of 4.3 mW and a slope efficiency of 2.7 %.

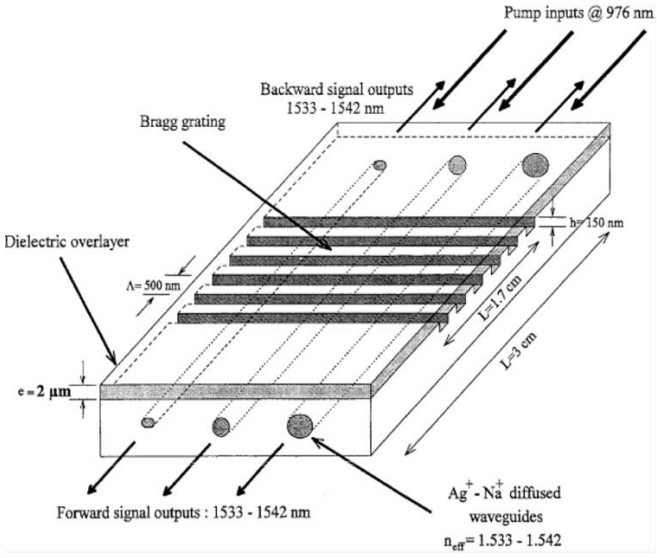

Figure 1-16 Glass integrated optics laser matrix [44]

Hybrid CW DFB laser on glass substrate has also been fabricated [42]. Such a laser is illustrated in Figure 1-17. It has been fabricated to test the capacity to integrate active functions (amplification and emission) and passive ones (multiplexing, filtering…) on a single glass substrate. This laser is composed of a Bragg channel waveguide selectively buried in the passive glass substrate and loaded

by a slab waveguide defined on an active glass co-doped with Erbium and Ytterbium. It emits a fiber-coupled optical power of 420µW at 1534nm for 390mW of optical pump power.

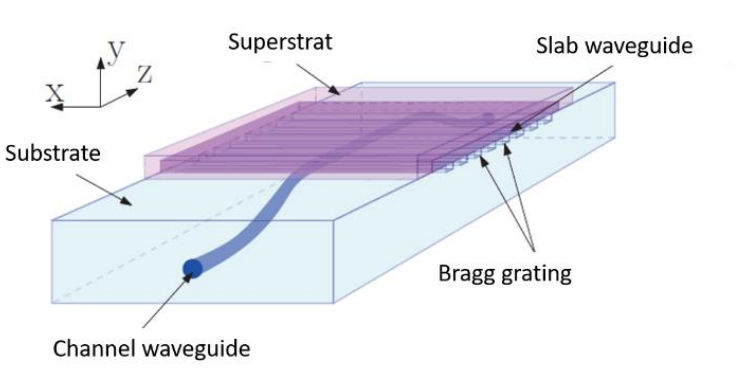

Figure 1-17 Three-dimensional hybrid DFB laser on glass substrate [42].

As a summary of these results concerning glass DFB lasers, this technology seems promising in the context of mm-wave carrier generation for several reasons:

- The wavelengths that can be generated with these lasers are compatible with the generation of carriers in the mm-wave range.
- The linewidth of these lasers is several of magnitude smaller than that of semiconductor devices. This should translate into mm-wave carriers with a phase noise several orders of magnitude lower than that obtained with standard photonics solutions.

1.5 Outline and aims of this thesis

In this chapter, the state of the art of the existing photonic systems for mm-wave generation has been carried out. The different techniques usually employed to produce mm-wave carriers have been listed and their respective advantages and limitations have been presented. At last, earlier works on glass DFB lasers carried out in the laboratory have been presented. It appears that these lasers could be good candidates for the generation of mm-wave carriers since they possess key advantages over the semiconductor lasers which are usually employed for this application. In this thesis, we propose the use of single mode DFB lasers on glass that will be designed and fabricated for mm-wave generation by heterodyning.

Indeed, the main issues with carriers generated by heterodyning two single-mode lasers are their large electrical phase noise induced by the use of the large linewidth semiconductor lasers and the large frequency deviation obtained when fiber lasers are used. DFB lasers on glass have already proved to

be stable and possess an ultra-narrow linewidth. These two characteristics combined with the simple heterodyning technique are expected to allow us the generation of stable narrow mm-wave carriers.

In the second chapter, the different steps of the fabrication process of DFB lasers on glass are presented. At first, Erbium Ytterbium doped waveguide amplifiers are fabricated and characterized. The different steps for implementing the Bragg grating are then presented. Multiple improvements on the grating fabrication process are highlighted. A fiber-glass connectorization process is presented. The last section is devoted to the characterization of the DFB laser on glass in term of output optical power, emission wavelength, thermal sensitivity, relative intensity noise and linewidth.

In the third chapter, mm-wave generation using DFB lasers on glass is successfully achieved for the first time. At first, the results of some simulations are presented to study the potential generated frequencies and the accuracy of our fabrication process. Then a comparative study between three configurations using independent free-running DFB lasers on glass is conducted to understand how thermal fluctuations influence the stability of the generated carrier. The quality of the generated carriers is evaluated by performing data transmission measurements.

In chapter four, three co-integrated laser designs will be presented: two co-integrated lasers, the co-integrated lasers with a waveguide Y-junction and lastly a dual mode laser. Radio frequency carrier generation using each design is performed and the generated carrier is characterized in term of linewidth, frequency deviation and thermal dependency. Moreover, data transmission measurements are performed in order to ascertain the suitability of these carriers for their target application.

2 Glass DFB lasers: design, fabrication and characterization

2.1 Introduction

A laser is composed of an amplifying medium contained in an optical cavity. When pumped, this medium emits photons by stimulated and spontaneous emission, with wavelengths located in the gain region of the amplifier. The cavity returns a part of those photons of the signal to the amplifier medium achieving what is called an optical feedback. When the small signal gain in the amplifier medium exceeds the losses in the system, laser emission occurs.

In our work, the amplifier medium is an ion-exchanged co-doped Erbium (Er) Ytterbium (Yb) IOG1 (Integrated Optics Glass1, manufactured by Schott™) [45] glass substrate on which waveguides with specific widths are imprinted. The optical cavity is composed of a Bragg grating with pre-determined spatial periods Λ etched on the waveguides. This grating provides optical feedback around a specific wavelength called the Bragg wavelength λ_B.

In the first part of this chapter, the design, fabrication and characterization of the amplifiers are detailed. A model leading to the prediction of the waveguide's modicity at different wavelengths is used. Then, the multiple technological steps leading to the fabrication of the waveguides are expanded. Finally, amplifiers are characterized.

The second part is devoted to the Bragg grating implementation and characterization. The standard grating implementation process is presented before highlighting the multiple modifications that have been achieved during this work to improve the Bragg grating quality.

The third and last part of this chapter deals with the fabricated laser characterization. The emission wavelength and optical power are measured. Then the laser linewidth and relative intensity noise measurements are presented.

2.2 Erbium Ytterbium co-doped waveguide amplifiers

The amplifying medium in our DFB lasers on glass consists of ion-exchanged waveguides on IOG1 Er/Yb co-doped glass [45]. The theoretical study of the amplification with this medium has been previously studied in another work [41] prepared in IMEP-LaHC laboratory. In the following subsection, the substrate used in our studies, the design, fabrication and characterization of the Er/Yb Doped Waveguide Amplifier (EYDWA) are presented.

2.2.1 Glass

Glass, associated with the ion exchange process, was identified since 1969 by Miller [46] as one of the substrates on which optical integrated circuits could be fabricated. To better understand how this process can modify the properties of the glass, we need to look closely at its composition. Only oxide glasses [47] are described here as they are used in this work.

An oxide glass is an amorphous solid derived from an oxide mixture. The different oxides which compose the glass can be classified into three categories according to their oxygen binding energy [47] [48] [49]:

- The network oxides have a binding energy higher than 300 kJ/mol, they can compose a glass by themselves. They give their name to the glass. Silicate (SiO_2), borosilicate (B_2O_3-SiO_2) and phosphate (P_2O_5) fall in this category.
- The intermediate oxides of the network have a binding energy between 200 kJ/mol and 330 kJ/mol, which will hardly allow them to form a glass by themselves. They are used to facilitate the fabrication of a glass and modify the physical characteristics and the chemistry of the vitreous matrix. The main intermediate oxides of the network are: Al_2O_3, TiO_2, PbO, ZnO and CdO.
- The network modifiers oxides have a binding energy lower than 200 kJ / mol. They partially break the bonds created by the network and depolymerize the glass. These are essentially alkaline (NaO_2, K_2O and Li_2O) or alkaline earth oxides (CaO, MgO). Due to their low binding energy, the cations that form them are relatively mobile in the glass matrix. Indeed, subjected to temperatures between 200 °C to 500 °C, the bonds of the cations with oxygen break. They can therefore move in the glass and possibly be replaced by other ions. Replacing these modifiers cations with other cations induces a refractive index variation.

IOG1 is an alumino-phosphate glass composed of 60 mol% of P_2O_5, 24 mol % of Na_2O, 13 mol % of Al_2O_3 and the remaining 3 mol % are R_2O_3 with R the sum of rare earth. It is specifically optimized to be used in the fabrication of integrated optics devices by silver sodium ion-exchange [45].

In our case, the glass is co-doped in Erbium (Er) and Ytterbium (Yb) ions with concentrations equal to 2.2 x 10^{26} $m^{-3}$and 3.6 x 10^{26} m^{-3} respectively. Figure 2-1 shows the Er^{3+} and Yb^{3+} energetic levels involved in the amplification of wavelengths around λ_s = 1534 nm, when λ_p = 980 nm is used for optical pumping.

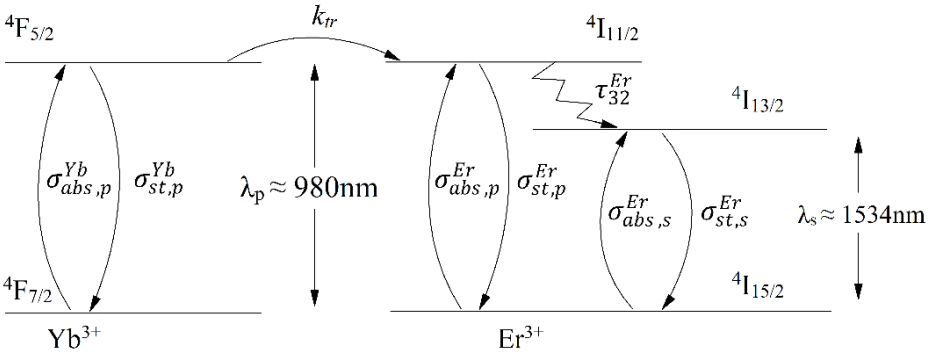

Figure 2-1. Representation of the energetic levels and transitions of Er and Yb ions involved in the amplification aound 1534 nm.

The Erbium atom can be seen as a 3-level system in which the optical pumping excites electrons from their fundamental level $^4I_{15/2}$ to the metastable level $^4I_{13/2}$. $\sigma^{Er}_{abs,p}$ and $\sigma^{Er}_{st,p}$ are the absorption and emission cross sections of the $^4I_{11/2} \leftrightarrow {}^4I_{15/2}$ transition.

When the Er atom is in the excited state $^4I_{11/2}$, it can, by generating some phonons in the vitreous matrix, deexcite non radiatively to the metastable level $^4I_{13/2}$. This transition is characterized by its time constant τ^{Er}_{32}. Finally, a stimulated emission can eventually occur if excited by an adequate wavelength between the $^4I_{13/2}$ and the $^4I_{15/2}$ levels. The absorption and emission cross sections of this transition in IOG1 are represented in Figure 2-2. The emission and absorption cross sections vary differently in function of the wavelength. The Er^{3+} absorption cross section at 980nm is 2 x 10^{-25}m^2. This value is relatively low and produces low linear absorption at $\lambda_{sp.}$

Therefore, to obtain a higher absorption, the IOG1 is co-doped with Ytterbium. As illustrated in Figure 2-1, the transition between the fundamental level $^4F_{7/2}$ and the metastable one $^4F_{5/2}$ of the Yb^{3+} ions will let them absorb and emit photons at λ_p. The absorption and stimulated emission cross sections associated to this transition will be $\sigma^{Yb}_{abs,p}$ and $\sigma^{Yb}_{st,p}$.

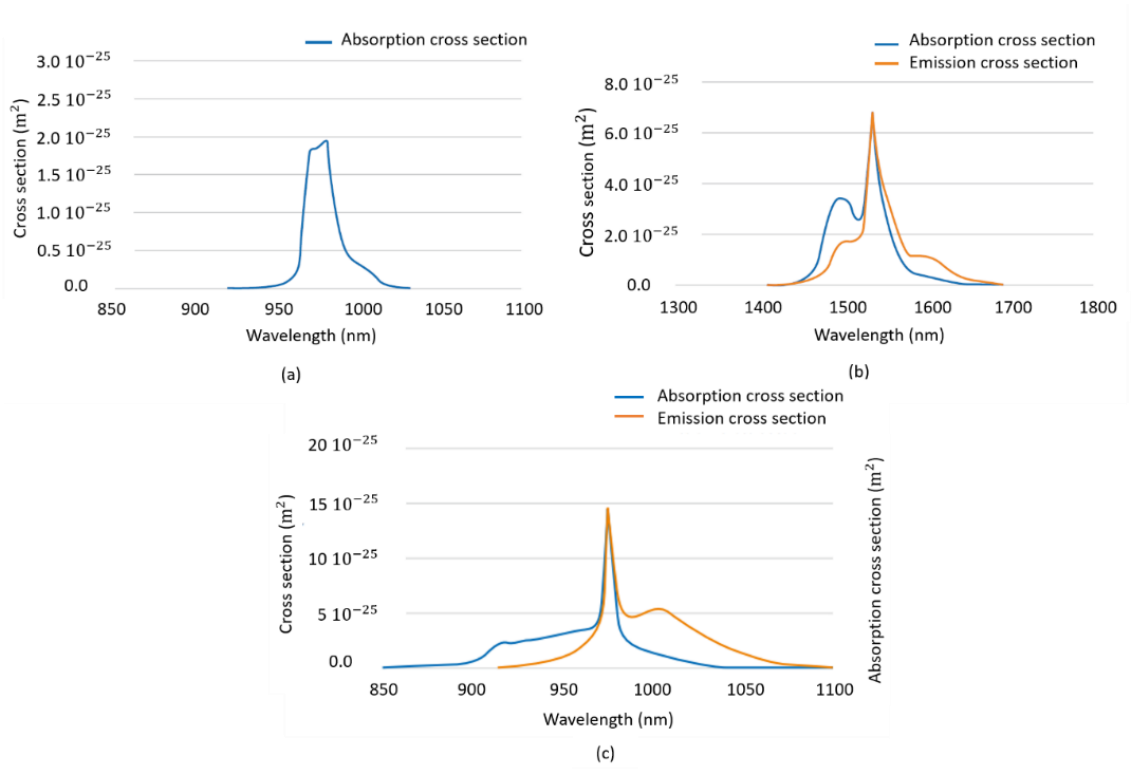

Figure 2-2. (a) absorption cross section around λ_p, (b) absorption and emission cross sections around λ_s for the Er^{3+} ions and (c) absorption and emission cross sections around λ_p for Yb^{3+} ions in IOG1 glass Source: data sheet of the manufacturer [45].

The absorption cross section $\sigma^{Yb}_{abs,p}$ of the $^4F_{7/2} \leftrightarrow {}^4F_{5/2}$ transition reaches, in the case of the Er-Yb co-doped IOG1 glass, a value of 14.5 x $10^{-25} m^2$ at λ_p as shown in Figure 2-2-c. Thus, the probability of absorption of a photon at λ_p is higher with Yb^{3+} than with Er^{3+}. Therefore, the Er-Yb co-doping can artificially increase the Er pump absorption cross section as, if an excited Yb atom is near an Er atom in his fundamental level, an energy transfer between the two ions can occur with a high probability. The transfer rate is higher than 95% [50]. This non-radiative and non-dissipative transfer excites the Er ion from $^4I_{15/2}$ to $^4I_{11/2}$ while the Yb ion deexcites to its fundamental level $^4F_{7/2}$ with a probability defined by the transfer coefficient k_{tr}.

2.2.2 Design of the EYWDA

The waveguides required for our DFB lasers on glass are obtained by silver/sodium ion-exchange done in our Er/Yb co-doped glass substrate. In this section, the principle of ion exchange is first introduced. An in-house model developed to study the diffusion process during ion exchange is then used to simulate the amplifiers modicity. Those tools are finally used to design the optical amplifier.

2.2.2.1 Ion exchange principle

Ion exchange process allows a local modification of the refractive index of the glass in order to fabricate optical waveguides. The first ion-exchanged waveguides on glass were fabricated in 1972 by Izawa and Nakagome [51] into borosilicate glass utilizing a combined $Tl^+ - Na^+$ and $Tl^+ - K^+$ ion exchange. Ion-exchanged waveguides provide several advantages over the other commonly used planar optics waveguide technologies. These include ease of fabrication combined with low propagation loss, good mode field matching with optical fibers, resulting in low fiber-to waveguide coupling losses. A disadvantage with ion exchanged waveguides is that ion exchange produces a relatively low refractive index difference, and therefore bending losses tend to be higher than in etched technologies such as semiconductor-based waveguides. This means that larger bending radii must be used, which leads to an increase in the chip size.

Ion exchange is based on the observation that the glass refractive index depends on its composition. We have seen in section 2.2.1 that in the glass composition, the modifiers of the network are in ionic form in the matrix and that they have relatively low oxygen bond energy. During the ion exchange, the glass is heated to provide the necessary thermal energy to break the modifiers bonds and set the corresponding cations free, without modifying the solid matrix formed by other species. By bringing in contact the glass with a well-chosen ions source (liquid or solid), the ions contained in the source diffuse into the glass while modifiers cations from the glass diffuse outside, thus modifying the glass

composition. The variation of the refractive index with glass composition is noted Δn and it can be calculated using equation (2.1):

$$\Delta n = \frac{c}{V_0}(\Delta R - \frac{R_0 \Delta V}{V_0}) \quad (2.1)$$

with c the normalized concentration in ions of substitution, R_0 and V_0 the refractivity and volume per oxygen mole, and ΔR and ΔV the refractivity and volume variations respectively.

According to equation (2.1), the modification of the glass composition causes the local refractive index variations via two mechanisms:

1- The difference of the polarizability between the exchanged cations: Δn varies proportionally to the difference of the polarizability between the exchanged ions (term ΔR).
2- The volume difference: the more the difference of volume of the exchanged ions is important, the more the glass density and therefore the refractive index is modified. Then, if the volume variation is too significant, the matrix deformation is not elastic. Constraints are created and equation (2.1) is not valid.

To increase the refractive index, the exchanged ions must present either a higher polarizability or a higher ionic radius than the ion initially present in the glass. Table 2-1 presents the different polarizability and ionic radius values of ions commonly used for ion exchange on sodium glass:

Ion exchange	Polarizability ($Å^3$)	Ionic radius (Å)	Linear losses (dB/cm)	Mechanical constraints
Ag^+/Na^+	2.4/0.41	1.26/0.95	0.01	Low
K^+/Na^+	0.43/0.41	1.33/0.95	0.009	High
Tl^+/Na^+	5.3/0.41	1.49/0.95	> 0.2	Very high

Table 2-1 Characteristics of the frequent ions exchanged with sodium [52].

In the works presented in this manuscript, silver/sodium (Ag^+/Na^+) ion exchange is used. This ion exchange allows us, based on Table 2-1, to obtain high quality waveguides, with low mechanical constraints and a relatively high Δn that can reach 0.1 [52]. However, the main disadvantage found throughout many studies of silver exchanged waveguides is the tendency of silver ions to reduce into neutral atoms, subsequently aggregating into metallic clusters in glass and forming an absorbing colloid. This can cause high waveguide losses, particularly for high Ag concentrations. Different

approaches have been taken to decrease these losses, and finally it was understood that glass composition played a key role in the reduction of silver to metallic forms. Particularly, impurity elements residing in the glass structure as polyvalent ions should be avoided. Different glasses structures were developed for this reason, usually by adding aluminum oxide (Al_2O_3), as the IOG1 glass, that is the selected glass in our study.

2.2.2.2 Ion exchange theory

To determine the guiding properties of the structures fabricated using ion exchange, it is necessary to know the refractive index distribution in the exchanged zone. This distribution is linked to the dopants normalized concentration c, which is defined as the ratio between the Ag^+ concentration and the Na^+ concentration present in the glass before the ion exchange, via the relation:

$$n(x,y,z) = n_{sub} + \Delta n_{max} c(x,y,z) \tag{2.2}$$

where, n_{sub} is the refractive index of the un-doped substrate and Δn_{max} is the maximum variation of the refractive index obtained when c = 1 that is the case if the glass is saturated in dopants.

The solution utilized during the ion exchange contains a mixture of $AgNO_3$ and $NaNO_3$ salts. When the glass substrate is in contact with the molten salts during the exchange, a concentration gradient exists at its surface. Thus, the Ag^+ ions substitute the Na^+ ions at the substrate surface at first, until Ag^+ surface concentration c_s is reached. This surface concentration can be computed by [52] equation (2.3):

$$c_s = \frac{x_{Ag} K}{1 + x_{Ag}(K-1)} \tag{2.3}$$

with x_{Ag} is the molar concentration of Ag in the bath, and K the thermodynamic equilibrium constant of the reaction.

Simultaneously, the Ag^+ diffusion into the glass occurs. It is due to dopant concentration gradient in the glass. The temporal evolution of the Ag^+ normalized concentration in the substrate is given by the equation:

$$\frac{\partial c}{\partial t} = -\mathrm{div}\left(\frac{D_{Ag^+}}{1 - \alpha c} \overrightarrow{\mathrm{grad}}\ (c)\right) \tag{2.4}$$

with $\alpha = 1 - D_{Ag^+}/D_{Na^+}$ is Stewart coefficient, and D_{Ag^+} and D_{Na^+} are the Ag^+ and Na^+ diffusion coefficients. A more rigorous description of the diffusion process requires the consideration of mixed alkaline effect. This effect implies a dependency of the diffusion coefficients with the concentration value. The model we use is [53]:

$$\begin{cases} D_{Na^+}(c) = D_{Na_1^+} . e^{A(1-c^2)} \\ D_{Ag^+}(c) = D_{Ag_1^+} . e^{Bc^2} \end{cases} \quad (2.5)$$

where, A and B, are the mixed alkaline coefficients. $D_{Na^+}(c = 1) = D_{Na_1^+}$ so that $D_{Na_1^+}$ represents the diffusion coefficient of sodium ions in the glass when the latter is saturated in dopants. Besides, $D_{Ag_1^+}$ corresponds to the diffusion coefficients of dopants in the vitreous matrix when their concentrations tend toward zero.

The parameters associated to ions diffusion properties in the vitreous matrix for the IOG1 phosphate glass at a temperature equal to 320°C are mentioned in Table 2-2 below [54].

Diffusion parameters	Coefficient value
A	0.3 ± 0.1
B	3.1 ± 0.6
$D_{Na_1^+}(\mu m^2/\min)$	1.5 ± 0.5
$D_{Ag_1^+}(\mu m^2/\min)$	0.6 ± 0.3

Table 2-2. Diffusion coefficients values of the IOG1 glass at T = 320°C [54]

These coefficients were experimentally determined by Bertrand Charlet [54] during his thesis in IMEP-LaHC. Moreover, to avoid the formation of silver clusters on the glass surface, we used the optimum silver nitrate proportion in the ion-exchange bath as calibrated in the thesis of Bertrand Charlet [54]. The corresponding normalized surface concentration was calculated to be c_s = 0.25. Using these coefficients, we are able to perform simulations in order to know the spatial distribution of silver ions in the glass. The results of the simulations are presented in the following section.

2.2.2.3 Fabrication of EYWDA

In this work, the Er/Yb co-doped waveguides, used as the amplification medium of the lasers, are straight waveguides made at the surface of the sample. Their aperture widths are defined thanks to openings in a Silicon masking layer deposited on top of the glass substrate. Silicon has been chosen because it is possible to use dry etching to define the waveguide aperture using a process having a good selectivity with glass. Moreover, Silicon is a good barrier to cation diffusion even with small layer thicknesses such as a few tens of nanometers.

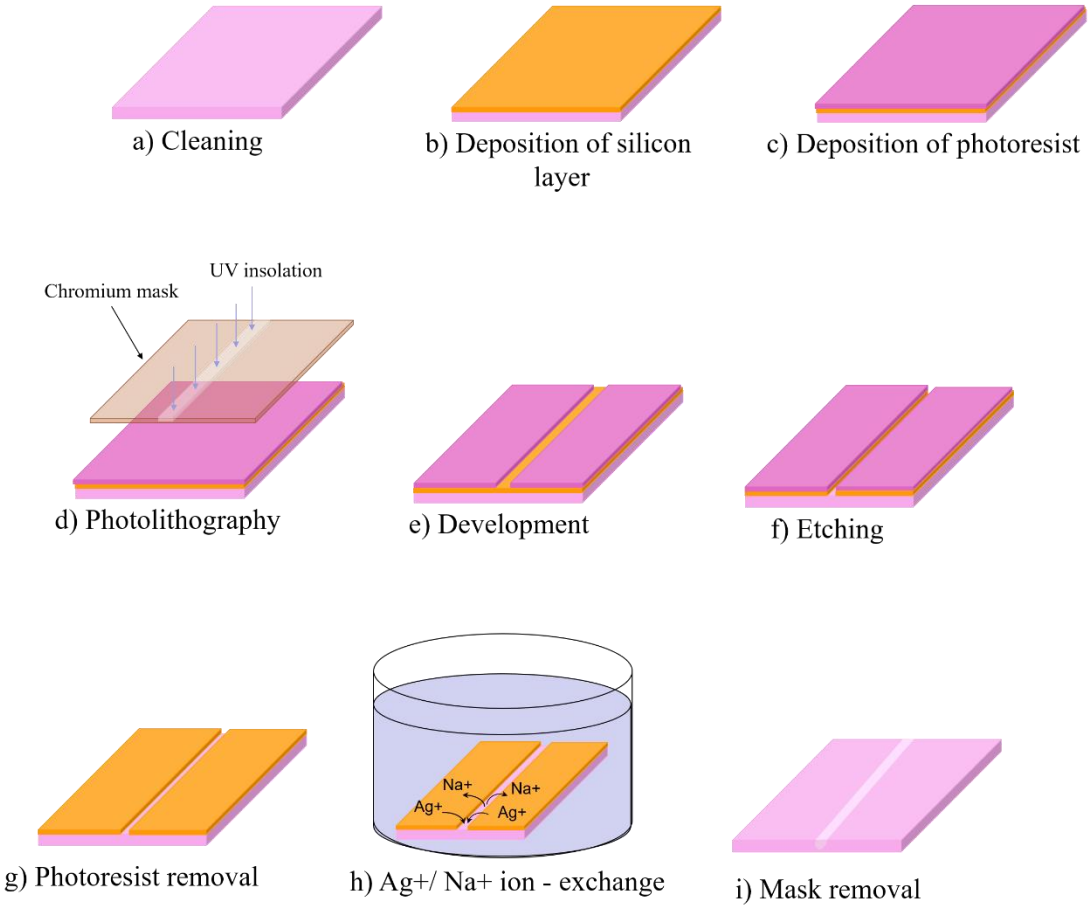

Figure 2-3 Technological fabrication process of EYWDA.

Figure 2-3 depicts the amplifier fabrication process steps. After cleaning the sample (Figure 2-3-a), a 70 nm- thick Silicon film is at first deposited on the glass surface by RF sputtering at 200 °C (Figure 2-3-b). Then a 500 nm-thick positive photoresist is deposited on the Silicon layer (Figure 2-3-c). 4 cm- long straight diffusion apertures with width w are defined by a standard photolithography process (Figure 2-3-d) followed by a development of the exposed photoresist in a developer solution (Figure 2-3-e). After verifying the good inscription of the apertures under the microscope, a 30 s reactive ion etching (RIE) is carried out to etch the aperture in the Silicon layer (Figure 2-3-f). The photoresist is then removed prior to the ion exchange (Figure 2-3-g). The sample is horizontally immersed in a bath of molten $NaNO_3$ and $AgNO_3$ (20 mol%) salt as shown in Figure 2-3-h for a duration t at a temperature of 320 °C. When in contact with air, some Ag^+ions can be reduced to Ag atoms which can create optical losses. To avoid this phenomenon, the glass is immersed for 4s in a bath containing 50 % $NaNO_3$ and 50 % KNO_3 just after the ion exchange in order to create a few nanometer thin Na-doped subsurface layer. After that, the Silicon mask is removed by RIE (Figure 2-3-i) and the sample is cleaned. Finally, the input/output facets of the chip are cut and polished to optical quality.

2.2.2.4 Waveguide design

The waveguide we want to design is composed of a core having a refractive index modified by ion exchange surrounded by unmodified glass acting as a clad. By combining equation (2.4), (2.5) and the parameters in Table 2-2, a concentration map of an exchanged waveguide can be obtained using a numerical in-house developed tool which simulates the diffusion process during ion exchange. Using equation (2.2), the link between the concentration and refractive index profiles can be established. Then, using a mode solver from the commercial software Optiwave, we calculate the effective index and spatial distribution of the electromagnetic field of the guided modes by finite difference.

The ion-exchange temperature and bath composition have been optimized and will be kept identical in this work. However, two more process parameters can still be varied in order to change the guiding properties of our waveguides: ion-exchange duration t and the width w of the diffusion aperture. The simulation results of modicity of the waveguide at λ_s = 1550 nm as function of the waveguide aperture width and ion exchange duration are presented in Figure 2-4. The area of interest in this work is determined by:

1- Transverse single mode waveguide at λ_s
2- The waveguide aperture width (w): 1 µm < w < 10 µm. The reproducibility of the photolithography process is low for w < 1 µm, and for w > 10 µm the coupling losses become more important.
3- Since a higher modal net gain is expected for higher ion-exchange durations [55], we chose to work with durations longer than 5 min.

By combining these criteria, the area delimited by 1 µm < w < 10 µm and t > 5 min is the area of interest. Furthermore, we didn't do any ion exchange duration higher than 10 min because they would require a waveguide aperture width smaller than 1 µm.

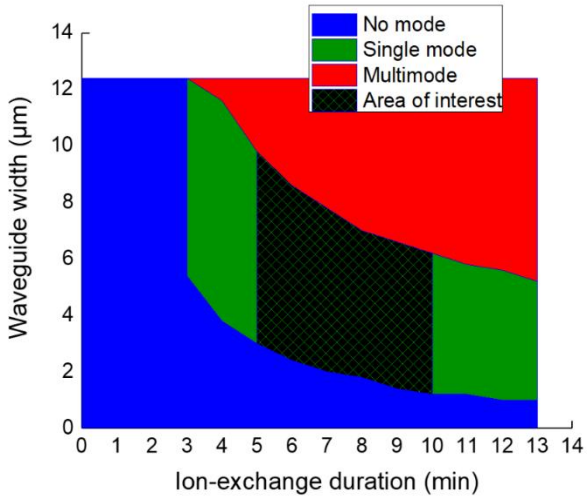

Figure 2-4. Simulated diagram of modicity at the signal wavelength of the ion-exchanged waveguides, as a function of the ion exchange duration t, and the waveguide aperture width w.

It is important to note that, based on simulations and mode distribution measurements which are not presented in this manuscript, most of the waveguides in our area of interest are multimode at λ_p. However, this is not a problem for our devices since slightly multimode amplifiers were proven to be better or similar than strictly single-mode ones in previous works [41].

2.2.3 Characterization of EYWDA

In the following chapters of this manuscript, most of the used lasers have waveguide aperture width between 3.5 µm and 7 µm and ion-exchanged for a 7 min duration. The waveguide with w = 7 µm is mostly used, that is why we present all its characterizations. The optical amplifiers realized with other process parameters all possess comparable characteristics to the one presented.

2.2.3.1 Intensity profile measurement

The setup employed for measuring the output optical intensity profiles of guided modes is represented in Figure 2-5. The sample is maintained by aspiration on a metallic support. Its position can be adjusted thanks to a 3-axis micro-positioners (XYZ). The measurements are done at the signal wavelength λ_s = 1550 nm. The light emitted by a laser at 1550 nm is injected to the input facet of the waveguide via a fiber (SMF28). The microscope objective (x50), allows the focalization of the image coming from the output facet of the waveguide on an infrared camera. For our waveguides, the obtained image is close to the intensity profile of the electromagnetic field of the guided mode. Analyzing this intensity profile allows us to measure the dimensions of the guided modes. Moreover, varying the input coupling conditions allows estimating the waveguide modal distribution at both λ_p and λ_s. We verified

that all the fabricated waveguides between 3.5 µm and 7 µm are single mode at λ_s. The modicity of the waveguides is in an excellent agreement with the simulations (for an exchange duration of 7 minutes, simulations shown in Figure 2-4 predict a single mode behavior for aperture width ranging from 2 µm to 7.8 µm).

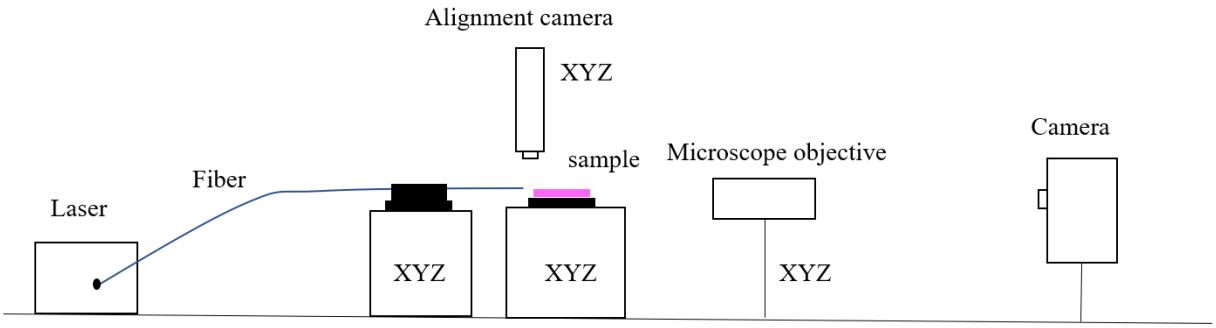

Figure 2-5. Experimental setup for the measurement of intensity profiles of guided modes at λ_p = 980 nm and λ_s = 1550 nm.

As shown in Figure 2-6, the mode profile measurement recorded for a w = 7 µm aperture width waveguide (Figure 2-6-a) is in good agreement with the simulation (Figure 2-6-b).

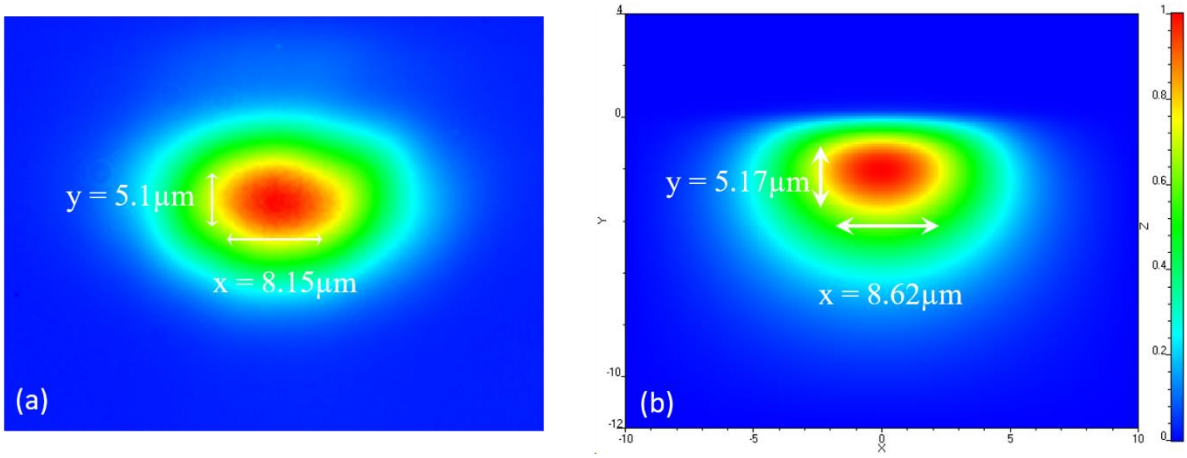

Figure 2-6. Mode profile for a 7 µm wide waveguide ion-exchanged at T= 320 °C for a duration t= 7 min at λs = 1550 nm: a) Measurement and b) Simulation.

2.2.3.2 Gain measurement

The setup used for gain measurement is reported in Figure 2-7. At first, the injected power must be measured. To do so, the pump diode power P_p at the output of the multiplexer is calibrated using a calibrated power-meter. The point A of the multiplexer is spliced to a fiber going to a 980nm power-meter.

Then, the fiber is spliced directly to a fiber at the input of the optical spectrum analyzer (OSA) (point B) to measure the losses α_s^{OSA} induced by the attenuator, multiplexer, fibers connectors and the OSA. Finally, the 980/1550 fiber of the multiplexer is aligned with the waveguides on the sample, and a fiber going to the OSA is aligned from the second side of the sample.

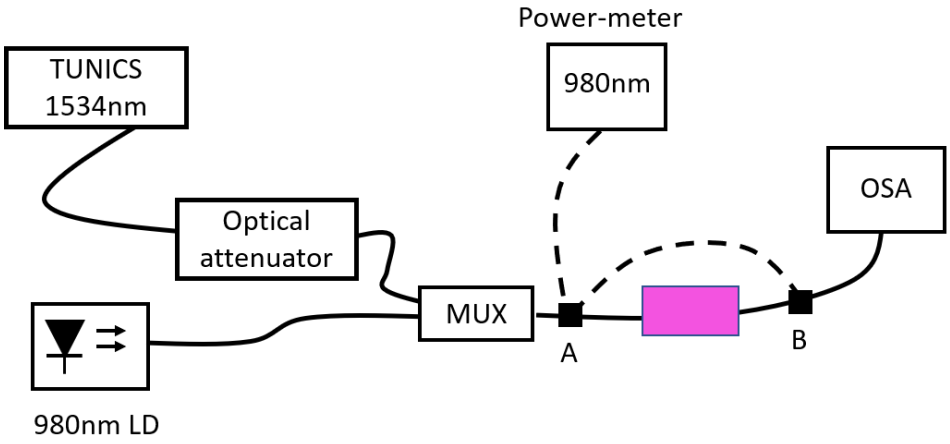

Figure 2-7. Setup used for the amplifier small signal gain measurement. The dashed lines indicate the calibration connection.

The small signal gain measurement is then performed for the different power pump and a signal power at 1534 nm equal to P_s = -20 dBm. After its propagation in the amplifying waveguide, the power has been amplified by a factor G depending on the pump power. Moreover, the amplifying waveguide generates an amplified spontaneous emission (ASE) over the entire range of Er gain. In order to remove the ASE contribution, we take a couple of values for each pump power: the power of ASE, P_{ASE}, at a wavelength near λ_s, and the total power P_{tot} at λ_s. At the signal wavelength, the measured power by the OSA is

$$P_{tot} = G.P_{in} + P_{ASE} \tag{2.6}$$

From which we can compute G using equation 2.7

$$G\,(dB) = 10.\log\left[\frac{P_{tot} - P_{ASE}}{P_s}\right] \tag{2.7}$$

This experiment has been carried out on waveguides having their aperture width between 4 µm and 7 µm. The maximum gain for a 7µm waveguide is measured to be 15.2 dB ± 0.4 dB for an injected pump power P_p = 560 mW as shown in Figure 2-8. The pump power transparency threshold has been measured to be 140 mW.

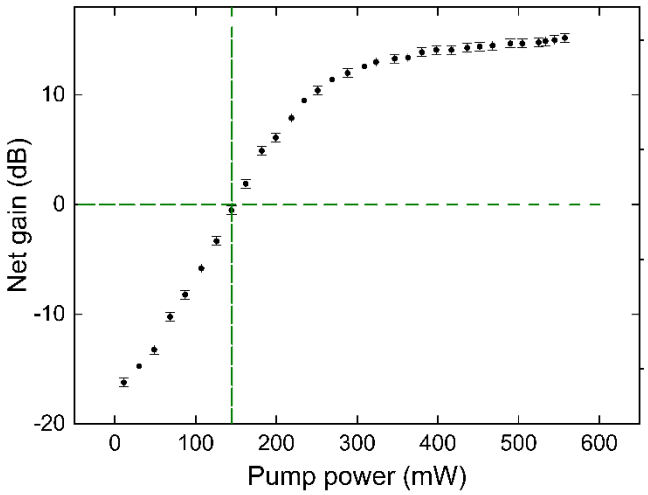

Figure 2-8. Amplifier small signal net gain at λ_s = 1534 nm as a function of pump power.

Figure 2-9 summarizes the measured gain per unit length at P_p= 560 mW pump power for waveguides having different aperture widths. We notice that the different characterized waveguides have comparable gain values, with a slight increase of the gain for larger waveguides. Comparable small signal net gain and transparency have been measured in [56] with amplifiers fabricated with the same Erbium and Ytterbium concentrations.

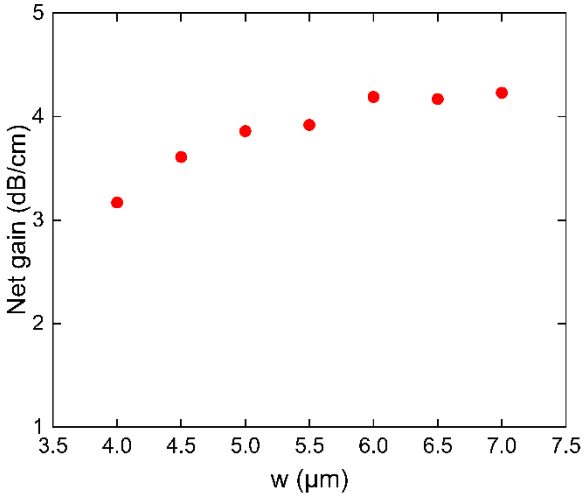

Figure 2-9. Experimental measurement of small signal gain (dB/cm) at λs = 1534 nm as a function of the waveguide apertures. Pp = 550 mW and L= 3.6 cm.

Up to here, the optical amplifier, the first component of the DFB laser, is fabricated and characterized. The fabricated amplifiers have the required characteristics: single mode operation for the signal wavelength and net gain higher than 3dB/cm for the waveguides having their apertures 4 μm < w < 7 μm. The next step is the implementation of the Bragg grating on top of these amplifiers.

2.3 Bragg grating

The feedback element in DFB lasers on glass is a Bragg grating which is used as a wavelength selective mirror. As shown on Figure 2-10, if an optical signal with large spectral bandwidth propagates through the grating, only narrow spectral band, centered at the Bragg wavelength, is reflected. Otherwise, the grating transmits the light without any effect. Bragg wavelength λ_B is defined from the grating step Λ and the waveguide effective index n_{eff} as

$$\lambda_B = 2\Lambda n_{eff} \tag{2.8}$$

In the case where the waveguide is fabricated in an amplifying medium, a lasing effect can occur at wavelengths very close to the Bragg wavelength.

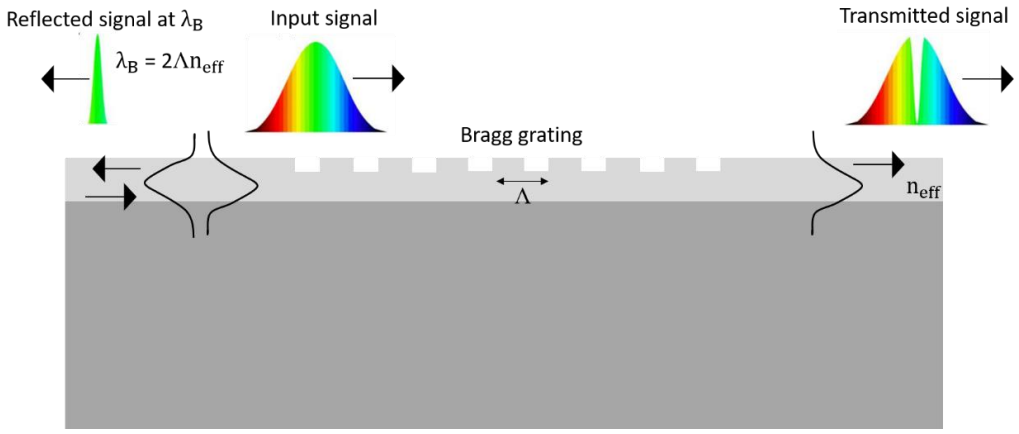

Figure 2-10. Bragg grating description.

2.3.1 Fabrication process

The inscription of the Bragg grating can be done using different photo-inscription techniques. When the Bragg grating step is bigger than the resolution of the photolithography equipment, direct inscription using pre-designed mask [57] can be used. In our case, an interferometric insolation technique is used. As this latter has been employed in IMEP-LAHC laboratory for more than fifteen years for DFB lasers fabrication [40], [42], [58] and [59], we can benefit from the expertise to fabricate grating adapted to our device.

The different fabrication processes and characterization steps are illustrated in Figure 2-11. The first step consists of depositing a 500 nm thick photoresist layer on the substrate using a spin coater (Figure 2-11-a). The sample is then placed on a hotplate at 110 °C for 5 minutes to dry the photoresist. The inscription of the Bragg grating in the photoresist is achieved thanks to an interferometric setup schematized in Figure 2-11-b. A beam at λ = 405 nm from a laser is filtered by a pin hole then collimated

using a lens with a 10 cm diameter and a focal distance equal to 1 meter. The collimated beam illuminates a bracket consisting of two vertical uprights assembled at 90 degrees. On the first upright, a metallic mirror is fixed, the second one is designed to maintain the sample to be exposed. The adjustment of the grating step Λ is realized by setting the angle θ that the mirror forms with the direction of the collimated beam: $\Lambda = \frac{\lambda}{2\sin(\theta)}$ [40]. Each point of the sample is then illuminated by two beams: the direct beam from the laser source and the one reflected by the mirror creating interferences fringes on the sample. On the bright bands, the photoresist is periodically insolated. The development of the photoresist allows us to transfer the fringes pattern on the photoresist with the fringe periodicity (Figure 2-11-c).

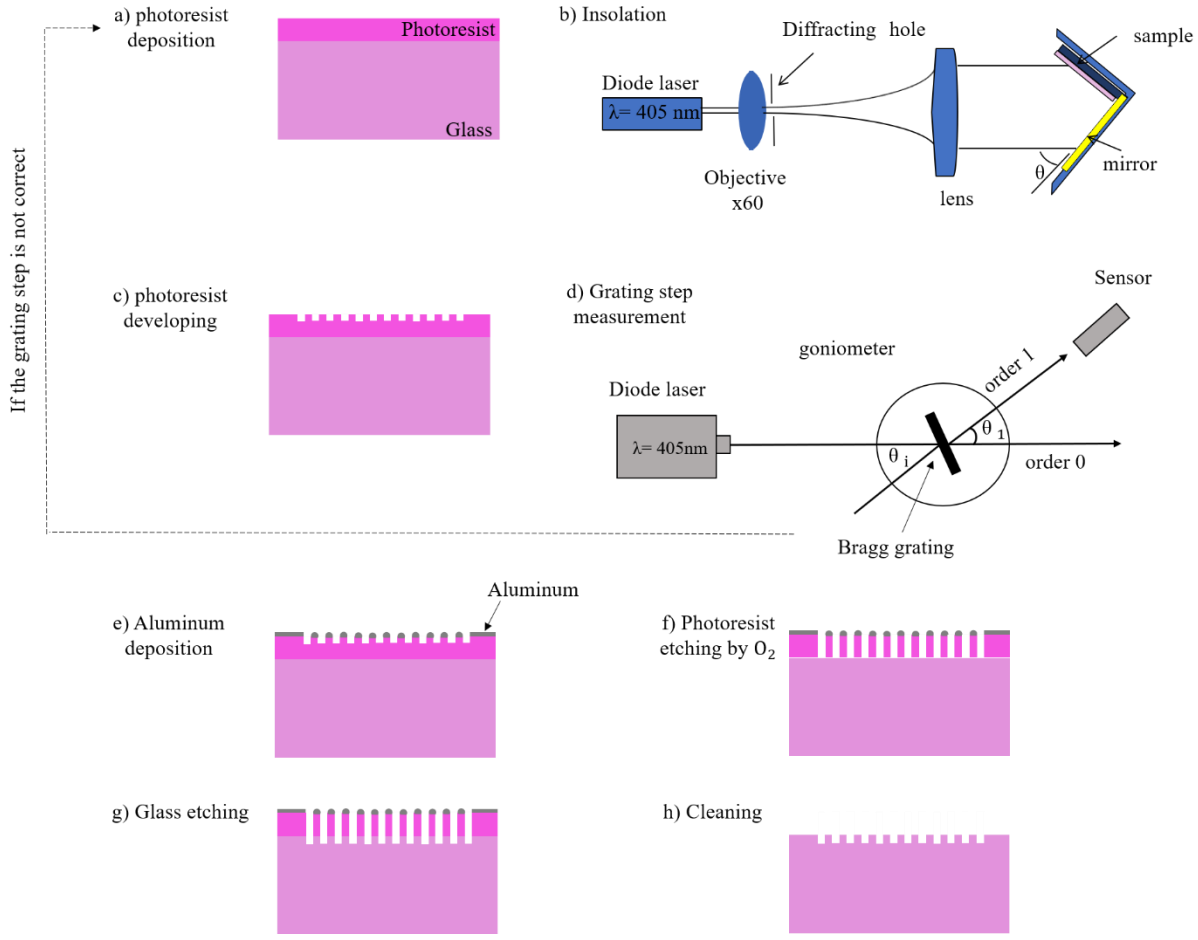

Figure 2-11. Bragg grating fabrication process.

From this step, the Bragg grating step can already be measured thanks to the optical setup utilizing the minimum deviation method as schematized in Figure 2-11-d. During this characterization, the sample is placed on a goniometer and a collimated 405nm wavelength (Toptica Photonics - BlueMode)

laser beam is shined on the grating. Diffracted beams are created by the grating, whose diffraction directions are known as diffraction orders, noted by integer number m. The refraction angle for each order depends on the angle of incidence θ_i, the grating step Λ and the laser beam wavelength λ. There are two angles of incidence for which the angle θ_1 between the diffracted beams at order 1 and 0 is minimal. By measuring the difference between these two angles $\Delta\theta$, the grating step Λ can be obtained using formula (2.9):

$$\Lambda = \frac{\lambda}{2.\sin\frac{\Delta\theta}{4}} \tag{2.9}$$

If the measured grating step does not correspond to the targeted value, the sample is cleaned, and the process is resumed from the beginning with a corrected angle.

Once the correct grating step is measured, next step consists in protecting the grating for the following etching step. A thin layer of Aluminum (Figure 2-11-e) is thus deposited on the crest of the grating by an oblique evaporation of Aluminum.

Before the etching, an O_2 plasma is used for 2 minutes to completely remove the developed photoresist from the grating grooves (Figure 2-11-f). Then the glass is etched by RIE process, using an SF_6 and CHF_3 gas mixture (Figure 2-11-g). This step transfers the grating to the surface of the IOG1 glass. Finally, the sample is cleaned to remove the Aluminum and the photoresist layers (Figure 2-11-h).

A measurement of the topology of the grating can be obtained by Atomic Force Microscope (AFM) imaging as it will be shown later. This measurement allows to see the profile of the grating and its depth. The grating period can also be measured using the AFM image, but a more exact value can be obtained using the bench presented in Figure 2-11-d.

2.3.2 Design of the Bragg grating

The Bragg grating can be seen as a periodic spatial perturbation of the waveguide. In our case, the grating depth is small when compared to the mode size, so that the effect of the grating on a propagating mode can be described using the coupled mode theory. In this work, the theoretical study for the grating design is not presented. We have used the parameters computed during a previous work [40] [60] in the laboratory and we have adapted our fabrication process to obtain similar grating characteristics.

The parameters of the Bragg grating have been previously determined in [40] [60]. The depth of the grating is between 150 nm and 300 nm, the duty cycle ~ 40 % and the step Λ depending on the wavelength emission calculated from the formula $\lambda_B = 2n_{eff}\Lambda$ where, n_{eff} is the waveguide effective index. However, the photoresist developer that had been used previously was changed and the new one

brought problems with the adherence of the photoresist on the IOG1 glass. Also, the existing process had reproducibility issues so that the grating depth after glass etching could vary by 100 % with identical process parameters. For these reasons, I decided to set up new process parameters. Three different set of experiments have been necessary to determine proper process parameters. At first, I focused on obtaining a photoresist grating on the glass surface with good adherence to the glass during the development step (step c on Figure 2-11). Then, another set of experiments has been focused on the reproducibility of the process. Finally, after improving the process, I observed that most lasers would emit light only if pumped from one particular side. A third set of experiment was thus dedicated to improving the symmetry of the fabricated gratings. Those three sets of experiments are detailed hereafter.

2.3.2.1 Adapting the insolation process

The first experiments performed to improve the grating fabrication process are related to the change of the developer used after insolation of the photoresist. Indeed, the first tests with this new developer produced gratings in the photoresist which would detach from the glass. The insolation parameters that were used up to now thus had to be modified. The new values of these parameters and their adjustment range are summarized in Table 2-3.

Parameter	Values
Insolation duration	120 s – 300 s
Developer concentration in water	10 % - 30 %
Development duration	5 s – 60 s

Table 2-3. Tested parameters for adapting the insolation process to the new developer.

Those three parameters are linked together, thus different combinations of these can result in an acceptable grating. For example, for a longer insolation duration, a lower concentration of the developer and a shorter duration of development are required. However, we used the parameters in a way that a reproducible process can be achieved. For example, even if 5 s of development can be good with a specific insolation duration and developer concentration, this duration is too short leading to a relatively big error impacting the reproducibility of the process.

For our process, we fixed the parameters to be 240 s of insolation followed by 20 s of development in a solution with a developer concentration of 15 %. Using these parameters allowed us to obtain a good adhesion of the photoresist and to carry out the next fabrication steps so that we could produce

our first working lasers. However, the adherence of the photoresist on the IOG1 glass was still low, which negatively impacted the reproducibility of this process.

2.3.2.2 Process reproducibility improvements

We investigated the reasons of the low reproducibility of our process. We observed that the photoresist drying process could be improved. Eventually, and after trying different processes, we fixed our drying process to be in an oven at 90 °C for 30 min and waiting at least for two days before the grating insolation. In fact, using the oven instead of the hotplate allowed for a more homogeneous solvent evaporation over the thickness of the photoresist. Moreover, waiting for two days before insolating the photoresist lead to a better adherence of the resist on the glass, although we could not back up this observation with published work for an explanation.

This modification of the drying process leads to a dramatic improvement of our reproducibility issue. However, when we carried the fabrication of the grating to its end and characterized the obtained DFB lasers, we observed that the devices would work as intended, but only if pumped from one particular side. When pumped from the other side, the lasers would emit a much lower output power or even not lase at all. This was a problem for us since some of our experiments involved pumping two lasers of the same chip from opposite sides. We thus decided to investigate this problem before going further in laser characterization.

2.3.2.3 Duty cycle and laser behavior improvements

In order to investigate the non-symmetrical behavior of our lasers, we systematically captured AFM images after each technological step to see the modifications in the grating shape. Figure 2-12 shows three AFM images of the grating after step c (photoresist development), g (glass etching) and h (final cleaning). It is apparent that the shape and duty cycle of the grating is not significantly modified between the development step (Figure 2-12-a) and the grating etching in the glass (Figure 2-12-b). The only difference is the bottom of the grating: in Figure 2-12-a, the curvature at the bottom of the grating denotes the presence of non-developed photoresist whereas in Figure 2-12-b, the flat bottom corresponds to the glass surface after etching. Figure 2-12-c is the AFM image after removing the Aluminum and cleaning the glass surface. We noticed that during this step, the grating has been etched.

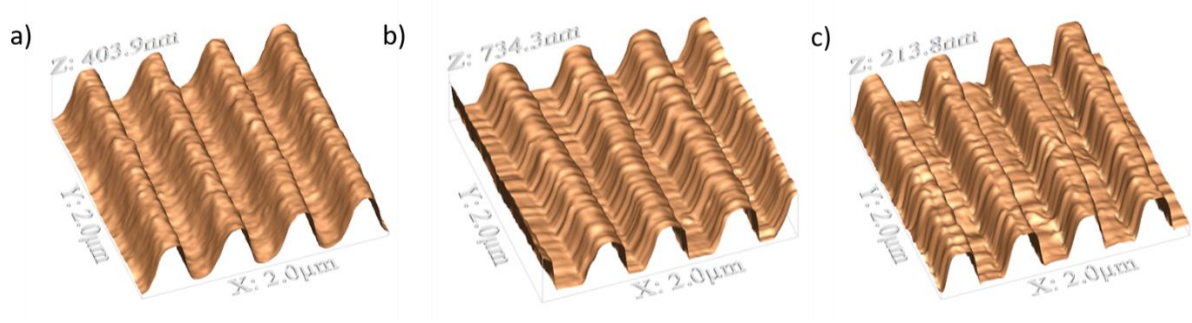

Figure 2-12 AFM image of the grating after a) photoresist deposition, insolation and development, b) after etching the grating in the glass and c) after removing the aluminum and cleaning the sample.

Moreover, during the Aluminum deposition, there is a part on one side of the sample where Aluminum is not deposited, as shown in Figure 2-13-a. This could lead to an etch of the glass (and thus the waveguide surface) on this side of the device during the glass etching process. Further etching of this side of the wafer would also happen during the Aluminum removal process.

We hypothesized that this surface etching was linked to our lasers dissymmetrical behavior. Figure 2-13 shows a more detailed view of what happens during the Aluminum removal process. During this step, the glass is immersed in an Alu-etch solution with stirring for 1 minute (Figure 2-13-b). We analyzed that since the IOG1 glass contains Aluminum in its composition, the Aluminum removal process could also etch our glass.

In order to solve these issues, we modified the two involved process steps. First, to remove the Aluminum without etching, we decided to use remover. Indeed, there is always photoresist under the Aluminum, so that when the remover dissolves the photoresist, the Aluminum comes along. Secondly, during the glass etching step, we covered the unprotected part by a small piece of aluminum, in order to prevent the waveguides from being etched.

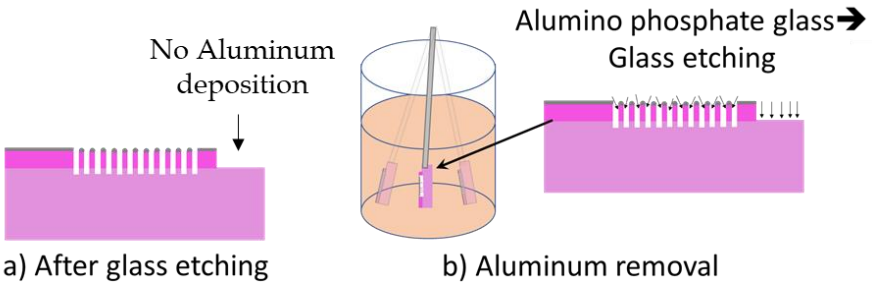

Figure 2-13 Aluminum removal process

Figure 2-14-a and Figure 2-14-b show the shape and the 2-D profile of the grating obtained after using all the fixed parameters. The grating has rectangular shape, an average depth of 145 nm and an average duty cycle of 40 %, which is equivalent to its value before Aluminum removal. It thus seems that our modification of the Aluminum removal step allowed preserving the grating shape.

New lasers have been fabricated with the adjusted Aluminum removal process. These lasers now behave symmetrically with respect to the pump side and they emit higher output power that reaches 41 mW as will be shown in the following section. The grating fabrication process as it was modified is the one that has been used to fabricate all the lasers used in the remainder of this manuscript.

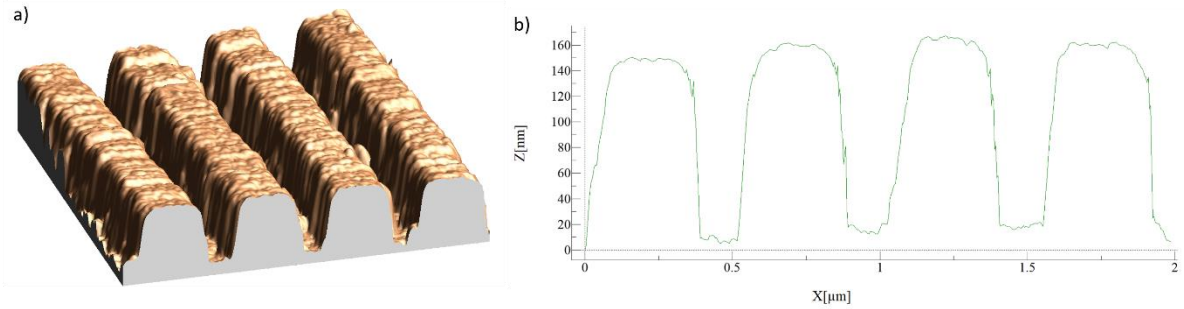

Figure 2-14 Bragg grating a) AFM image, b) profile.

2.4 Laser connectorization

When fabricating an optical device, it is always interesting to connectorize it, so it can be used outside of a testing optical bench. During this work, we used a fiber-glass connectorization process developed by the company Teem Photonics SA.

The connectorization process consists in gluing input/output fibers to the glass chip. Here is a summary of the steps used for this process.

- The chip input facets and the fibered ferrules are polished to optical quality at 98° and 82° respectively.
- Active fiber-waveguide alignment for highest output power of the laser is achieved using 6-axis piezo positioners (10 nm precision). We decided to perform an alignment by injecting pump input and monitoring laser output instead of maximizing the transmission of a signal at 1300 nm for a better reproducibility of the process. During all the process, the optical power and emission wavelength of the laser are monitored using a power-meter and an OSA.

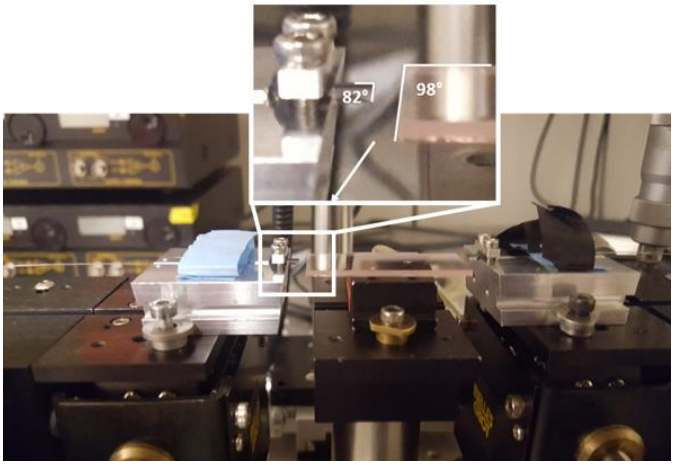

Figure 2-15 Photography of the optical bench on which a 98° polished sample and a 82° ferrule are maintained.

An ultraviolet adhesive glue has been used to bond the ferrule to the glass. We were careful not to allow the glue to reach the optical path since it may degrade under the pump light. The reflection on the interface air/glass and glass/air cause losses between the waveguide and the fiber. These reflections can be mitigated by setting precisely the distance between the fiber and the chip [55]. However, when the glue dries, this distance is changed, and a small reflection may arise. This reflection can destabilize and damage the pump diode and may also change the emission spectrum of our laser. This effect can be suppressed by polishing the input/output facets of the laser at 98° and the injection fiber at 82° as shown in Figure 2-15. The lost power is then reflected outside the waveguide and the fiber.

Once the bonding is done, the connectorized device is installed on a metallic support, as shown on Figure 2-16, that can be thermally controlled by a Peltier module. This Peltier module is itself placed on a heat sink. A thermal paste has been employed to ensure a good thermal coupling between all these elements. A temperature sensor is positioned inside the metal support under the glass chip, so we are able to adjust the temperature of the device.

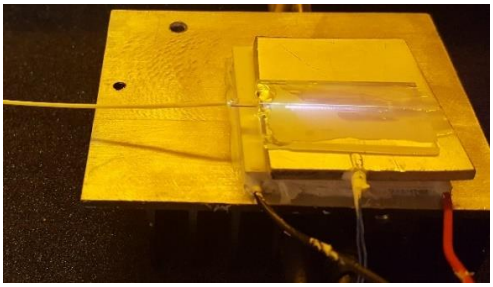

Figure 2-16. Image of a connectorized laser placed on a Peltier module and a heat sink for temperature control.

2.5 Laser characterization

Once all the fabrication and connectorization steps are achieved, the fabricated lasers are characterized. We start with the optical characterization to measure the laser emission wavelength, its output power characteristic and wavelength tunability. Then the laser linewidth and relative intensity noise are measured.

2.5.1 Characteristic $P_s(P_p)$

The characteristic of the laser describes the evolution of the lasing output power with the pump power injected in the device. This characteristic is measured using the setup shown in Figure 2-17. The pump diode is connected to a 980nm / 1550nm multiplexer. A polarization controller (PC) is used to ensure an optimal pumping. The pump power is injected in the device via the common port of the multiplexer. The laser emits in both directions: forward and backward with respect to the pump signal. As it was observed in [41], the laser output power from the backward direction is higher than the one measured in the forward direction. The difference between backward and forward emission efficiencies is related to the absorption of the pump from rare-earth ions during the propagation, which results in decreasing the small signal gain along the laser waveguide [44]. For this reason, the output signal, used for all the measurements in this work, corresponds to the backward signal collected at the signal port of the 980/1550 multiplexer (referred to as P_S^1 in Figure 2-17). This signal is collected from an on-line power-meter and then sent to an OSA.

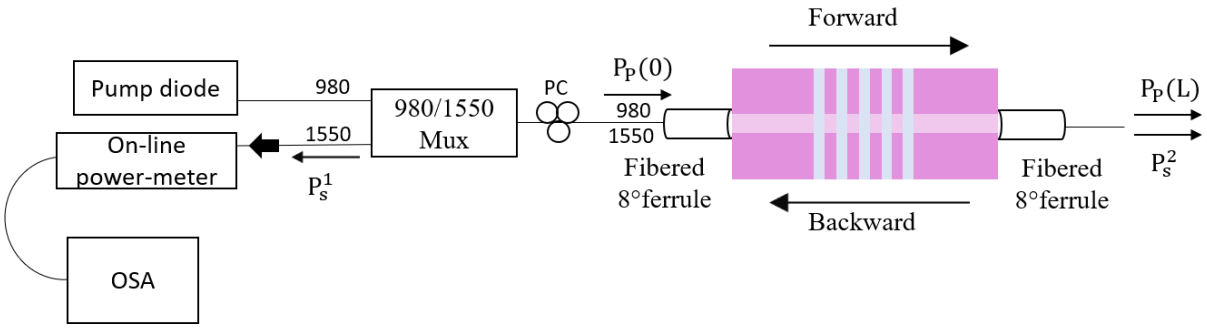

Figure 2-17 Laser output power and emission spectrum measurements setup.

Figure 2-18 depicts the 7 µm width laser fiber-coupled output power versus pump power. The threshold occurs at 140 mW and a 41 mW of optical output power is reached for a maximum pump power of 560 mW. The lasing threshold is very close to the measured transparency of the amplifier, which indicates that our cavity has very low losses. The laser slope efficiency is 9.8%, which is better than the state of art values for glass Erbium lasers on glass [61]. Such lasing threshold has already been measured when the Ytterbium concentration in the glass is higher than the Erbium's [61].

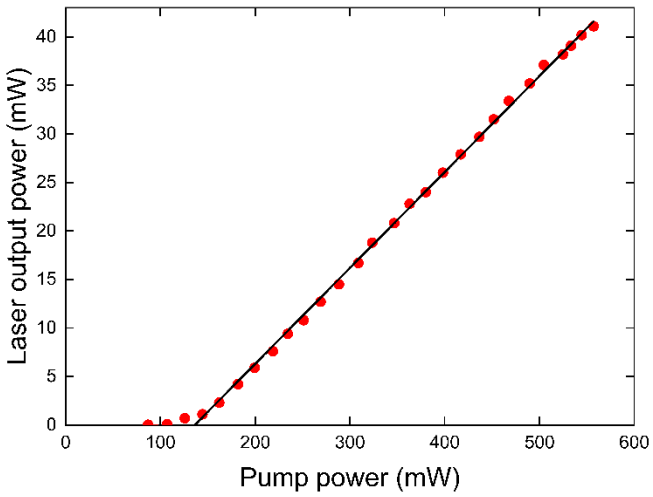

Figure 2-18 Fiber-coupled output power of the laser versus pump power for laser with waveguide aperture width = 7 µm.

Table 2-4 summarizes the measured lasers thresholds and slope efficiencies for the fabricated lasers having different waveguide aperture widths. The propagating field is more confined in the waveguide having bigger aperture widths. That's why 7 µm width waveguide has a higher gain as it was presented in Figure 2-9. Consequently, the fabricated lasers with 7 µm aperture width have lower threshold and better efficiency.

The output power of each of the lasers is higher than the powers obtained with the lasers fabricated in [41] and the efficiency is multiplied by a factor four. The optimization of the grating process is the main element explaining this improvement of the lasers performances.

Width	Threshold	Slope efficiency
4 µm	260 mW	9.1%
6 µm	150 mW	9.6%
7 µm	140 mW	9.8%

Table 2-4 Measured power characteristics of the fabricated lasers with different aperture widths.

2.5.2 Emission wavelength

The main use of the fabricated lasers in this work is the generation of mm-wave carriers by beating two lasers of a photodiode. The frequency f of the generated carrier depends on the emission wavelengths λ_1 and λ_2 of the two lasers as shown in equation 2.10

$$f = c\frac{\lambda_2 - \lambda_1}{\lambda_2\lambda_1} \tag{2.10}$$

It is thus important to be able to design with precision the emission wavelength of each laser prior to its fabrication in order to generate the required frequency. The emission wavelength of a DFB laser is

$$\lambda_B = 2n_{eff}(w,t)\Lambda \tag{2.11}$$

where $n_{eff}(w,t)$ is the effective index of the lasing mode for a waveguide having an aperture width w, and a duration t of ion exchange, and Λ is the Bragg grating step. Theoretically, DFB laser on glass emits with two wavelengths. To avoid that, a phase shift has to be inserted in the waveguide or the grating to select only one wavelength. Our lasers have been fabricated without any phase shift, but most of them emitted a single wavelength. Moreover, even with lasers emitting two wavelengths, we were always able to obtain a single wavelength emission by modifying the optical coupling of the pump input fiber. Note that during the work of this thesis, a lithography mask containing waveguides with phase shifts has been designed but we couldn't characterize them for lack of time.

To measure the emission wavelength of the fabricated lasers, we used the setup depicted in Figure 2-17 and the optical spectrum are observed on an OSA having a resolution of 0.07 nm.

In the following two subsections, the variation of the emission wavelength λ of a single mode laser with pump power and chip temperature are given. This measurement of the tunability is limited by the OSA resolution (0.07 nm). More accurate performances will be given in chapter 3 by measuring the tunability of a frequency generated by beating two lasers.

2.5.2.1 Wavelength thermal sensitivity

When using single mode lasers for radio frequency (RF) generation, it is frequent that two semiconductor lasers emitting at the same wavelength when they are used at the same temperature. The frequency control of the RF carrier is then ensured by tuning the temperature of at least one of the two lasers to adjust its wavelength. For that reason, we wanted to measure the frequency variation of our lasers relative to the thermal tuning.

This measurement has been carried out using a laser chip mounted on a Peltier module as presented previously. The emission wavelength and the emission power have been monitored for different temperatures of the metal plate supporting the laser chip. The laser temperature has been varied from 10 °C to 70 °C. As can be seen on Figure 2-19, the wavelength shifts of ~ 0.82nm. This shift corresponds to a thermal sensitivity of 13.6 pm/°C. This value is slightly higher but of the same order of magnitude than the previously measured sensitivity equal to 11.4 pm/°C [58]. The difference between those two

results may be explained by a change in the measurement protocol: temperature of the chip was set in [58] by setting the whole chip in an oven. Power fluctuations have also been measured as a function of the temperature. It is interesting to see that we have not observed any significant change in the laser optical power at low (10 °C) (11.3 dBm) and high (70 °C) (11.39 dBm) temperatures. This indicates that there is no limitation to thermal wavelength tunability linked to the material constituting the optical cavity. For the moment, the only observed thermal limitations are due to the Peltier module limited between 10 °C and 70 °C and to the glue used for connectorization, which loses its strength for temperature higher than 70 °C.

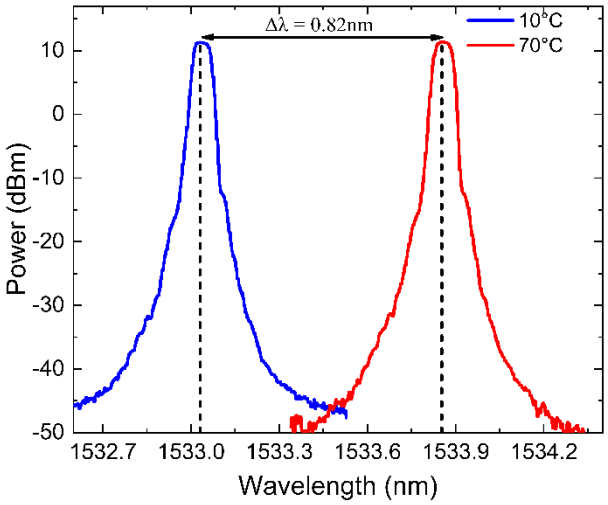

Figure 2-19 Laser emission spectra at 10 °C and 70 °C.

2.5.2.2 Wavelength vs pump power

In addition to the thermal sensitivity of our lasers to tune the laser wavelength, the wavelength variation linked to the pump power variation can be considered as finer tuning as the pump power injected into the waveguides can induce additional temperature variation on the waveguides. The emission wavelength of the 7 µm width laser has been measured without and with thermal control for two values of the pump power: the first is slightly higher than the lasing threshold and the second is the highest pump power (560 mW) that can be obtained by our 980 nm LD. Figure 2-20-a and Figure 2-20-b depict the obtained spectra without and with thermal regulation respectively. Wavelength shifts equal to 30 pm and 10 pm have been measured leading to an average variation of 0.07 pm/mW and 0.02 pm/mW without thermal control and with thermal control respectively. These values correspond to a frequency tunability equal to 9 MHz/mW and 3 MHz/mW respectively if two lasers are used for RF generation. The measured wavelength shift values are lower than OSA resolution (0.07 nm) and

thus, our confidence in these values is low. However, the difference between the two measurements shows that our thermal control is efficient as it reduces by a factor of ~3 the pump power impact.

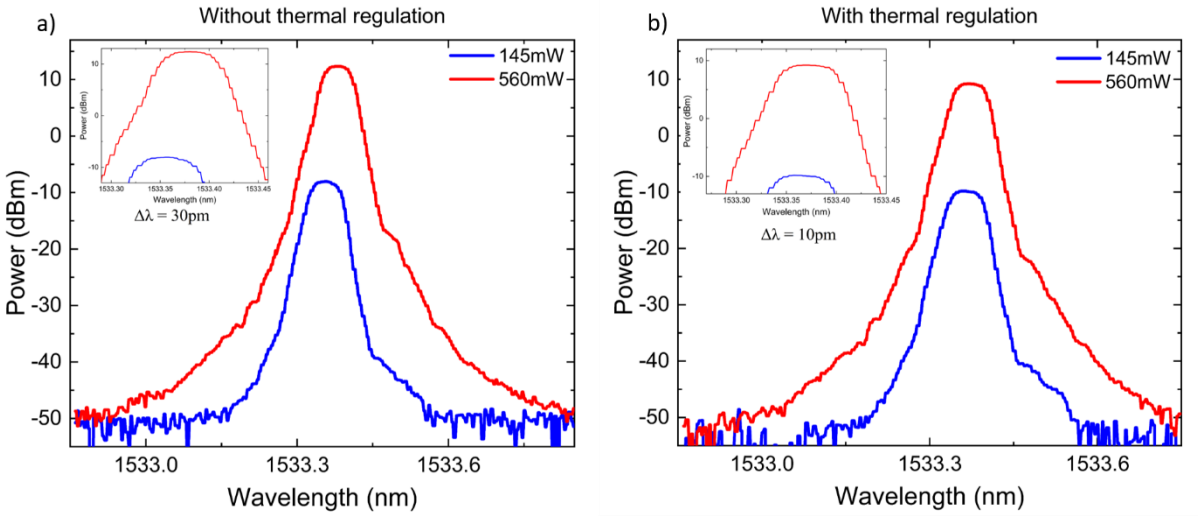

Figure 2-20 Optical spectra of the laser for different launched pump powers a) without and b) with thermal control.

2.5.3 Linewidth

The ultra-narrow linewidth of DFB lasers on glass has already been proved using a similar fabrication process [41]. Figure 2-21 illustrates the self- heterodyning setup that has been realized to perform linewidth measurements. The light emitted from a laser is split in the arms of an unbalanced Mach-Zehnder interferometer. One arm is a 25 km long fiber to decorrelate the signals in the two arms, and on the second arm an acousto-optic modulator is used to frequency shift by 40 MHz the laser signal. As a consequence, a beating signal around 40 MHz is obtained on the rapid photodiode (PD). The resulting spectrum is observed on an electrical spectrum analyzer (ESA) to extract the laser linewidth.

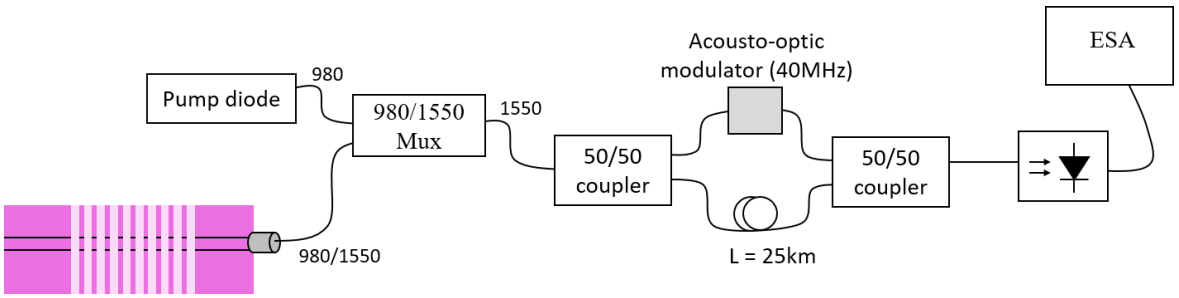

Figure 2-21 Self-heterodyning setup used for linewidth measurement.

Figure 2-22 depicts the acquired spectrum for the optical linewidth measurement for a sweep time equal to 50 ms and a resolution bandwidth of 1 kHz. It has not been possible to fit the curve using a

Lorentzian distribution, but a Voigt profile allowed obtaining a good agreement with the measurement. The obtained Voigt fit contains a gaussian and a Lorentzian contributions having a full width at half maximum (FWHM) of 20kHz and 4 kHz respectively. Considering only the Lorentzian contribution, the laser optical linewidth is equal to 2 kHz. Further work would be needed to understand if the Gaussian contribution is linked to the setup used for this measurement or if it comes from the laser itself. We chose not to follow this path as there is already much work to be done with the beating signal as will be shown in the next chapters.

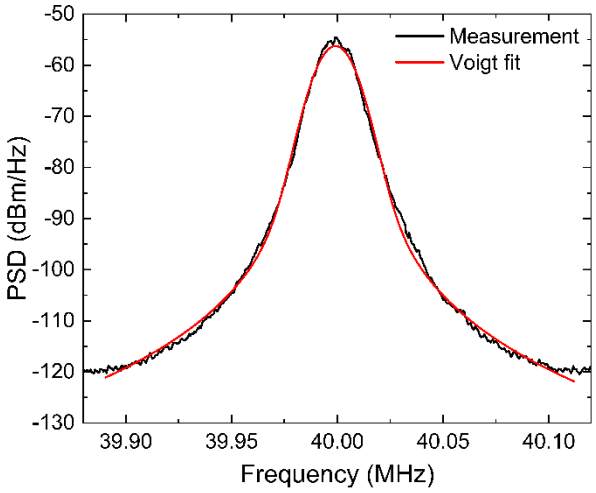

Figure 2-22 Linewidth measurement using self-heterodyning setup.

2.5.4 Relative intensity noise

The relative intensity noise (RIN) of the laser consists in characterizing the fluctuations of the laser output power. This characterization is done in the electrical domain in order to observe the low frequencies fluctuations. To do so, the setup represented in Figure 2-23 is used. The emitted signal with 3 mW optical power of the 7 µm width laser is sent via a single mode fiber to a photodiode, then the electrical signal spectrum is analyzed on an ESA.

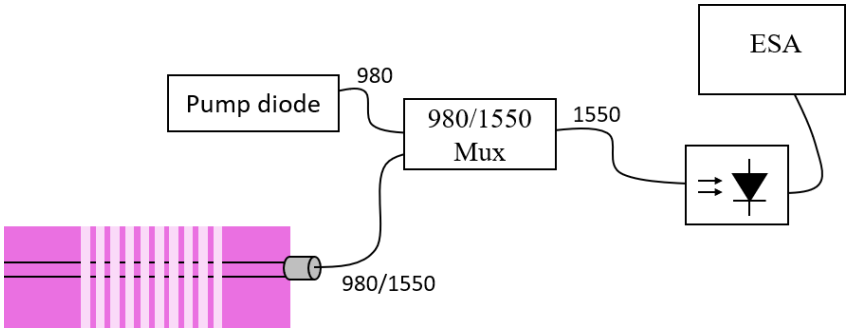

Figure 2-23 Relative intensity noise measurement setup.

The noise measured by the ESA is the sum of three contributions which are the shot noise, the thermal noise and the RIN of the laser. Since we want to measure only the RIN, the two other contributions have to be removed. The shot noise is equivalent to an intensity noise of -150 dB/Hz for 1 mW of laser optical power. In the case the noise is estimated higher than the shot noise, the shot noise contribution can be neglected in most of the cases. The thermal noise of the system can be measured by turning the laser off and extracted from the total noise.

The RIN is defined by the formula (2.12):

$$\mathrm{RIN} = \frac{< \Delta P_{out}^2 >}{< \mathrm{Popt} >^2} \tag{2.12}$$

As the measurement is performed in electrical domain and not optical domain, it can also be expressed as a function of the average electrical power $<P_{elec}>$ and the electrical power spectral density N_{RIN} induced by the optical noise by the formula (2.13):

$$\mathrm{RIN} = \frac{N_{RIN}}{< \mathrm{Pelec} >} \tag{2.13}$$

This relation can be obtained by calculating $P_{elec} = R.<I>^2 = R.(\eta. <Popt>)^2$ where R is the input resistance of the ESA and η the responsivity of the photodiode.

Figure 2-24 shows the measured RIN and a fitting model for it. After subtracting the thermal noise, a peak of RIN equal to -84 dB/Hz is observed at the relaxation frequency equal to 480 kHz. The excellent correlation between measurements and the model allows us to conclude that RIN goes below -120 dB/Hz after 5 MHz and that no additional noise is present. We also verified that there is no excess noise at other frequencies and the absence of beat-note at higher frequencies confirms the single-mode operation of our lasers. For frequencies higher than 5 MHz, the intensity noise is low enough (< -120 dB/Hz) to impact the quality in communication systems according to the IEEE standards.

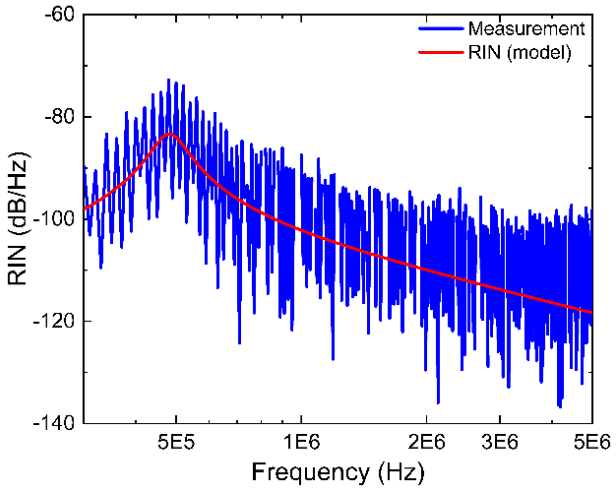

Figure 2-24: Relative intensity noise measurement and fit.

2.6 Summary

We presented in this chapter the fabrication and characterization of DFB lasers on Er/Yb co-doped glass. At first, the ion exchange technology has been presented. An in-house developed diffusion model has been used to design single mode waveguides at 1550 nm. An amplifier having 7 µm width has been characterized and it has a small signal net gain of 4.2 dB/cm. Bragg grating implementation process has been improved, grating with a duty cycle of ~ 40%, a depth of 145nm and a step equal to 510 ± 1 nm have been inscribed on the amplifiers. Fiber-chip connectorization has been presented. Then, one 7 µm laser has been characterized. The laser emits at 1533.3 nm at 25 °C an output optical power equal to 41 mW for 560 mW of pump power. Its efficiency is as high as 9.8% with a lasing threshold of 140 mW pump power. A thermal sensitivity equal to 13.6 pm/°C has been measured by varying the laser temperature between 10 °C and 70 °C. Similar optical powers have been measured at low and high temperatures. A wavelength shift in the order of tenth of pm has been measured for a pump power variation of 415 mW. Laser linewidth and RIN have been finally measured to be 2 kHz and lower than -120 dB/Hz after 5 MHz respectively.

All these characteristics are comparable and sometimes better than the state of the art for glass DFB lasers. They also prove that our lasers are good candidates for optical telecommunications and for mm-wave carrier generation. In the next chapter, carriers generated by the beating of two different lasers are presented and characterized.

3 Millimeter-wave generation using free-running DFB lasers on glass

3.1 Introduction

In this chapter, two DFB lasers on glass, are used to generate mm-wave carriers by heterodyning. Using this technique when employing free running DFB semiconductor lasers, results in generated signals having a lack in stability and large linewidth [62]. For this reason, electrical and/or optical feedback loops are generally used to stabilize the generated carrier and enable communication applications. One goal of this work is the generation of a mm-wave signal that fulfills the ECMA [12] and the IEEE [13] standards in communication systems using only free-running lasers.

DFB lasers on glass possess a narrow linewidth as measured in [63] and in the chapter 2 of this manuscript. Thus, combining such lasers with the heterodyning technique is expected to result in a narrow-generated carrier even at high frequencies.

Before going through the experimental mm-wave carrier generation and characterization, some simulations results for frequency generation based on the diffusion model that has been used in chapter 2 are presented. These simulations have two goals: firstly, the prediction of the possible frequencies that can be generated using two free-running DFB lasers on glass and secondly, the identification of the impact of fabrication tolerance of each fabrication parameter on the generated frequencies.

In the second section of this chapter, the experimental generation of mm-wave carriers using independent DFB lasers on glass is carried out. The carriers' stability has been studied through three different configurations for the lasers. The impact of the lasers' thermal control and thermal coupling on the generated frequencies are highlighted. Generated carriers are characterized, and data transmission measurements using three different modulation formats are performed: BPSK, QPSK and 16QAM. We show a strong correlation between the carrier stability and the data transmission performances.

3.2 Generated frequencies range

As presented in chapter 2, using optical sources, the generated frequency f is defined using the formula (3.1):

$$f = c\frac{\lambda_2 - \lambda_1}{\lambda_1\lambda_2} \tag{3.1}$$

where λ_i are the emission wavelengths of the two optical sources. In the case of single mode DFB lasers on glass, the emission wavelength is linked to technological parameters through:

$$\lambda = 2n_{eff}(w,t)\Lambda \tag{3.2}$$

where $n_{eff}(w,t)$ is the effective refractive index of the lasing mode for a waveguide having an aperture width w and a duration t of ion exchange, and Λ is the Bragg grating step. Any of these parameters w, t and Λ may be adjusted to change the emission wavelength of a DFB laser. A schematic representation of a laser along with the technological parameters that can be adjusted is depicted in Figure 3-1.

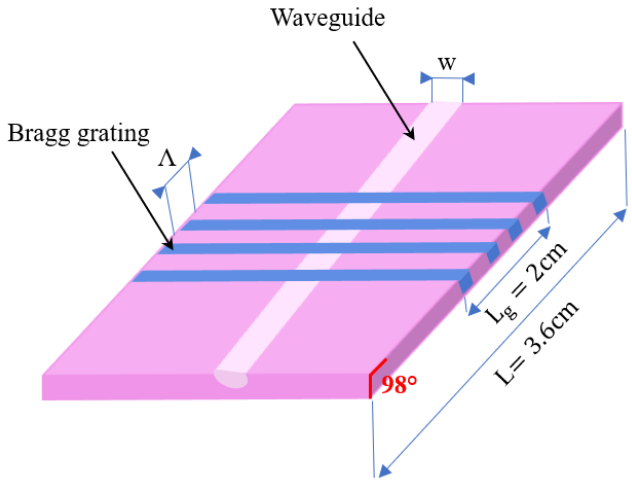

Figure 3-1 Schematic representation of the DFB laser on glass.

In the next subsections, the impact of each of these technological parameters on the individual laser emission wavelength is evaluated, to demonstrate how they can be used to adjust the frequency generated by heterodyning two different lasers using equation (3.1) and equation (3.2).

3.2.1 Bragg grating step Λ

DFB lasers on Er/Yb co-doped phosphate glass emit at wavelengths contained within the Erbium emission spectrum. For fixed values of w and t parameters, any wavelength within this spectrum can be covered by adjusting the Bragg grating step Λ. Indeed, with the grating fabrication setup presented in the chapter 2, grating step can be varied over values corresponding to Bragg wavelengths ranging from 1000 nm to 1700 nm, which fully contain the Erbium emission wavelength range.

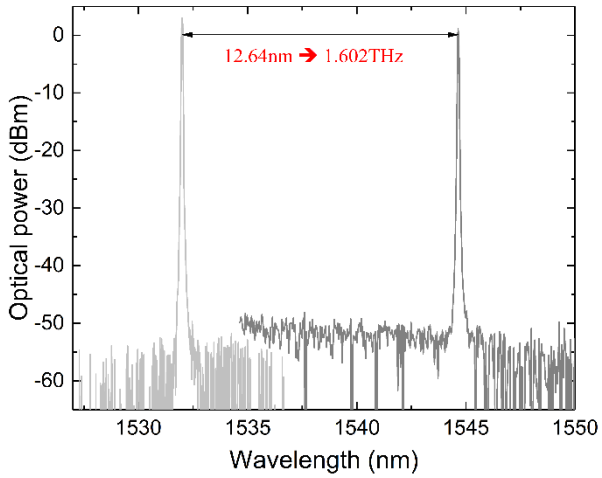

Figure 3-2 Experimentally available frequency range.

Figure 3-2 shows two spectra generated for this study emitted from two different lasers. The grating step Λ has been varied between 507 nm and 512 nm while the waveguide parameters, w = 4 μm and t = 7 min, have been kept unchanged. The 12.64 nm difference between the emitted wavelengths corresponds to a potential generated frequency of 1.6 THz. This value could be increased to reach potentially 8.8 THz corresponding to a 70 nm of continuous emission as it has been shown in [64] for Erbium doped fiber lasers. Such high frequencies are more interesting in applications such as THz imaging. Since this work is aimed at communication applications, we were not interested in fabricating lasers that can generate such high frequencies. However, it is already interesting, for future applications, to know that we can reach 1.6 THz without any modification to our lasers design, and that this value may be increased up to 8.8 THz.

As it has been shown, varying the grating step can lead to the generation of frequencies in the THz range. However, the precision of the grating step adjustment using our fabrication process is limited to ±0.5 nm, which is equal to a precision of ~200 GHz on the generated frequency. It is thus insufficient to obtain a precise value of the carrier frequency for applications in the mm-wave range (30 GHz - 300 GHz).

3.2.2 Waveguide effective index neff

The effective refractive index n_{eff} of each waveguide can be set by adjusting different technological parameters. The two most influent and easy to control are the waveguide aperture width w and the ion-exchange duration t. The impact of these two parameters on the effective index has been simulated using the in-house model developed to study the diffusion processes during ion-exchange [52] and commercial mode solver presented in chapter 2. Figure 3-3 depicts the simulated effective refractive index increase during the ion exchange compared to the non-exchanged refractive index for different waveguide aperture widths and different ion exchange durations. The simulation results highlight the increase in the effective index variation as the waveguide aperture width w and the diffusion time t increase.

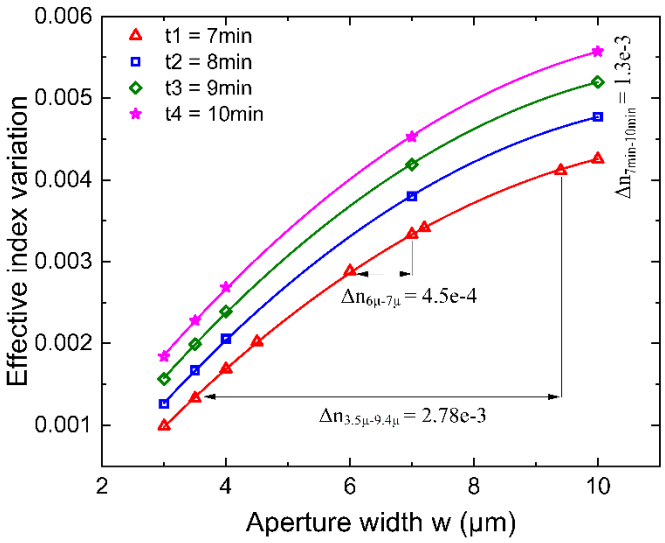

Figure 3-3 Simulated effective index variation of waveguides Δn_{eff} during ion exchange as a function of the waveguide aperture width w for different ion exchange durations t.

The values of both parameters w and t are kept within practical limits that both ensure the realization of a reproducible Δn_{eff} value and the single-mode operation of the lasers. The effective index n_{eff} of the waveguide is bound by n_{sub} and $n_{sub} + \Delta n_{max}$, with n_{sub} the glass refractive index equal to 1.507 and Δn_{max}= 0.08 the maximum possible refractive index due to ion exchange for the salt concentration used in our process [52]. Although, as strictly single mode lasers are required, the modicity of the waveguides limits the effective index that can be used. The effective index variation range presented in Figure 3-3 corresponds to this maximum theoretical value, which shows that changing the w and t parameters allows obtaining all the possible n_{eff} values.

3.2.2.1 Fabrication process accuracy

Before presenting the measurements and comparing them with the simulations, it is important to study the impact of the fabrication tolerance of each parameter on the laser emission wavelength and thus on the generated frequency. As in any fabrication process, many tolerances can lead to a variability in the resulting device characteristics. At first, we identified the different parameters that can have an impact on the guided mode effective index and then we conducted a tolerancing study using the diffusion model previously described and used. The different parameters are the following:

- Waveguide aperture width (w)
- Silver concentration in the salt used for the ion exchange (c_s)
- Flash duration (t_f)
- Ion exchange duration (t)

Moreover, we did this study for four different waveguide aperture widths: 3.5 µm, 6 µm, 7 µm and 9.4 µm to see if we have the same impact for the different widths and at different frequencies. Table 3-1 summarizes the different studied parameters and their possible tolerances during the fabrication process. These tolerances are based on various considerations. Concerning the waveguide aperture width w, it has been measured using an optical microscope on multiple fabrication runs and a variation of ±0.2 µm has been observed. The surface concentration parameter c_s has its tolerance linked to the precision of the weighting machine used to weight the salts composing the ion-exchange bath. Finally, the tolerance for t_f and t_{ech} come from the operator since the samples are plunged manually in the ion-exchange and flash baths.

Parameter	Standard value	tolerances
w (µm)	3.5; 6; 7; 9.4	±0.2 µm
c_s	20 %	±0.1 %
t_f	4 s	±2 s
t_{ech}	7 min	±10 s

Table 3-1 Different simulations parameters.

Diffusion and mode-solving calculations have been carried-out using the standard values of all parameters except one, for which the minimum and maximum values have been used. In order to have meaningful results, instead of presenting the effective index obtained in each case, we computed the frequency generated from the beating of lasers with w =3.5 µm and 9 µm in the first case and w = 6 µm and 7µm in the second case. The simulations results are compiled in Table 3-2. The calculated frequencies were done supposing the lasers were fabricated simultaneously so that they all have the same value of the grating step Λ that we suppose equal to 508nm. For each technological parameter, there are three corresponding values to each couple of lasers: the frequency variation when the varied parameter is minimum (Δf_{neg}), the frequency obtained for the standard value (f) and the frequency variation when the parameter is maximum (Δf_{pos}). The results in Table 3-2 show that the frequency variations depend on the value of the waveguides apertures widths, which comes from the non-linear relationship between the waveguide aperture width and the effective index (as seen in Figure 3-3). For example, for a variation of +10 s on the ion exchange duration, the frequency increases by 3 GHz when generated using w = 3.5 µm and 9.4 µm lasers, whilst it only increases by 0.47 GHz in the case of 6 µm and 7 µm apertures widths lasers. Also, for the same parameter, the variation of the generated frequency is not exactly the same depending on the tolerance if it is positive or negative. Finally, we can observe that the parameter with the most influence on the uncertainty of the obtained frequency is

the diffusion aperture width w, while the uncertainty on the surface concentration c_s has a minor effect due to the good precision of the weighting machine.

Overall, when heterodyning the 6 µm and 7 µm lasers, a frequency of 56 GHz < 58.57 GHz < 61 GHz is expected. And in the case of 3.5 µm and 9.4 µm lasers, a frequency of 346.7 GHz < 360.58 GHz < 375 GHz is predicted.

Parameter	$f_{3.5 - 9.4µm}$ (GHz)			$f_{6 - 7µm}$ (GHz)		
	Δf_{neg}	f	Δf_{pos}	Δf_{neg}	f	Δf_{pos}
w	+12.79	360.58	-12.62	+2.33	58.57	-2.26
c_s	-0.772	360.58	+0.773	-0.119	58.57	+0.11
t_f	+5.5	360.58	-5	+0.76	58.57	-0.7
t_{ech}	-3.14	360.58	+3	-0.49	58.57	+0.47

Table 3-2 Simulation results: fabrication parameters tolerances' impact on the emission wavelength and the generated frequencies supposing Λ = 508nm.

3.2.2.2 Waveguide aperture width w

Now that we have the range of the expected generated frequencies using the fabricated lasers, we can proceed to the measurements.

Figure 3-4 depicts the different measured lasers optical spectra for an ion exchange duration t = 7 min, the grating step Λ = 508 nm ± 0.5 nm and different aperture widths w varying between 3.5 µm and 9.4 µm. These lasers have been fabricated simultaneously so the grating step fabrication tolerance has no impact on the generated frequencies.

We only use the waveguides having aperture widths equal to 3.5 µm, 6 µm, 7 µm and 9.4 µm to compare the measurements with the simulations. The other lasers are used in further measurements in the chapter.

Considering lasers with aperture widths equal to 6 µm and 7 µm respectively, the measured wavelengths show that using these two lasers, a generated frequency equal to 48 GHz ± 8 GHz can be produced. The ±8 GHz corresponds to the OSA precision. For lasers with the same technological parameters, the simulations predict a generated frequency between 56 GHz and 62 GHz. Considering the lasers having w = 3.5 µm and 9.4 µm, measurements show a generated frequency equal to 314 GHz ± 8 GHz. Simulations predicted a generated frequency between 346 GHz and 375 GHz. We thus conclude that the simulations results are higher than the measurements.

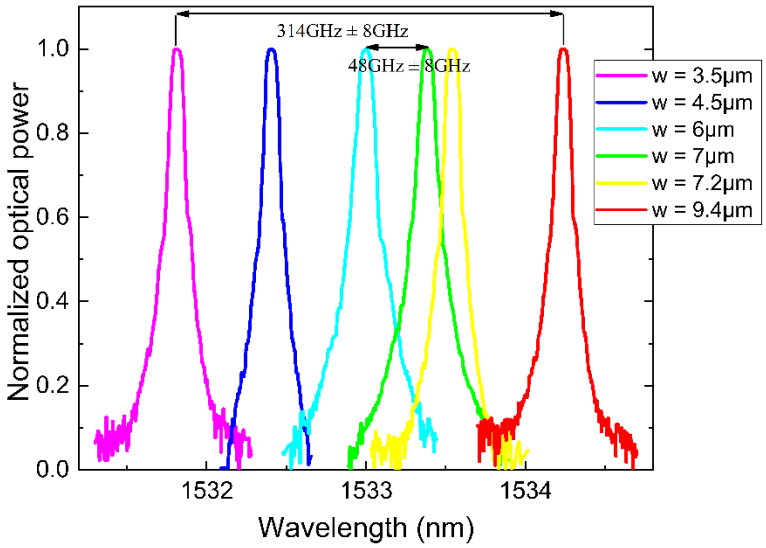

Figure 3-4 Measured lasers emission spectra for different aperture widths, Λ= 508 nm and t = 7 min.

Similar evolutions are obtained for ion exchange durations from 7 min to 10 min. These results demonstrate that frequencies up to ~314 GHz can be generated while keeping identical grating step Λ and ion-exchange duration t. This allows covering the entire millimeter frequency range (30 GHz to 300 GHz) while fabricating simultaneously the two lasers with the same fabrication process (same t and Λ) and an adequately designed photolithography mask.

3.2.2.3 Ion exchange duration

Simulation results presented in Figure 3-3 indicate that two lasers, fabricated with equal waveguide aperture widths of 10 µm and grating step Λ = 511 nm, but with two different ion-exchange durations from t = 7 min to 10 min will have an effective index difference $\Delta n = 1.31 \times 10^{-3}$. Such refractive index difference would correspond to a beating frequency of 160 GHz. We have experimentally measured that, for 7 min < t < 10 min, the lasers having an aperture width up to w = 10 µm are single mode.

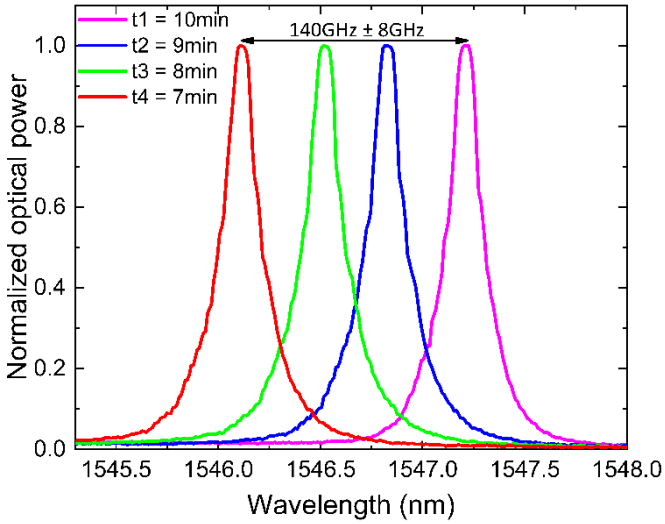

Figure 3-5 Lasers emission spectra measured for w= 10 µm and t = 7 min, 8 min, 9 min and 10 min respectively.

Figure 3-5 shows the measured spectra on devices having the same parameters used in simulations. Frequency up to 140 GHz ± 8 GHz can be generated for w =10 µm and t from 7 min to 10 min. The measurements are thus in good agreement with the simulations. As predicted by the simulations, the available frequencies obtainable by varying the ion-exchange duration are lower than those obtained by varying the waveguide aperture width. It is also more difficult to co-integrate two lasers with different ion-exchange durations. However, the precision on the generated frequency is better, as will be proved in next section.

3.2.2.4 Modification of the ion-exchange simulation

The experimental results obtained in the last two sub-sections are relatively far from the results computed from the simulations and the generated frequencies in all our experiments were systematically smaller than expected. One explanation could be that the way we model our ion-exchange process is incorrect. Indeed, after the ion-exchange and the flash processes, we systematically wait for 210s before washing the substrate in order to ensure the glass temperature is close enough to room temperature and there is no risk of thermal shock. For this duration, the diffusion of ions inside the glass continues, but we did not use to consider it for our simulations.

I decided to simulate this by adding a third diffusion step after ion-exchange and flash. This step was computed at temperatures considering a linear decrease (30 s for each 35 °C decrease from 270 °C to 25 °C) for a duration of 210 s. Adding this third step changed the value of the calculated refractive index and thus the value of the generated frequency decreased. Table 3-3 presents the results obtained

with this new simulation protocol along with the corresponding experimental measurements. We can observe that simulation and experiment are now much closer and majorly within the predicted accuracy.

	Old simulation [GHz]	New simulation [GHz]	Measurement [GHz]
w (6 µm & 7 µm)	58.57	47	48 ± 8
w (3.5 µm & 9.4 µm)	360.58	279	314 ± 8
t (7 min & 10 min)	160	137	140 ± 8

Table 3-3 Comparison of the possible generated frequencies between simulations (old and new) and the measurements.

3.2.3 Discussion

We demonstrated that the three technological parameters Bragg grating step Λ, waveguide aperture width w and ion-exchange duration t can be adjusted during the fabrication process to select the emission wavelength of the lasers and thus the frequency generated by photomixing two of these lasers. The grating step Λ can be used for a large frequency variation, potentially up to 8.8 THz, but is limited to a precision of ± 200 GHz, due to its fabrication process.

For a medium adjustment range, the waveguide aperture width w can be adapted to control the frequencies within a 279 GHz range with a precision of ± 12 GHz, corresponding to lithography process precision.

Then, for a fine adjustment, the ion-exchange durations t can be selected to adjust the beating frequency within a range of 137 GHz with a precision of ± 5 GHz, determined by the ion exchange process precision.

Combining the different technological parameter adjustments and the thermal and pump power tunability, our devices are thus able to generate any frequency in the THz domain with sub-GHz accuracy while keeping a narrow linewidth.

3.3 Thermal sensitivity and dependency of the generated carrier frequency using two free-running DFB lasers

The first heterodyning experiment has been performed using two similar lasers emitting at a wavelength of 1536.5 nm at 25 °C. Those two lasers have been installed on two different heat sinks as depicted in Figure 3-6. Their temperatures have been controlled using two different temperature controllers in order to independently tune the lasers wavelengths and thus control the generated beating

frequency. Thermal wavelength sensitivity and thermal power sensitivity have been studied before characterizing the beating signal at 54 GHz.

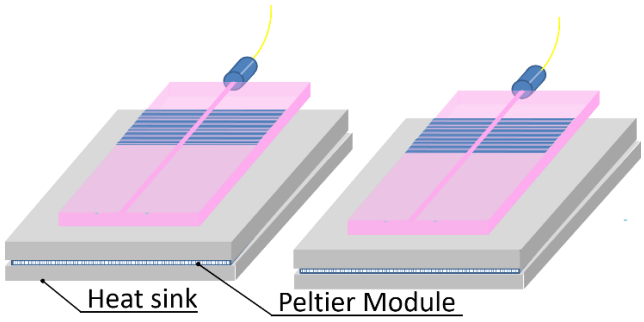

Figure 3-6 Two lasers individually thermally controlled.

For all the measurements performed with two free-running DFB lasers in this chapter, the experimental setup is the same as presented in Figure 3-7. The two lasers are pumped by two 977 nm laser diodes (LD) through a 980/1550 nm multiplexer. The backward signals emitted by the lasers are collected on the 1550 nm ports of the multiplexers followed by 20 dB optical isolators. The signals emitted by the two DFB laser cavities are merged via a 3 dB fiber coupler. The electrical carrier is produced by a 70 GHz bandwidth photodiode having a responsivity of 0.6 A/W. For frequencies between 0 GHz and 40 GHz, an ESA (ANRITSU MS2668C) is used is visualize the signal. When the generated frequencies are between 50 GHz and 65 GHz, the signal is down-converted using a mixer (50 GHz – 65 GHz) having 6 dB loss in combination with a RF local oscillator (LO).

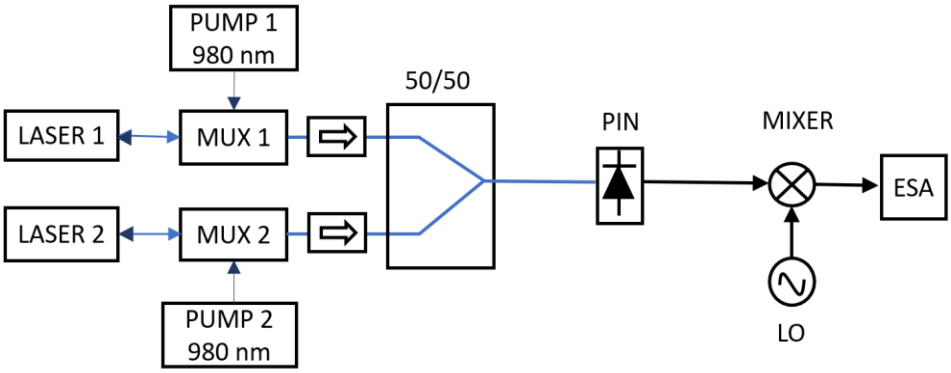

Figure 3-7 Experimental setup for mm-wave generation.

3.3.1 Generated frequency tunability

Since the two lasers are placed on distinct heat sinks, a mm-wave carrier can be obtained by setting different temperatures for each laser. Varying the temperature modifies the laser cavity parameters and

thus the emitted wavelength [41]. The two parameters defining the beating frequency, that are modified with the temperature are the grating step Λ and the refractive index of the glass. The grating step variation is due to the glass thermal expansion $\frac{1}{L}\frac{dL}{dT}$ that is equal in our case to 112 x 10^{-7} °C^{-1} [45] whilst the variation of the glass refractive index is linked to its thermal coefficient $\frac{dn}{dT}$ which is unfortunately not given by the glass manufacturer. The relative temperature difference between the two lasers is set by the two temperature controllers whose accuracies are ±0.1 °C. The two used lasers in this measurement have been fabricated separately with the following technological parameters: w 7 µm, t = 7 min and Λ = 509 nm. At first, both lasers' temperatures have been set to 25 °C. A signal at 1 GHz has been generated, which is well inside our reproducibility uncertainty of ± 12 GHz (as shown in part 3.2). Then, the temperature of one laser has been varied between 10 °C and 67 °C while maintaining the temperature of the second laser constant at 25 °C. Figure 3-8 shows the measured frequency difference for the various temperature differences. Frequency differences from -30 GHz to 56.2 GHz have been obtained. This corresponds to a tunability of 86.2 GHz for a relative temperature difference ΔT= 57 °C between the two lasers. The generated frequency has a nearly linear dependency to the temperature difference, with a thermal sensitivity of 1.49 GHz/°C. This value is slightly higher than the thermal sensitivity previously measured in [41]. This is due to the difference in the glass thermal expansion and the difference in the measurement method as in [41], the laser temperature was changed by putting the laser in an oven.

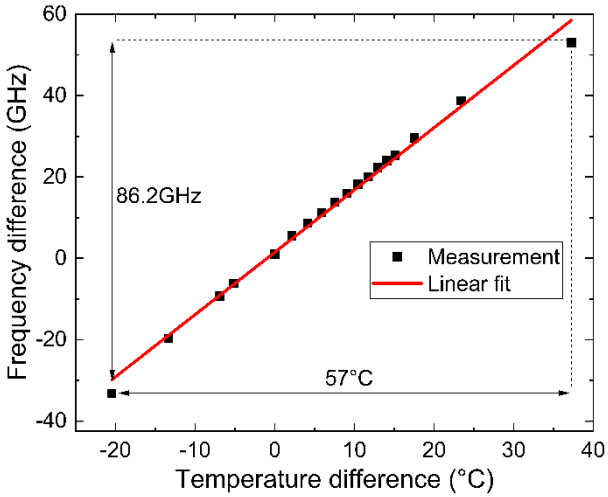

Figure 3-8 Experimentally measured thermal tunability of the generated frequency.

Higher frequencies could be reached by increasing the temperature difference between the lasers, but this would require a better performance of the heat dissipation and thermal regulation. The thermal

control is also limited by the glue used for the fiber-chip assembly. The one used in this work cannot support temperature higher than 70°C.

3.3.2 Power stability

After measuring the thermal tunability of the generated frequencies, their electrical power at different lasers temperatures has been measured. It is interesting to measure the power stability at different temperatures to demonstrate that when a laser is heated or cooled, only its wavelength is modified. Also, if varying the temperatures of two lasers identically, the generated frequency should ideally stay stable with identical performance (power, linewidth…). To avoid the presence of any power variation linked to modifications in the measurement setup, we limit the frequency variation to values lower than 40 GHz to perform all the measurements using the same setup.

The measured lasers temperatures couples are shown in Figure 3-9. The first series of pairs of lasers temperatures, represented in full circles and full triangles in Figure 3-9, have been chosen to study the impact of the generated frequencies on the electrical and optical powers.

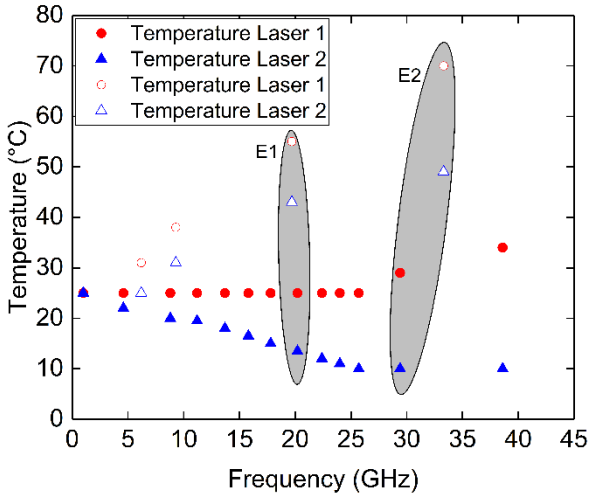

Figure 3-9 Generated frequencies for different lasers temperatures setting couples.

It is also possible to generate identical frequencies using different temperature settings. To study the impact of different temperature settings, a second series of measurement, represented by the empty symbols in Figure 3-9 and Figure 3-10, have been performed. Ellipse 1 (E1) contains the two couples of lasers temperatures (30 °C; 10 °C) and (55 °C; 43 °C). The difference between the temperatures of the lasers for each couple is around 13 °C leading to a generated frequency around 20 GHz. Ellipse 2 (E2) contains the two couples of lasers temperatures (30 °C; 10 °C) and (70 °C; 49 °C). The experiment linked to E2 corresponds to a signal at ~30 GHz from a laser temperature difference of ~20 °C.

Figure 3-10 presents the measured optical and electrical powers for each of the lasers couples. The powers measured for each beating are illustrated in corresponding full squares and full triangles respectively in Figure 3-10. Experiments corresponding to empty symbols in Figure 3-9 are also reported. The average optical and electrical powers were measured to be 4.6 dBm and -62 dBm respectively. The value of the electrical power is lower than expected because we had an issue with one of the electrical cables at the time of the measurement. Beating measurements with good cables are reported later (in 3.4 for example) and an electrical power better than -40 dBm is systematically obtained.

It can be seen in Figure 3-10 that the optical and electrical power keep a relatively constant value whatever the generated frequency. Moreover, for a given frequency and two different temperature sets, optical and electrical powers are also similar. At 20 GHz, the optical and electrical powers vary by only 0.1 dB and 1 dB respectively for the two studied lasers couples in ellipse E1. At 30 GHz (ellipse E2), the optical and electrical powers only vary by 0.3 dB and 5 dB respectively.

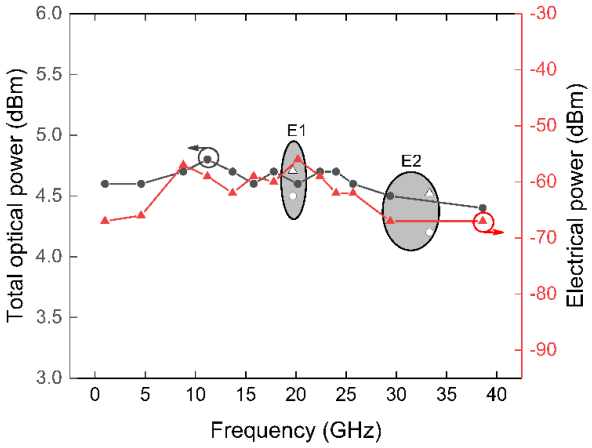

Figure 3-10. Optical and electrical powers for different generated frequencies.

The optical power variations are ± 0.3 dB for the frequencies from 0 GHz up to 40 GHz. For these optical powers, the corresponding electrical power variations were ± 5 dB. The observed optical and electrical power variations can be explained by a small coupling variation between the input fiber and the laser chip when temperature changes.

We accentuate that the chip can withstand low and high temperatures without any significant variation in the electrical power of the generated signal. For the moment, only thermal limitations due to the Peltier module and to the glue capabilities have been observed. Indeed, the laser chips have the same behavior for all temperatures from 10 °C to 70 °C.

3.4 Linewidth and frequency stability

After we presented the technological parameters that can be adjusted to fabricate lasers emitting at different wavelengths and the frequency thermal tunability, in this section the experimental generation and characterization of radio carriers generated by heterodyning two DFB lasers on glass are performed. In this measurement, we start from the last setup where the two lasers have been installed on two separate heat sinks and their temperatures have been fixed independently. We will then modify this setup and show we can improve the stability of the generated carrier frequency by thermally coupling the two laser chips.

3.4.1 DFB Lasers independently thermally controlled

In order to characterize a frequency in the mm-wave range, the differential temperature between two identical lasers (Figure 3-6) has been set to 38 °C.

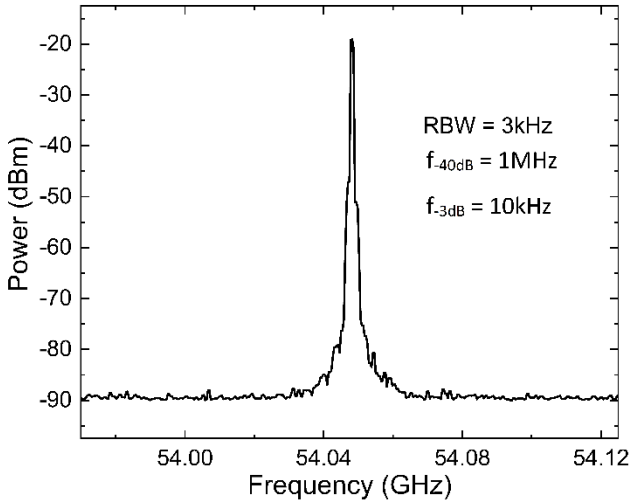

Figure 3-11 Electrical spectrum of the generated signal obtained for ΔT =38 °C for a sweep time of 100 ms.

Figure 3-11 depicts the acquired spectrum of the generated carrier at 54 GHz. The -40 dB linewidth is 1 MHz. This corresponds to a -3 dB linewidth equal to 10 kHz if a Lorentzian shape is assumed. This value is, to our knowledge, the narrowest obtained linewidth for a signal generated using two free-running DFB lasers with no feedback loop. Moreover, the measured signal to noise ratio (SNR) is higher than 70 dB with no spurious in the electrical spectrum.

To qualify the frequency stability, a frequency deviation measurement has been carried out using the max-hold function on the ESA. Figure 3-12 shows a total deviation lower than 36 MHz over a total acquisition duration of 7 s, which corresponds to a deviation equal to ±334 ppm from the 54 GHz

central frequency. The 7 s duration is long enough to be able to perform data transmission measurements. This frequency deviation value is still higher than the IEEE standards (±20 ppm) [13] even though it is already fulfilling the standards in Japan (±500 ppm) [65]. To our knowledge, there is no such deviation measurement in the literature for mm-wave carriers generated using free-running DFB lasers, so it is very difficult to compare the performances of our lasers to other published devices. In order to alleviate this issue, we will present later on data transmission experiments, which may be used to compare to other technologies.

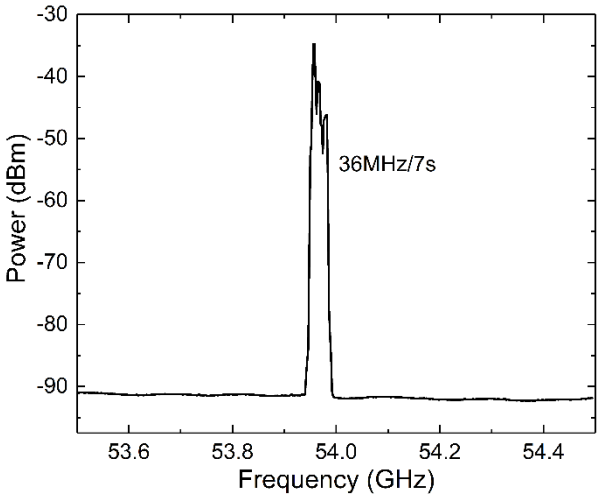

Figure 3-12. Measured frequency deviation for 7s using two free-running DFB lasers on glass.

Using the measured 1.49 GHz/°C thermal sensitivity of the lasers, this deviation may be interpreted as a variation of the relative temperature ΔT equal to 2.4×10^{-2} °C between the two lasers. Such a temperature variation falls within the ±0.1°C control loop accuracy of the used temperature controllers. We thus think that this deviation is not inherent to our lasers and may be decreased by using better temperature controllers.

A mere 0.02 °C fluctuation, that is lower than the accuracy of our temperature controllers, could thus explain the measured frequency deviation. In order to reduce the deviation induced by differential temperature fluctuations between the lasers, the influence of the thermal management on the stability of the generated carrier has been studied by comparing the three following configurations:

- Configuration A (corresponds to the already performed measurements): the two lasers are installed on two separate heat sinks and their temperature are fixed independently (Figure 3-6).
- Configuration B: the lasers are kept on two separate heat sinks without any active thermal control (Figure 3-13-a).

- Configuration C the two lasers are installed on the same heat sink and no temperature controller is used (Figure 3-13-c).

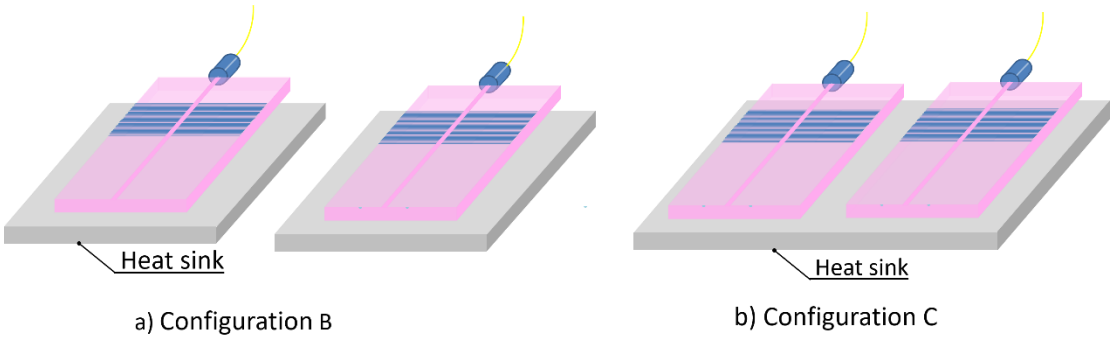

Figure 3-13 Schematic of the new configurations a) configuration B and b) configuration C.

3.4.2 Configuration B: two lasers without thermal control

In configuration A, one cause of the frequency deviation may be the accuracy of the temperature controllers used in the setup. Indeed, those temperature controllers use the temperature measured on a thermistor and a feedback loop to fix the target temperature. However, this feedback loop produces fluctuations of the temperature within a small range (the 0.1 °C accuracy specified by the manufacturer). It is thus possible that the frequency deviation we observed was linked to those temperature fluctuations.

We thus decided to stop the thermal control while keeping each of the lasers on separated heat sinks as shown in Figure 3-13-a. In this so-called configuration B, the Peltier elements have been removed and the glass chips lie on two distinct heat sinks which enables a homogeneous temperature on each chip and provides some thermal inertia. However, since we removed the controllers, the laser chips are both at room temperature. Thus, to generate a mm-wave carrier we used another couple of lasers which have been designed and fabricated to emit different wavelengths at ambient temperature. This has been done by adjusting the waveguide aperture width w of each laser as presented in the beginning of this chapter. Laser 1 has a w= 6.1 µm and emits 3.2 dBm of optical power at 1533.01 nm. Laser 2 has a w= 7.8 µm and emits at 1533.48 nm with an optical power equal to 3dBm. Figure 3-14 presents the electrical spectrum generated by optically mixing these two single mode lasers. A carrier at 60.3 GHz having its electrical power equal to -36 dBm has been generated. Its linewidth at -40 dB is measured to be 60 kHz. Assuming a Lorentzian profile, the linewidth of the generated signal is equal to 600 Hz for a measurement duration equal to 50ms.

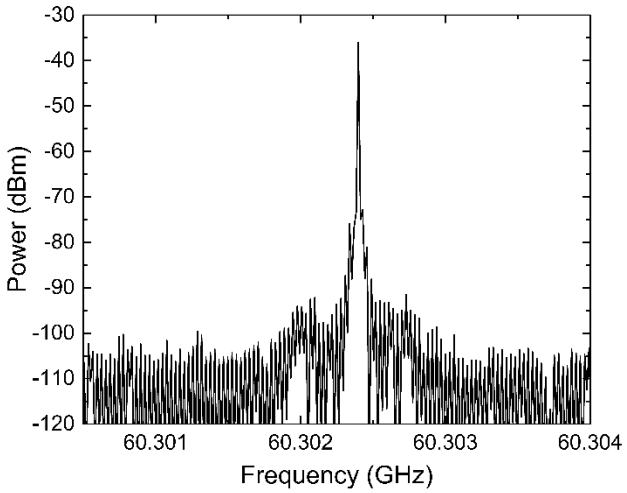

Figure 3-14 Electrical spectrum of the generated signal sweep time = 50 ms and resolution bandwidth = 3 kHz.

Again, the max-hold function on the ESA has been used to measure the frequency deviation of the generated signal for a 7 s duration as shown in Figure 3-15. A deviation reduced to 10 MHz/7 s has been measured.

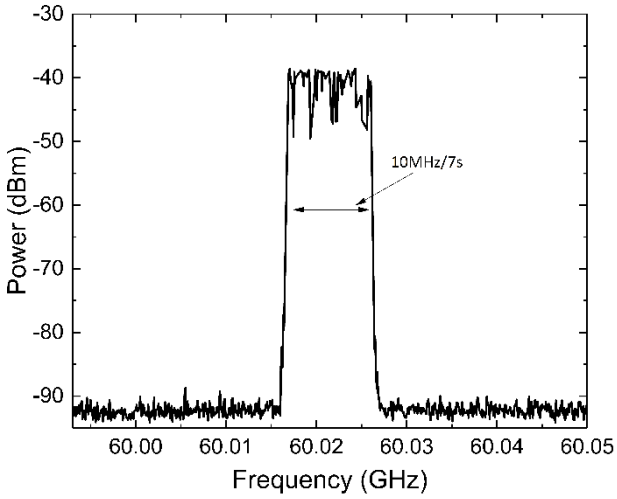

Figure 3-15. Measured frequency deviation for configuration B.

The deviation is improved almost 4-fold compared to configuration A. This improvement confirms the hypothesis that the 36 MHz/7 s deviation measured using configuration A is mainly caused by the thermal controllers' noise. However, the measured 10 MHz/7 s deviation corresponds to ±83 ppm, which is still higher than the IEEE standard [13]. This deviation corresponds to a relative temperature variation equal to 6.7 x 10^{-4} °C between the two lasers. As the two lasers are not close to each other in

this configuration, a very low thermal perturbation across the room can slightly change the temperature difference between the laser chips and thus produce a frequency deviation.

3.4.3 Configuration C: two lasers thermally coupled

After proving that the active thermal control degrades the stability of the generated signal, we wanted to further enhance the signal stability by thermally coupling the two lasers. The reasoning behind this was that we wanted to minimize the effects of spatial thermal variations by setting the two lasers chips at a common temperature. For that, we decided to implement configuration C, where the two lasers used in configuration B, are installed close to each other on the same heat sink to be thermally coupled, thus decreasing the magnitude of differential temperature variations between the two chips.

The deviation measurement has been performed for the same 7s duration. A deviation equal to 2 MHz/7 s has been obtained. This deviation value has been reduced 5-fold compared to the deviation measured in configuration B. It corresponds to ±16.5 ppm and finally respect the IEEE requirements [13]. To our knowledge, this is the first time that, using free running lasers, a mm-wave signal is generated with a stability that respects the communication standards. For comparison, the smallest deviation values obtained without stabilization are 200 MHz/20 s using comb laser sources [66], 3 MHz/320 ms [67] and 28 MHz/30 s [68] for dual mode semiconductor lasers.

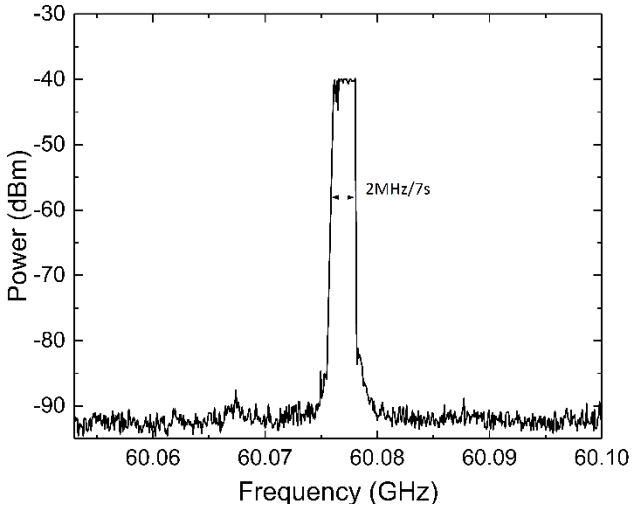

Figure 3-16. Measured frequency deviation for configuration C at 60 GHz.

As our carrier generation technique is based on heterodyning, the performances and spectral properties should not depend on the generated frequency and should be identical even for frequencies up to THz. In order to prove this assumption, two more deviation measurements have been performed with different generated frequencies. In the first one, we used the two lasers having that same

technological parameters. As they are similar, a beating frequency of only 2.1 GHz has been generated. Note that the two lasers used for the 2.1 GHz carrier generation are not the same that have been used in configuration A where 1 GHz has been generated. In the second measurement, two lasers having their waveguide aperture widths equal to 3.5µm and 4µm respectively were used to generate a signal at 36.9 GHz in order to use the same experimental setup used for [0 GHz – 40 GHz] measurement. Figure 3-17-a and Figure 3-17-b depict the respectively measured deviations. We observe that the deviations values at 2.1 GHz and 36.9 GHz are 2 MHz/7 s and 2.3 MHz/7 s respectively. These two values are quite similar and are also similar to the deviation measured at 60 GHz. These measurements indicate that the deviation is not linked to the generated frequency.

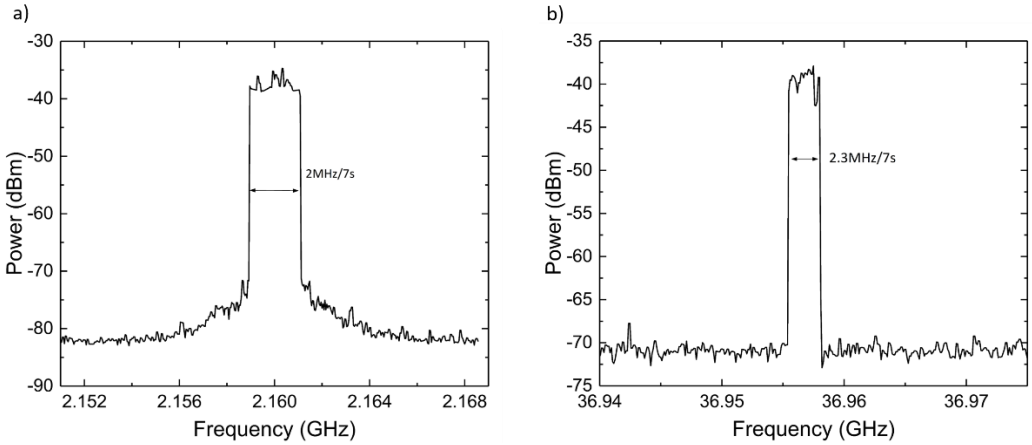

Figure 3-17 Measured frequency deviation for generated signal at a) 2.1 GHz and b) 36.9 GHz.

As the residual frequency deviation may be linked to thermal fluctuations, we investigated the dependency of the generated carrier frequency with temperature for two thermally coupled lasers. Using configuration C and activating the temperature controller, the temperature of the heat sink has been varied between 10 °C and 41 °C. The results are shown in Figure 3-18. For a variation of 31 °C, a variation of the beating frequency around 340 MHz has been measured. A linear fitting of the data gives an average variation of ≈11 MHz/°C. In section 3.3.1, the frequency variation of a single laser has been measured to be 1.49 GHz/°C. Thus, the thermal sensitivity is 100 smaller for thermally coupled lasers but is not zero as one could expect. We expect this sensitivity of the generated frequency to the temperature of the metallic base plate to decrease if the lasers are closer to each other. If the measured deviation of 2 MHz/7 s originates from the thermal sensitivity of the device (10.9 MHz/°C) the observed deviation would correspond to a temperature change equal to 0.18 °C for the whole structure. A room temperature variation of this magnitude is plausible for a duration of 7 s, so the cause for the observed deviation may be temperature variations.

Since closer lasers may have closer temperature variations, the deviation may be further decreased by using co-integrated designs. This is the object of chapter 4.

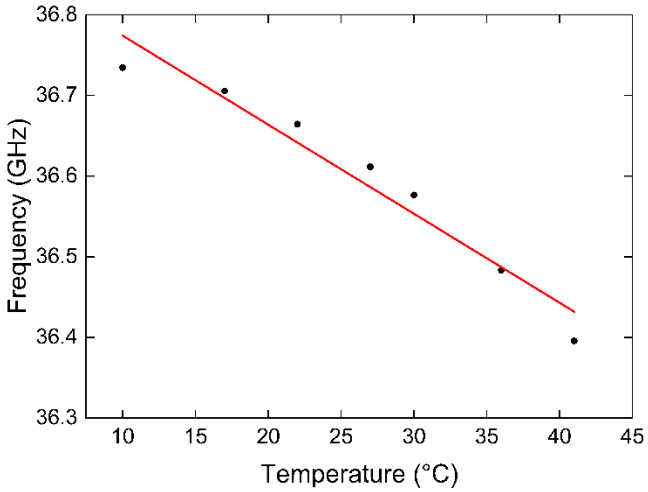

Figure 3-18. Variation of the measured generated frequency for different temperature values.

3.5 System evaluation

To evaluate the suitability of the generated carrier for communication applications, we proceeded with data transmission measurements. The setup used for this measurement is presented in Figure 3-19, where in addition to the setup used for mm-wave generation (Figure 3-7), we added some components illustrated in red.

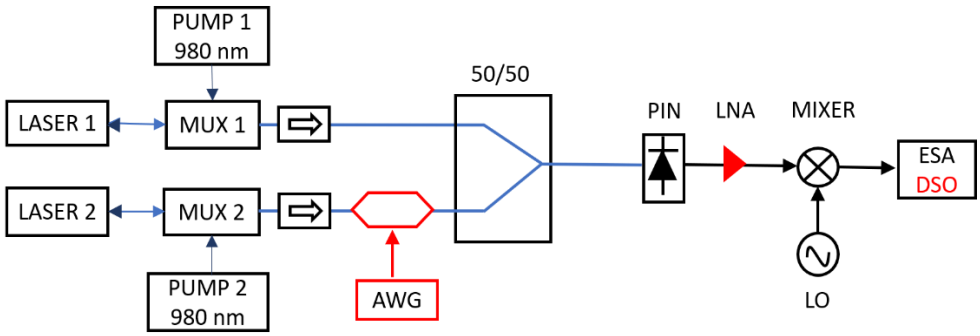

Figure 3-19 Experimental setup for data transmission measurements.

A Mack-Zehnder modulator (MZM) is used to modulate the intensity of the light at the output of one of the two lasers. A 35 dB gain low noise amplifier (LNA) having 55 GHz - 65 GHz bandwidth is added before the mixer to compensate for the losses generated by the mixer and the MZM. The data are electrically applied to the MZM using a Tektronix 12GS/s 7122B Arbitrary Waveform Generator (AWG) that generates BPSK, QPSK or 16QAM signals modulating a subcarrier; The signal and data

are captured and sampled using an Agilent 54855A high speed digital sampling oscilloscope (DSO) having 6 GHz bandwidth. Error vector magnitude (EVM) values are then measured online using a vector signal analyzer installed on the DSO. This same setup has been used for the three configurations A, B and C.

3.5.1 Configuration A

Figure 3-20 shows the different obtained EVM and back-to-back EVM values for different data rates using BPSK and QPSK formats. For both formats, the data transmission degrades quickly when increasing the data rates and when the bandwidth exceeds 500 MHz. However, the measured EVM at 400 Mbps using BPSK format already meets the ECMA [12] standards for the modes A0 and A10.

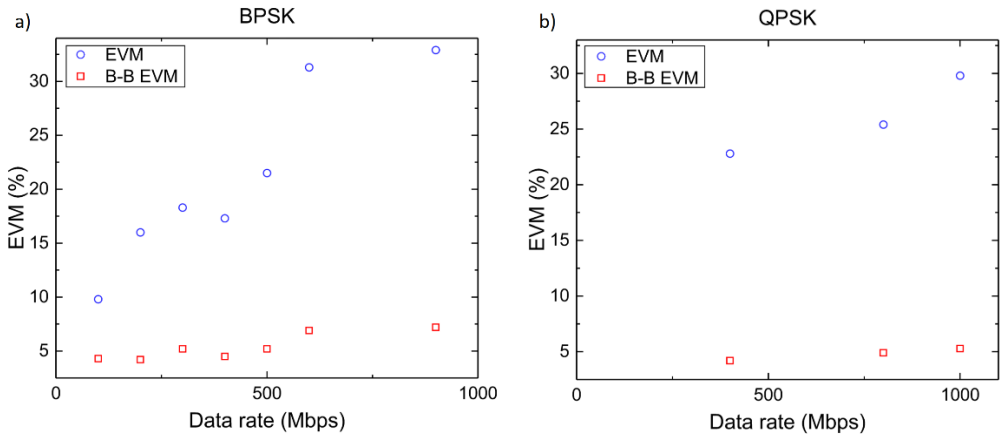

Figure 3-20 Measured EVM (blue empty circles) and B-B EVM (red empty squares) at different data rates for BPSK and QPSK formats.

3.5.2 Configuration B

To study the improvement for communication applications induced by the suppression of the thermal control in configuration B, data transmission measurements have been performed using the 60.3 GHz generated carrier with a 1.5GHz subcarrier. Figure 3-21 shows the different values of EVM and B-B EVM for BPSK, QPSK and 16QAM modulations formats, in addition to the constellations corresponding to the lower and higher data rates for each format.

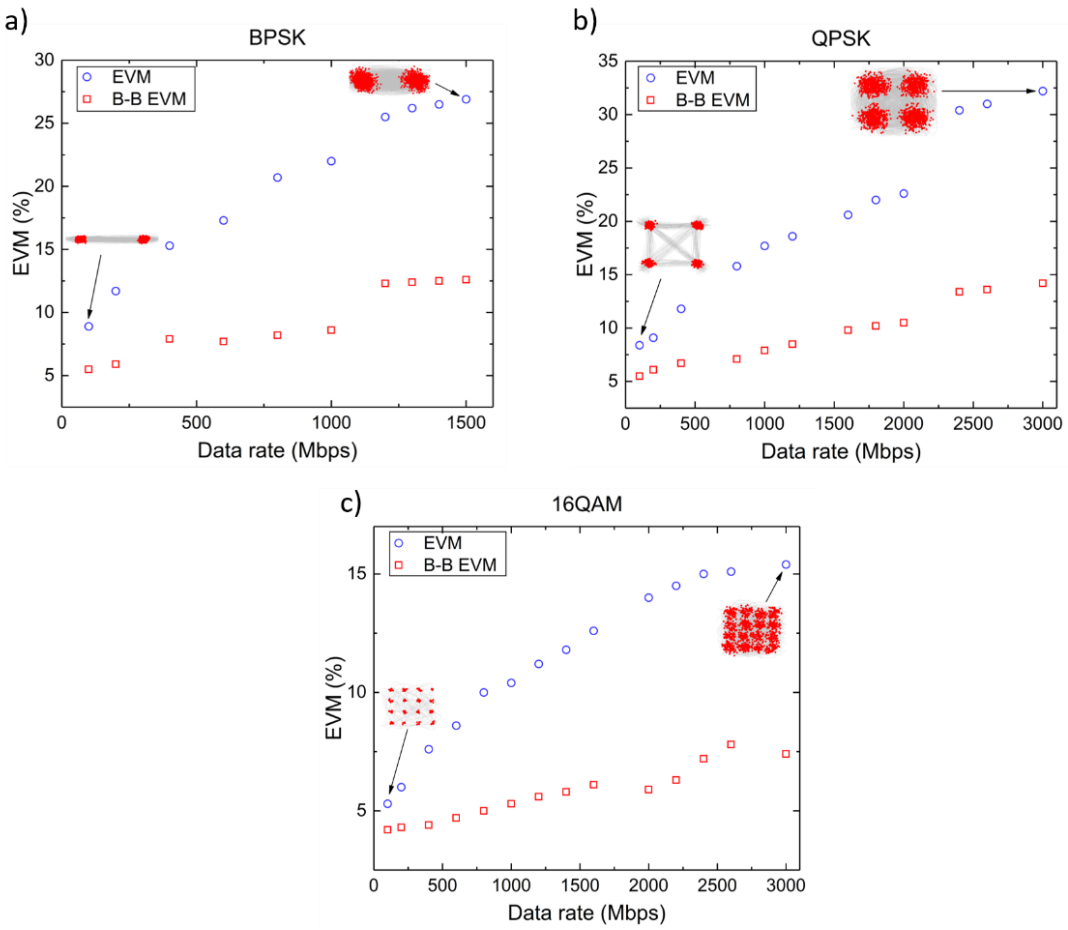

Figure 3-21 Transmitted and B-B EVM for a) BPSK, b) QPSK and c) 16QAM modulation formats for thermally independent lasers and without temperature controllers (configuration B).

By comparison with the data transmission results from configuration A, an important improvement can be observed. For BPSK and QPSK, better values of EVM have been measured for the same data rates. Moreover, we were able to transmit and demodulate data using 16QAM format up to 2 Gbps which was not possible using configuration A. The measured EVM values fulfill the requirements for the ECMA standards [12] [A0 (397 Mbps - BPSK), A1 (794 Mbps - BPSK), A3 (1588 Mbps - QPSK) and A10 (1588 Mbps - QPSK) modes]. This improvement clearly proves the improvement of the data transmission performances by increasing the frequency stability in heterodyned systems.

3.5.3 Configuration C

The reduction in the measured deviation value with configuration C has been once again characterized by performing data transmission measurement. Figure 3-22 shows the different values of EVM and B-B EVM for BPSK, QPSK and 16QAM modulations formats, in addition to the constellations corresponding to the lower and higher data rates for each format. By comparing the

measured EVM between the two configurations B and C, we can measure the impact of the deviation improvement. As the signals in both configurations have been studied at the same frequency and with the same optical and electrical powers, the differences in the measured values of EVM can only be attributed to the different frequency deviations. Improvements in the measured EVM values ranging between 2 points and 7.5 points, 2 points and 6 points and 1.7 points and 3.7 points for BPSK, QPSK, and 16QAM modulations formats respectively have been observed. These results show that passive thermal coupling allows a better-quality transmission and confirm the higher relative stability of the laser already shown by smaller frequency deviation value.

As the measured EVM values have been reduced, they still fulfill the requirements for the ECMA standards [12]. The EVM improvement can be used to reduce the transmission constraints, on the signal to noise ratio for example. Note that using the generated signal, we could perform transmissions with better-quality, but we were still limited by the B-B EVM mainly induced by the sampling precision of both the arbitrary waveform generator and the oscilloscope used in our system.

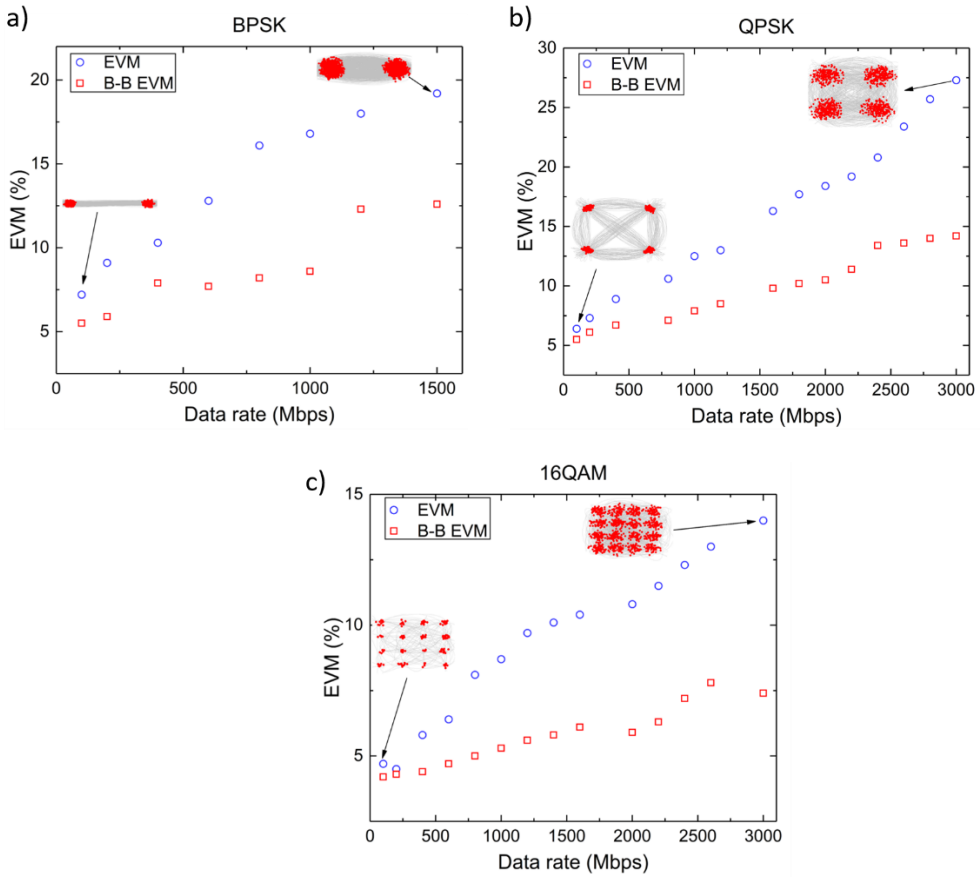

Figure 3-22 Measured values for EVM (blue empty circles) and B-B EVM (red empty squares) for a) BPSK, b) QPSK and c) 16QAM modulation formats with configuration C.

3.6 Conclusion

In this chapter, we studied the generation of mm-wave carriers using free-running DFB lasers on glass. At first, the results of simulations predicted the possible frequencies that can be generated using such lasers, by adjusting with precision their aperture widths and the ion exchange durations. Then, the tolerance of the fabrication process has been simulated. The experimental generated frequencies by heterodyning two DFB lasers on glass are in excellent agreement with the simulations.

Then, the first measurements for mm-wave carrier generation using free-running DFB lasers on glass have been presented. The first experimentally generated signals have very narrow linewidth lower than 10 kHz. We presented three configurations to demonstrate the negative influence of the thermal control on the generated radio carrier and the importance of the thermal coupling between the two lasers. The generated signal has been improved to fulfill the IEEE standards for frequency deviation. Figure 3-23 summarizes the reduction of the frequency deviation from 36 MHz/7 s in configuration A to 2 MHz/7 s in configuration C.

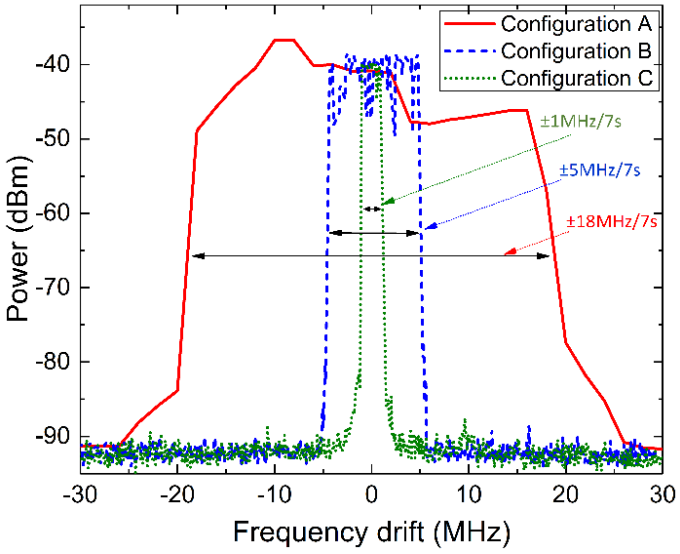

Figure 3-23 Comparison for the deviation obtained with the three configurations.

Table 3-4 summarizes the different results obtained in this chapter for the generated mm-wave carrier and the data transmission experiments. For each modulation format, the first given value is the data rate (Mbps) and the second value is the measured EVM (%).

Configuration	Frequency	Data transmission (data rate / EVM)		
		BPSK	QPSK	16QAM
A	54 GHz	900 Mbps 32.9 %	1000 Mbps 29.8 %	-
B	60.3 GHz	1200 Mbps 25.5 %	2600 Mbps 31.2 %	2000 Mbps 14 %
C		1200 Mbps 18 %	2600 Mbps 22.4 %	3000 Mbps 14 %

Table 3-4. Summary of the obtained results for data transmission.

We think that the residual deviation of less than 2 MHz/7s obtained with configuration C is not inherent to our lasers and may be explained by different phenomena that will be investigated in chapter 4.

4 Co-integrated designs

4.1 Introduction

In chapter 3, we have studied the performances of two glass DFB lasers used for mm-wave carrier generation. It has been shown that the frequency deviation observed on those devices had strong connections to temperature variations and depended on how the two laser chips were thermally coupled. We have shown that the frequency deviation of 2 MHz/7 s measured in configuration C where the two laser chips are coupled by a metallic plate may result from the temperature fluctuations of the plate. We expect that this effect should be smaller on lasers co-integrated on the same wafer since the distance between the lasers is then smaller.

Moreover, the compactness of photonic circuits is an important criterion in order to be used in RoF systems. A device where both lasers are co-integrated would thus be more stable on top of having a smaller footprint. Up to now, the fabrication and characterization for separate DFB lasers on glass have been presented. Each of the lasers was 3.6 cm long with an aperture width ranging from 3.5 µm to 10 µm.

In this chapter, we present three co-integrated designs for glass DFB lasers: two DFB lasers emitting different wavelengths integrated on the same chip, a Y-junction DFB laser and a dual-mode laser. Using each of these designs, RF carriers are generated, characterized and evaluated in communication systems.

At the end of the chapter, prospects of this work are given.

4.2 Co-integrated lasers

The first proposed co-integrated design, presented in Figure 4-1, is the co-integration of two DFB lasers on glass having different waveguide aperture widths. As described in the previous chapter, to obtain different emission wavelengths, fabrication parameters (w, t and Λ) can be adjusted differently for each laser. We have chosen to vary only the parameter w since it is the easiest choice:

- The variation of the ion exchange duration t is difficult on the same chip.
- The variation of the grating step Λ requires two Bragg grating implemented on the same chip. It is difficult to vary Λ precisely, especially with the precision of our current setup.
- The variation of w only requires an adequately designed mask for photolithography.

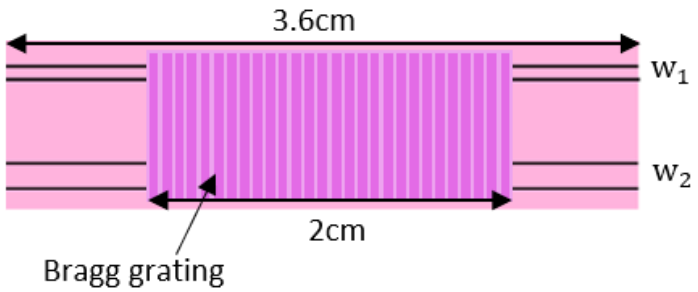

Figure 4-1 Co-integrated lasers design.

The spacing between the core of the two waveguides was a multiple of 127 µm. This is the smallest spacing that can be fixed when using fiber arrays to connect our chip. Several apertures widths have been set on the mask as presented in 3.2.2.2. We aimed at obtaining frequencies in all the mm-wave range. The length of the waveguide and the grating have been fixed as previously to 3.6 cm and 2 cm.

4.2.1 Frequency generation

Using this design, carriers at different frequencies ranging from 5 GHz to 164 GHz using three different detection setups have been generated. For frequency between 5 GHz to 67 GHz, the setups use direct analysis or down conversion using an electrical mixer as already presented in Figure 3-7. For higher frequencies, the setup depicted in Figure 4-2 has been used. In such detection scheme, the coupled output of the two DFB lasers illuminated an InGaAs photoconductive switch. The used photoswitch are also under test, they have been designed in 2012 in UCL London [69]. Their characterization is mainly the topic of another thesis currently under preparation in the IMEP-LAHC laboratory by Róbert Horváth [70]. Two electrical coplanar RF probes were used to connect the photoswitch to an RF generator and the measurement equipment. The photoswitch was biased using an RF signal generator using a 67 GHz probe (i67). The output was connected using a 110GHz probe (model i110, Cascade Microtech) followed by a harmonic mixer operating in the 60GHz – 90GHz range for measuring higher output frequencies. The output signal at the intermediate frequency was analyzed with an ESA. This setup used a prototype of an electro optic switch that allows the mixing of the optical signal from our laser with the electrical signal from the RF generator. The low frequency mixed signal at the output can help to investigate both optical and electrical inputs at a frequency too high to be analyzed.

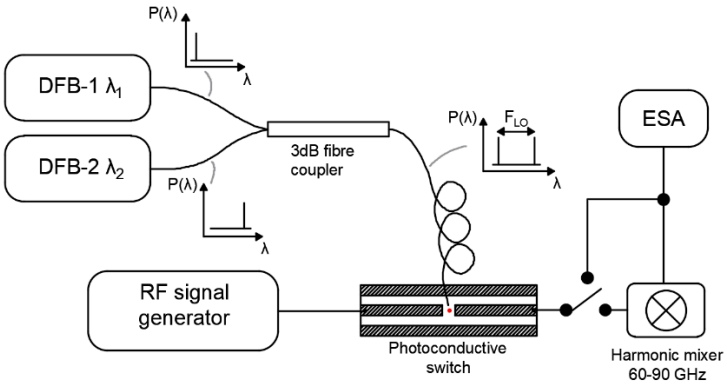

Figure 4-2 Setup for mm-wave generation using co-integrated lasers for frequencies between 65 GHz and 164 GHz.

4.2.2 Linewidth

Figure 4-3 depicts electrical spectra for three generated signals using co-integrated lasers, to present the frequency capability of the co-integration. The 5 GHz signal (Figure 4-3-a), has been generated using two lasers having waveguide aperture widths equal to 7 µm and 7.2 µm respectively. The total optical power before the PD was -5 dBm. Figure 4-3-b shows the generated signal at 52 GHz using two

lasers with waveguide aperture widths equal to 6.7 µm and 7.8 µm respectively. The total optical power before the PD was -2.3 dBm. In this case, a lower electrical power has been measured compared to the signal generated at 5 GHz, mainly because of the mixer and connection losses. The highest frequency that is possible to measure with the equipment available in the laboratory is 164 GHz (Figure 4-3-c). Two lasers having aperture widths equal to 3.5 µm and 9.4 µm emitting powers as high as 15dBm have been used for this measurement to illuminate the InGaAs photoswitch. The switch has low conversion efficiency as it is also under testing, but this measurement represents the first experimental THz generation demonstration using co-integrated DFB lasers on glass.

For both 5 GHz and 52 GHz signals, the linewidth at -40 dB is equal to 40 kHz. Assuming a Lorentzian profile, the linewidth at -3 dB is equal to 400 Hz for a measurement duration equal to 50ms. The spectrum at 163.8 GHz was not acquired with a span and an RBW that allow the characterization of its linewidth.

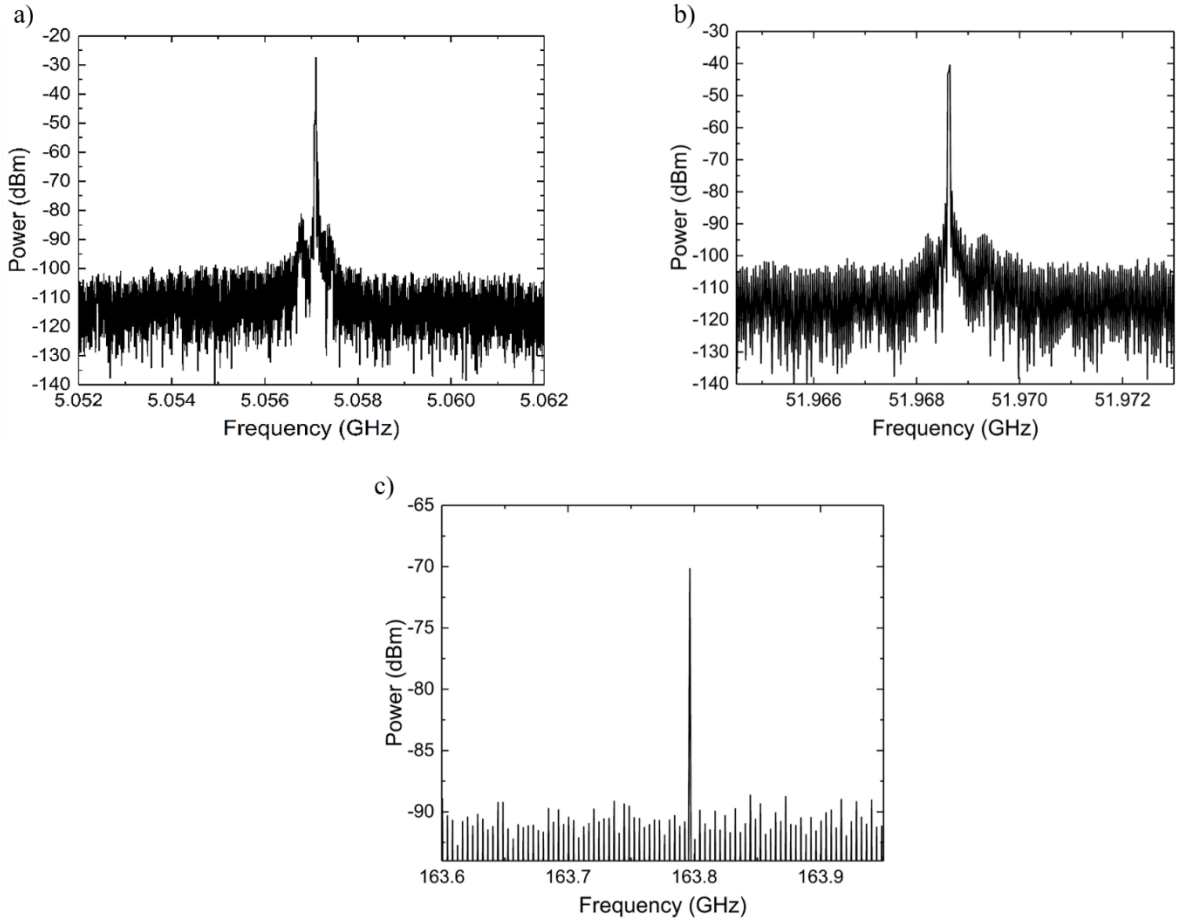

Figure 4-3 Spectra generated with co-integrated lasers at a) 5 GHz, 52 GHz and c) 163.8 GHz.

These results show that the linewidth of the generated RF carrier is independent from the generated frequency. In this work, we only present the characterizations of the generated signal at 52 GHz, as we have already proved that all the RF carriers have the same performances independently from the generated frequency.

4.2.3 Stability

Figure 4-4 shows a spectrum of the 52 GHz carrier recorded with the max-hold function of the ESA for a 14s duration. A total frequency deviation of 1.6 MHz/14 s has been measured. This deviation is slightly lower than the one obtained with independent thermally coupled laser chips (2 MHz/7 s). This result is coherent with our previous analysis on independent laser chips that the stability of the generated signal depends on the thermal coupling between the two lasers. Note that the two lasers used to generate this signal were separated by a distance of 254 µm.

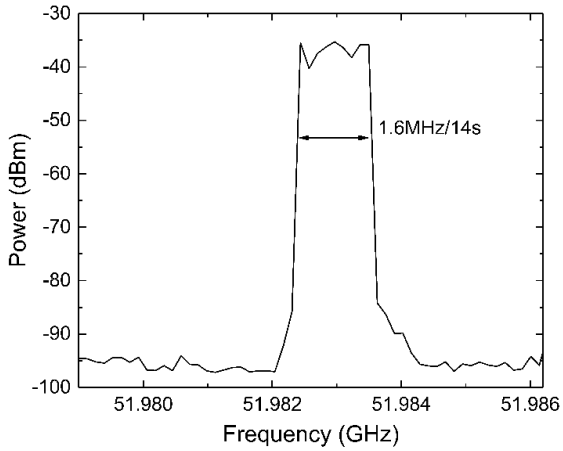

Figure 4-4 Measured deviation for the generated 52GHz signal using co-integrated lasers.

4.2.4 System evaluation

Data transmission experiments have been performed using the previously described setup shown in Figure 3-7. Three different modulation formats have been used: BPSK, QPSK and 16QAM. The measured EVM and back-to-back EVM for the three modulation formats are presented in Figure 4-5 as well as the constellations of the lowest and highest data rates for each format.

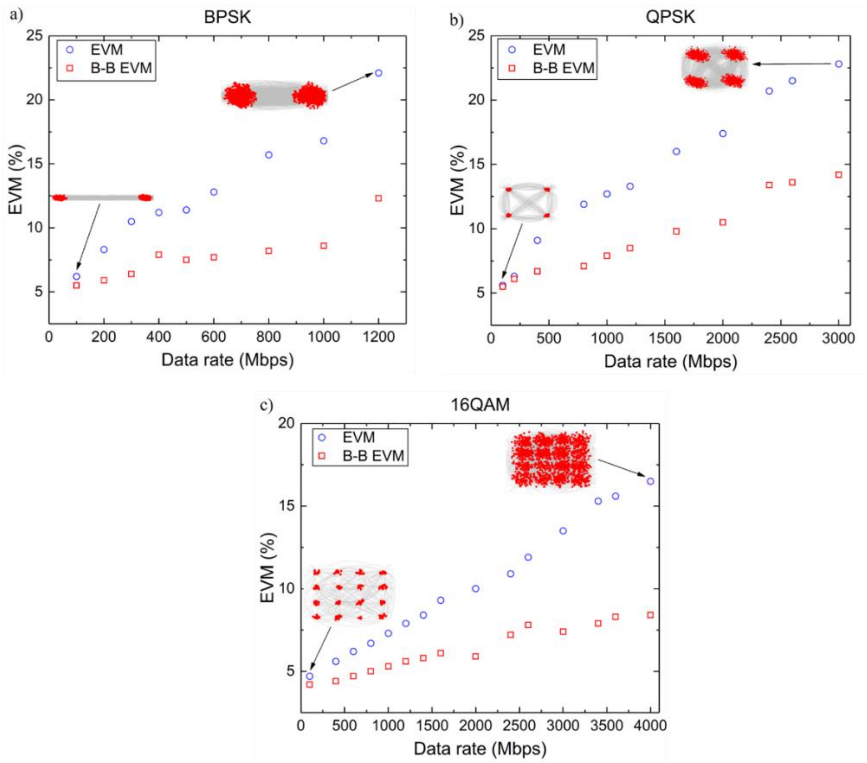

Figure 4-5 Measured EVM and B-B EVM and constellations for the a) BPSK, b) QPSK and c) 16QAM modulation formats using co-integrated lasers at 52 GHz.

By comparing the EVM values obtained here with the ones obtained in configuration C in section 3.5.3, we can see in Table 4-1 a slight improvement in the data transmission quality for QPSK and 16QAM formats. This is coherent with the slight improvement measured for the generated signal stability. However, it is good to note that the generated signal is at 52 GHz while the LNA bandwidth that has been used is between 55 GHz and 65 GHz, some degradation of the signal has been added. And thus, the fact that quite similar EVM values have been measured for both configuration C and the co-integrated lasers potentially mean that the co-integrated lasers could perform better data transmissions at an adequat frequency with the used LNA.

Design	Frequency	Data transmission		
		BPSK	QPSK	16QAM
Config. C	60 GHz	1200 Mbps 18 %	2600 Mbps 22.4 %	3000 Mbps 14 %
Co-integrated lasers	52 GHz	1200 Mbps 22.1 %	2600 Mbps 21.5 %	3000 Mbps 13.5 %

Table 4-1 Data transmission performance comparison between configuration C and the co-integrated lasers.

4.3 Co-integrated lasers with a Y-junction

In the previous section, the impact of co-integrating the two lasers has been addressed. A slightly more stable signal and a better data transmission have been measured. In this section, a new design is presented. It can be described as a Y-junction DFB laser. The design of the device is shown in Figure 4-6. The Y-junction has the role of a 50/50 optical coupler which separates the pump to feed the two laser cavities and also combines the backward signals from the two lasers. This design thus allows the use of only one pump diode for both lasers and avoid the use of an external fiber coupler.

The aperture width of the Y-junction and one of the two exit waveguides has been fixed to be w_1. The aperture width of the second exit waveguide is fixed to be w_2, 100 µm after the end of the Y-junction. The transition w_1 - w_2 is achieved via a linear taper. When implementing the Bragg grating on the waveguide, we were careful not to have the Bragg grating on the taper nor on the Y-junction. There is thus no optical coupling between the two DFB cavities of this device.

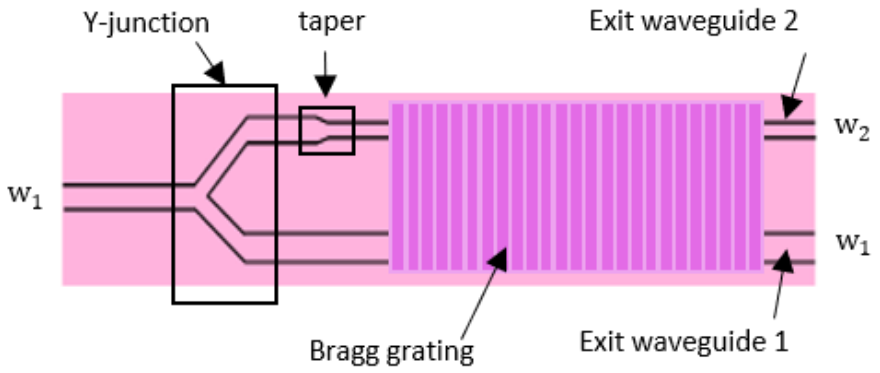

Figure 4-6 Co-integrated lasers with a Y-junction.

4.3.1 Frequency generation

Experimentally, carriers at two frequencies have been generated with this design. Using 9.3 µm and 9.4 µm waveguide aperture widths, a signal at 5.3 GHz has been generated. And using 6 µm and 6.7 µm waveguide aperture widths, a carrier at 36.5 GHz has been generated. Devices with smaller widths have been fabricated but they didn't function due to the insufficient gain.

Using the Y-junction design, the carrier generation setup has been simplified as seen in Figure 4-7. The two lasers are pumped using the same 980 nm LD and the backward emitted signal is directly collected from the input facet. When used for data transmission, a MZM is inserted directly at the 1550 nm output port of the multiplexer, thus the two lasers outputs are modulated. This configuration makes the signal sensitive to chromatic dispersion as the two signals containing data are superimposed.

Even if this setup is enough to characterize the impact of the optical source on the data transmission, it can be further improved by inserting a wavelength demultiplexer to modulate only one lasing signal by using the two co-propagating output

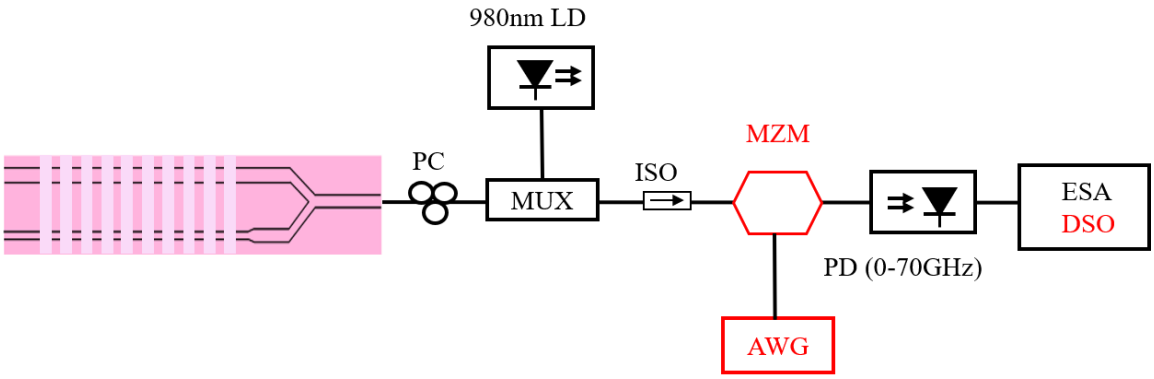

Figure 4-7 Experimental setup for carrier generation and data transmission (in red) using co-integrated lasers with Y-junction.

4.3.2 Linewidth

Figure 4-8 shows an electrical spectrum acquired for the 5.3 GHz generated carrier using our Y-junction design emitting two wavelengths around 1534.5 nm having a total optical power equal to -1 dBm. The two side peaks at less than 1 MHz from the carrier correspond to the laser intensity noise at the relaxation frequency. The linewidth of the signal is measured to be 1.8 kHz for a measurement duration equal to 50ms assuming a Lorentzian shape. It is important to point out that all the measurements for the Y-junction design have been performed without the use of any optical and/or electrical amplifiers.

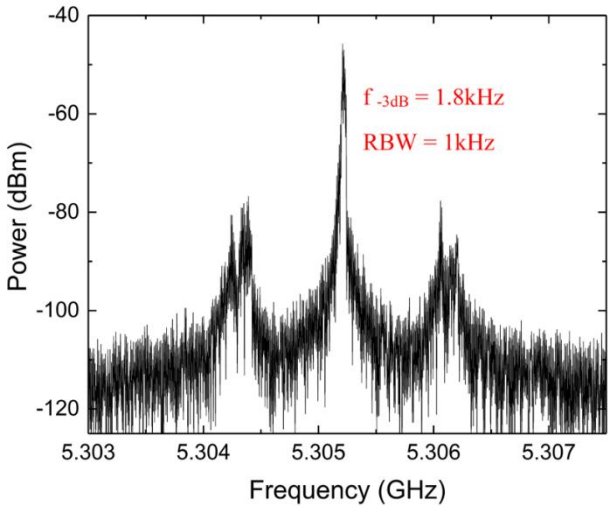

Figure 4-8 Electrical spectrum of the carrier generated using Y-junction lasers with w_1 = 9.4 µm and w_2 = 9.3 µm.

4.3.3 Frequency deviation

In Figure 4-9, the measured frequency deviations for short-term durations at 5.3 GHz (30 s) and at 36.5 GHz (14 s) and long-term duration (90 min) at 5.3 GHz are presented. For a duration of 30 s, a frequency deviation equal to 1.8 MHz has been measured for the 5.3 GHz carrier (Figure 4-9-a). For 14 s, the measured deviation for the 36.5 GHz carrier is 1.4 MHz (Figure 4-9-b). By comparing these two values, we can observe that comparable deviations are measured for two different durations (14 s and 30 s). The measured deviation values are slightly better than the ones measured previously with other designs and they also fulfill the IEEE standards [13].

The short-term duration deviation has been accompanied by a long-term duration measurement of the 5.3 GHz carrier. For 90 minutes, the frequency value has been recorded every 5 minutes. The recorded values depicted on Figure 4-9-c show that the long-term frequency deviation is less than

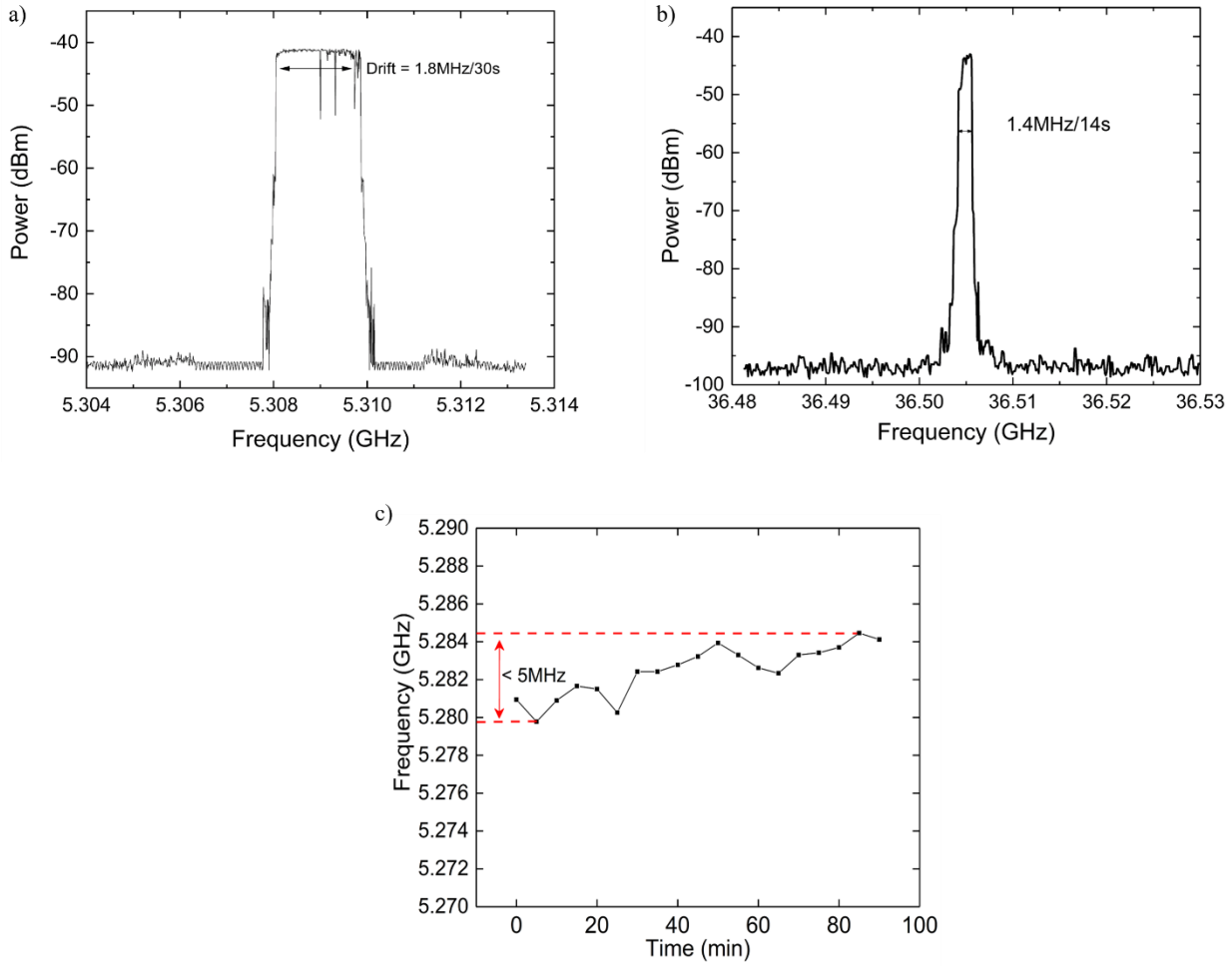

Figure 4-9 Measured carrier frequency deviation using Y-junction designs for a) 30 s at 5.3 GHz, b) 14 s at 36.5 GHz and c) 90 min at 5.3 GHz.

5 MHz over 90 min.

These frequency deviation measurements have been performed without any thermal control. It is interesting to see that short-term and long-term deviation values are close, which demonstrates that our device can work for long periods of time with no degradations of its performances.

4.3.4 Source of the frequency deviation using the Y-junction design

Using the Y-junction design, the frequency deviation value decreased slightly. But the measured deviations are still between 1 MHz and 2 MHz. We investigated what can be the source of the residual deviation. We have identified three different phenomena as the main candidates to explain the deviation:

a- Fluctuations of the differential temperature between the lasers.
b- Pump power fluctuations
c- Variation of opto-mechanical properties due to vibrations.

We investigated each possible source apart:

a- Thermal effect

The thermal effect on the generated frequency has been studied for the 5.3GHz carrier. The temperature of the heat sink, where the Y-junction chip has been installed, has been varied between 15°C and 63°C. As shown on Figure 4-10, an average variation equal to 0.7 MHz/°C has been measured. This thermal sensitivity is much lower than the measured value using two separate lasers on the same heat sink (10 MHz/°C). Using this design, the generated frequency sensitivity to thermal effects has been reduced, which means it is more immune to environmental temperature variations.

Furthermore, considering the thermal effect is the deviation source, the measured 1.8 MHz / 30s deviation would correspond to a room temperature variation of 2.5 °C in 30 s. This variation seems too high to be realistic. Thus, another phenomenon has to be the source of the frequency deviation.

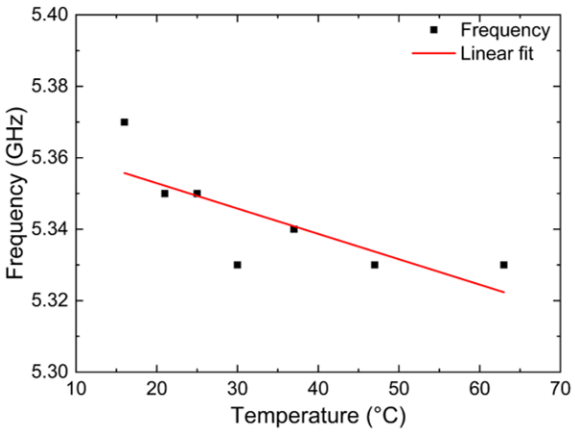

Figure 4-10 Thermal effect on the generated carrier using the Y-junction design at 5.3GHz.

b- Pump laser diode pump fluctuation

To investigate if the residual deviation is linked to some pump power fluctuations, we intentionally modulated the pump power at different frequencies with a modulation amplitude equal to ±200 mA corresponding to a variation of the injected power of ±70 mW. The used modulation frequencies and their corresponding deviations integrated over 30 s are summarized in Table 4-2. It can be seen that no significant variation of the deviation is observed for different modulation frequencies. Moreover, the deviation values are very close to those measured with no pump power modulation even though the modulation amplitude is very high when compared to the noise amplitude we expect from the pump diode. Pump power variations may then not be the source of the measured deviation in this Y-junction design.

Modulation frequency	Deviation (MHz)
No modulation	1.8
1Hz	1.8
10Hz	2.1
1kHz	1.7
100kHz	2

Table 4-2 Measurement of the frequency deviation of the 5.3 GHz carrier for various pump modulation frequencies.

c- Variation of opto-mechanical properties due to vibrations.

A third possible source of the frequency deviation is the vibrations. Given that the chip is not packaged and that we have not connectorized the input fiber to the chip, we could observe some vibrations of the input fiber. On single mode waveguides, these vibrations produce small coupling

variations, but their effect is very small. However, at the pump wavelength, the Y-junction used in our device is multimode. Vibrations of the input fiber can then vary the ratio of the pump power injected in each of the DFB cavities. We believe that this phenomenon leads to opposite variations of the frequency emitted by the two lasers which could cause the observed frequency deviation. In section 2.5.2.2, we have measured frequency sensitivity linked to the variation of the pump power in the order of 9 MHz/mW. A differential variation of less than one milliwatt between the two lasers could thus lead to the observed frequency deviation. Note that this effect could not be measured when modulating the pump power in the previous paragraph, because the modulation had the same effect on both branches.

In order to verify this hypothesis, we have tried to use the Y-junction designs, which were single mode at the pump wavelength. However, these devices would not lase because the optical gain is lower with smaller aperture waveguides. Another possibility would be to connectorize the input fiber to the glass chip.

4.3.5 System evaluation

The generated carrier at 5.3GHz using the Y-junction design is evaluated via data transmission measurements. EVM and back-to-back EVM values have been measured (Figure 4-11) for the three used modulation formats BPSK, QPSK and 16QAM. EVM values are better using the Y-junction design than using the co-integrated lasers only and they are consequently compliant with the standards and give more margin for other parameters like SNR.

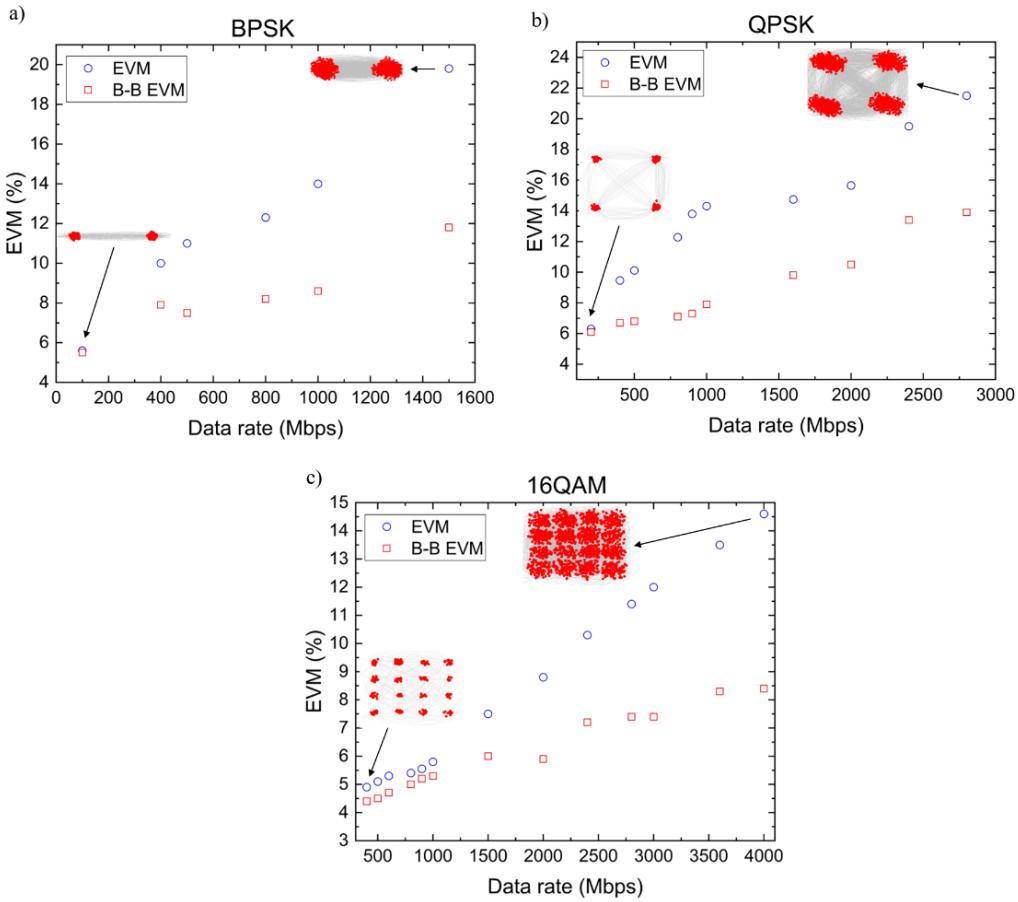

Figure 4-11 Measured EVM and B-B EVM and constellations for the a) BPSK, b) QPSK and c) 16QAM modulation formats using the 5.3GHz carrier generated by the Y-junction design.

4.4 Design and fabrication of a dual mode laser

A more advanced design has been also proposed during this work, the dual mode laser. It consists of having the two co-linear laser cavities on a single waveguide as depicted in Figure 4-12-a. Figure 4-12-b, Figure 4-12-c and Figure 4-12-d illustrate three possible different designs for dual mode laser. As it has been presented in chapter 3, three main technological parameters (w, t and Λ) can be adjusted to fabricate a laser emitting at a specific wavelength. The difference here is that we want to implement the two lasers on the same waveguide, which can induce some additional limitations.

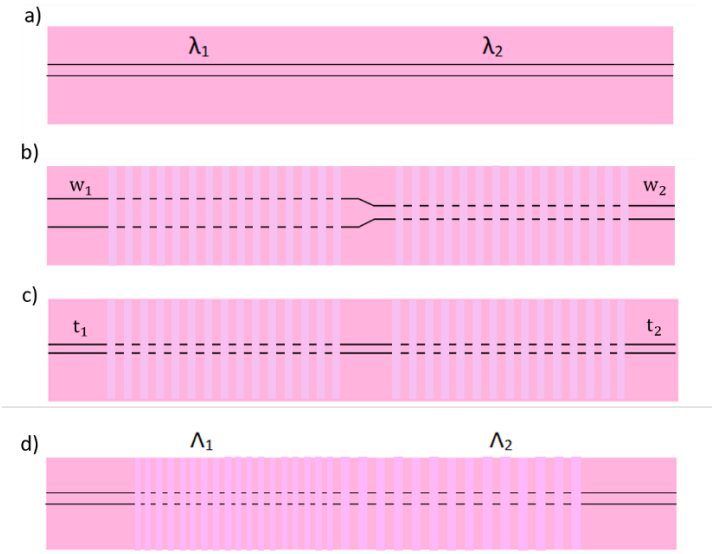

Figure 4-12 dual mode laser a) principle and design b) with different waveguide aperture widths, c) two ion exchange durations and d) two Bragg grating steps.

4.4.1 Design and fabrication of dual mode lasers

The design illustrated in Figure 4-12-b has been fabricated and characterized with different couples of (w_1, w_2). Only the waveguide having w_1 = 7 µm and w_2 = 7.1 µm separated by a 10 µm long taper has worked, generating an RF carrier at 6 GHz. The first experimental characterization of this 6.1 GHz carrier are presented in the following sections of this chapter.

With this design, two options have been proposed for the Bragg grating implementation:

- The grating is centered on the waveguide and thus, it is also on the top of the taper. There is in this case a single DFB laser cavity.
- The taper is masked during the grating implementation so that the grating is not etched on the taper. There are thus two laser cavities with separated gratings.

During this work, the two propositions have been fabricated. They both functioned with comparable results. We expect a more differentiated behavior between the two options as the aperture width difference is increased and the taper is longer. More work will then need to be done to study the effect of having the grating on the taper and the impact of separating the two gratings.

The second parameter that needs to be optimized is the taper design and dimensions to reduce the losses. Indeed, for these first tests, we used linear tapers, which is the simplest design. However, these tapers are not optimized for low losses, which may be the reason why the lasers having their widths differences

higher than 0.2 µm have not functioned. The other explanation is that each laser has a length of about 1cm, half of the length of our standard DFB lasers. This length may be too small to allow for an easy laser operation.

Figure 4-12-c illustrates a laser fabricated with two ion exchange durations in order to have on the same waveguide two distinct effective refractive index and thus two distinct emission wavelengths. Figure 4-13 depicts the two different techniques to realize the ion exchange with two different durations on the same waveguide. During this work, the study of the temperature homogeneity in different spots in the salt bath has been performed. A temperature difference of less than 10 °C between the bottom and the top of the salt bath has been measured. This difference is low and thus it allows us the realization of ion exchange supposing a quasi-homogeneous temperature for the whole glass sample.

Unfortunately, we have not been able to fabricate lasers using this technique. Indeed, during the ion-exchange process, the sample has been held vertically (see Figure 4-13a) and some air bubbles have been trapped on the glass surface during the descent of the wafer. This resulted in small zones where the ion-exchange did not take place, leading to non-continuous waveguides.

The second realization process proposition shown on Figure 4-13b, consists in tilting the sample with waveguide apertures facing top, so as to avoid the formation of air bubbles. We did not have time to test this modified process, but if it works, we expect to have less losses in the waveguide compared to the previous design (Figure 4-12-b).

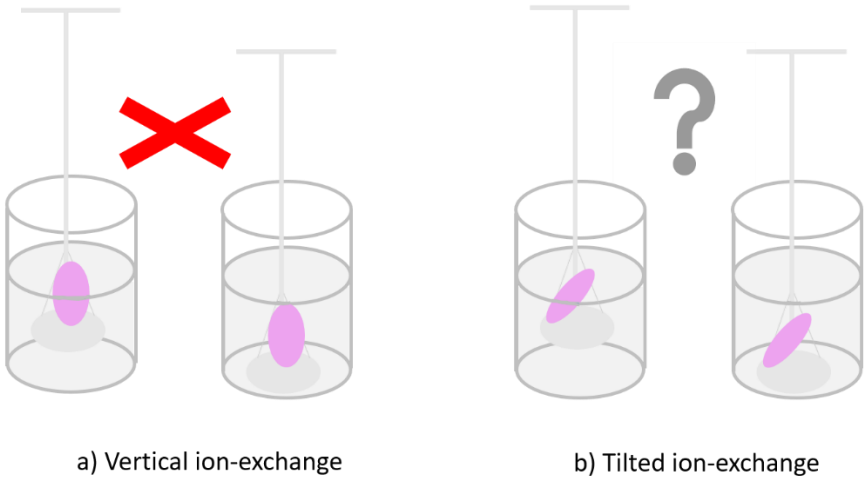

Figure 4-13 Ion-exchange realization process: a) the glass is immersed vertically into the salt bath, and b) the sample is tilted.

The third parameter that can be adjusted is the grating step. As already said in chapter 3, the fabrication tolerance of this parameter is ±0.5 nm ≈ 200 GHz. Thus, with our actual fabrication bench, this parameter can only be used for frequencies close to the THz band for applications where the frequency precision is not important.

4.4.2 RF generation and system evaluation

The device we characterize here is fabricated with 2 waveguide sections of different widths (w_1 = 7 µm and w_2 = 7.1 µm) separated by a 10 µm long taper. The laser output power and optical spectrum of the dual-mode laser has been measured as a function of the pump power. We observed that for low pump powers, only one wavelength was emitted. This corresponded to the emission of the laser located closer to the pump. In order to obtain two emission wavelengths, the pumping power needed to be set close to its maximum value of 560 mW. In this case, an average output power of 16 mW has been measured.

The setup depicted in Figure 4-14 has been used for the RF carrier generation. This setup is quite similar to the one used for Y-junction characterization. A variable optical attenuator (VOA) has been inserted before the photodiode to attenuate the output optical power of the laser to less than 7dBm which is the damage threshold of our photodiode.

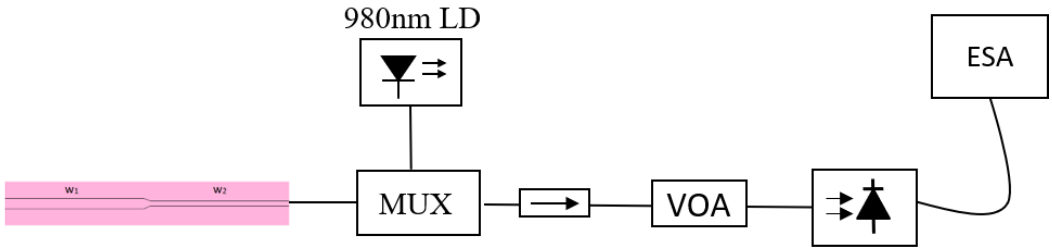

Figure 4-14. Setup for RF carrier generation.

Figure 4-15 depicts the generated RF carrier at 6.1 GHz. The linewidth at -40 dB was measured to be 60 kHz. Supposing a Lorentzian profile, the -3dB linewidth of the generated carrier is estimated to be equal to 600 Hz. Moreover, the measured SNR is as high as 60 dB.

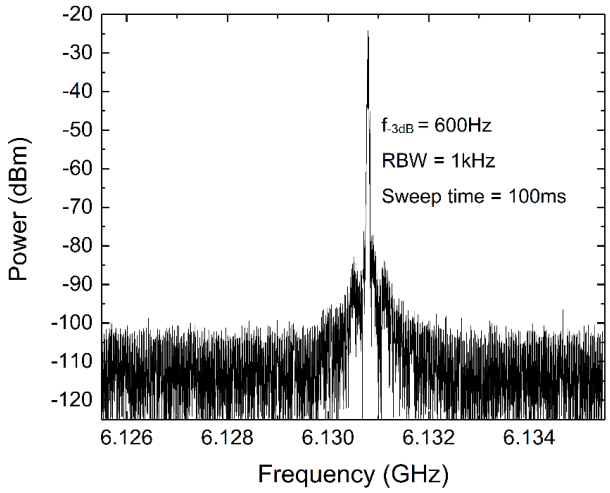

Figure 4-15. Spectrum of the generated carrier at 6 GHz using a glass dual mode laser.

The generated carrier has then been used for data transmission. A MZM has been inserted after the isolator to modulate the two lasers signals. We used the same data transmission setup that has been used for all the previous similar measurements. Figure 4-16 shows the different obtained EVM and back-to-back EVM for BPSK, QPSK, 16AM and even 64QAM. Data have been successfully transmitted and demodulated for data rate up to 1500 Mbps for BPSK, 2800 Mbps for QPSK, 4400 Mbps for 16QAM and 2000 Mbps for 64QAM modulation formats.

These measured EVM values are compliant with the requirements for the ECMA standards [A0 (397 Mbps - BPSK), A1 (794 Mbps - BPSK), A3 (1588 Mbps - QPSK) and A10 (1588 Mbps - QPSK) modes]. Note that for the 16QAM, the first mode from the standards is already at 4234 Mbps and the maximum allowed EVM is 11.1 %. The measured EVM in such configuration doesn't meet the requirement as the measured EVM is equal to 12.8 %. This result is still good as the main reason for not reaching such tight requirement is not due to the tested optical source but the back-to-back EVM that is already 9 %. This demonstrates that the generated carrier could potentially fulfill the standard if better equipment were used. The transmission integrity is the best obtained compared to all the other configurations and designs that we have proposed in this manuscript. It is also worth noting that this is the only device that allowed us to perform transmissions using the 64QAM modulation format, proving a very good carrier stability.

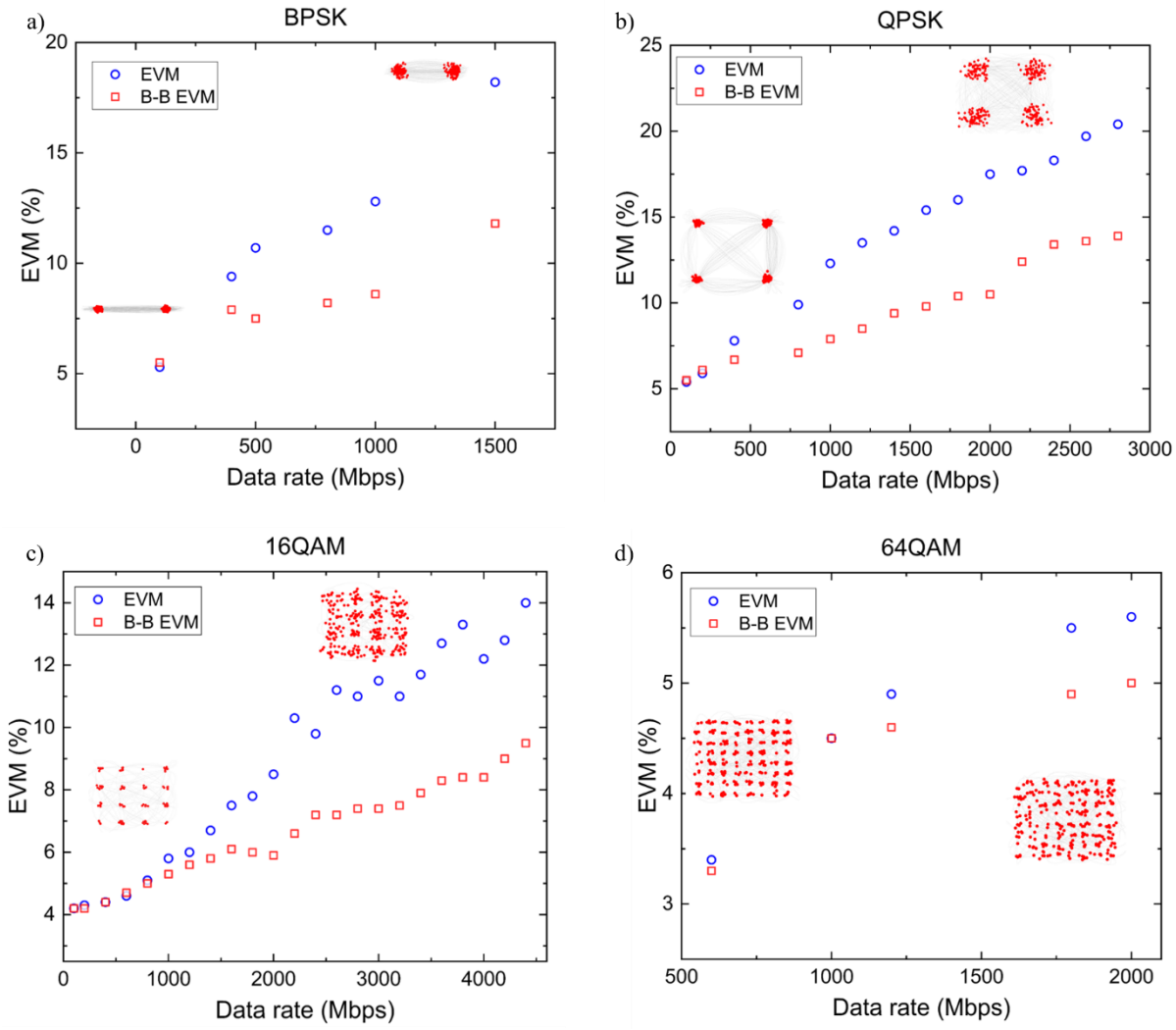

Figure 4-16 Measured values for EVM and B-B EVM for a) BPSK, b) QPSK, c) 16QAM and d) 64QAM.

The presented results concerning the glass dual mode laser are preliminary results. Additional characterizations should be performed on the generated carrier such as the short-term and long-term stabilities and the thermal dependency to complete this study. Moreover, as said in the beginning of this chapter, some extra work has to be performed on the design for high frequency generation. However, in chapter 3, we demonstrated that the characteristics of the generated carriers are independent from the frequency, and thus we expect a similar behavior at any frequency.

4.5 Future works

4.5.1 Short time prospect: Characterizing the lasers having a phase shift

To ensure a single mode operation of DFB lasers, a phase shift should be added in the waveguide. During this work, as it has been mentioned, a photolithography mask containing numerous waveguides with phase shifts with different dimensions have been designed and fabricated. However, due to lack of time, we couldn't characterize them. For that reason, one of the first future works should be the characterization of these devices.

4.5.2 Short-term prospect: Improving the ion diffusion model

In this work, we have used a diffusion model to calculate the effective refractive index of the ion-exchanged waveguides. In the end of the ion exchange process and to avoid breaking our sample, we wait for a duration of 210 s before cleaning it. Supposing a linear decrease of the temperature from 270 °C (the flash bath temperature) to the room temperature, simulations showed that during this time the effective refractive index of the waveguides decreases. A more accurate study should be performed to determine the real temperature curve during this step to be able to predict more accurately the effective refractive index of the waveguides. This study will also help to design photolithography masks for lasers emitting at precise wavelengths.

4.5.3 Short-term prospect: Terahertz imaging application

Using the fabricated lasers on glass, an electrical signal at 1.6 THz can be generated. THz radiations are attracting in medical and biological applications owing to THz sensitivity to the water content of tissues in addition to the fact that this imaging technique is non-invasive and harmless to the living organisms [71]. THz band is also interesting for security sensing thanks to the capacity to detect concealed weapons and target compounds such as explosives and drugs [72]. Our lasers have the capacity of generating THz carriers while having high power (optical output power for each laser is higher than 10 dBm). One of our prospects is the use of our lasers in THz imaging applications.

4.5.4 Medium-term prospect: Packaging the device

The generation of RF carriers by heterodyning two single mode lasers respecting the IEEE requirements in term of stability has been successfully achieved for the first time in this work. However, a residual frequency deviation in the order of 5 MHz / 90 min still exists. We suspect that this remaining deviation is caused by mechanical vibrations in the optical bench that induce a small difference in the repartition of the pump power in the arms of the Y-junction as the latter is multimode at the pump wavelength (980 nm). To study the feasibility of this hypothesis, three points have to be solved:

- Design single mode Y-junction at both the pump and the signal wavelength. This way we avoid the variation in the pump power repartition in the Y-junction arms.
- Use a pump setup in which all the components have compatible fibers. As during our work, we used a pump having a polarization maintaining fiber and a multiplexer having standards HI1060 and SMF28 fiber. The splice pump – multiplexer caused a lot of losses as the two fibers are not compatible. Moreover, this splice induced polarization problems at the pump wavelength.
- Connectorization of the system laser to the fiber and packaging the whole system to suppress any possible external vibrations.

4.5.5 Long-term prospect: co-integration of the pump setup

To suppress the losses induced by the fiber splices and connectors and the polarization problems, the best solution would be to co-integrate the pump diode and the glass lasers on the same wafer. Figure 4-17 illustrates the proposed design. The 980/1550 multiplexer should be designed on a photolithography mask, then fabricated on a passive glass by Ag^{+}/Na^{+} ion exchange. A semiconductor laser diode emitting at 980 nm is loaded on the passive glass. And the glass dual mode laser (or any other co-integrated design) fabricated on the active glass is loaded by chemical bonding on the passive glass.

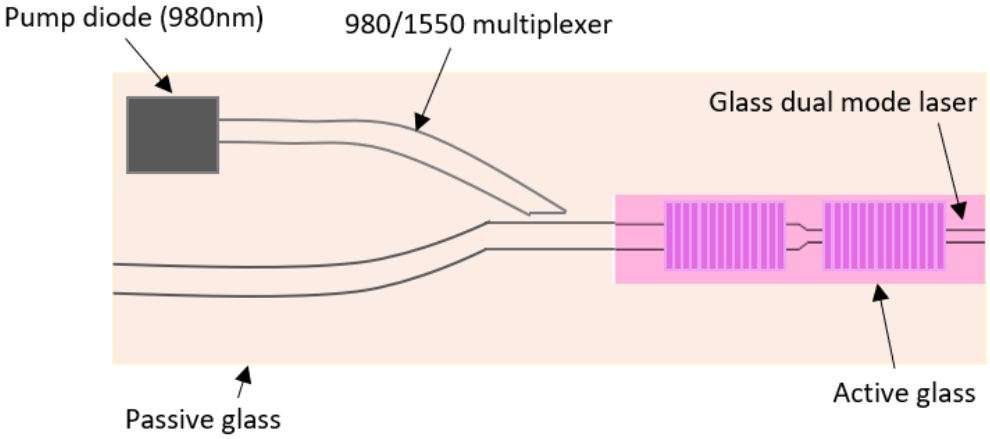

Figure 4-17 Co-integrated pump and signal setup.

4.6 Conclusion

To further enhance the stability of the generated carriers and to reduce the chip footprint, co-integrated designs have been introduced in this chapter. Three co-integrated designs have been presented: co-integrated lasers, Y-junction lasers and the dual mode laser.

Frequency deviations using the first two designs have been slightly reduced compared to that measured on the carriers generated by independent laser chips. A long-term deviation has been successfully performed using the Y-junction, and a deviation lower than 5 MHz over 90 minutes has been obtained. The possible sources of the residual deviation measured using the Y-junction have been investigated. The study showed that the thermal effects and pump power fluctuations are not the main contributors to the deviation. We expect that some vibrations are impacting on the repartition of the pump power in the branches of the Y-junction and thus inducing the frequency deviation.

Glass dual-mode laser has been introduced. The different ways to fabricate such lasers have been presented. A carrier at 6.1 GHz has been generated using the dual mode laser having its waveguide aperture widths w_1 = 7 µm and w_2 = 7.1 µm. Its linewidth is estimated to be 600 Hz. The generated carrier has been evaluated in RoF system by performing data transmission measurements. The measured EVM showed a significant improvement in the signal quality compared to all the signals generated using the other designs.

DFB lasers on glass proved their capacity to generate stable mm-wave carriers and transmitting data up to 4 Gbps. Table 4-3 summarizes all the measured EVM for the maximum reached data rate for different modulation formats. The carrier generated with Y-junction design proved to be resistive against external thermal fluctuations and to be stable. We expect that the remaining deviation can be reduced or neglected if the device is packaged. Additional characterizations should be performed for the dual mode laser to measure its deviation.

Design	Frequency	Data transmission			
		BPSK	QPSK	16QAM	64QAM
Co-integrated lasers	52 GHz	1200 Mbps 22.1 %	3000 Mbps 22.8 %	4000 Mbps 16.5 %	-
Y-junction	5.3 GHz	1500 Mbps 19.8 %	2800 Mbps 21.5 %	4000 Mbps 14.6 %	-
Dual mode laser	6.1 GHz	1500 Mbps 11.8 %	2800 Mbps 13.9 %	4400 Mbps 14 %	2000 Mbps 5 %

Table 4-3 Summary of all the data transmission measurement results using co-integrated designs.

General conclusion

In this manuscript, we detailed the works concerning the study of fabrication of DFB lasers on glass by Ag^+/Na^+ ion exchange. Using these lasers, different mm-wave carriers have been generated and they proved to be compliant with the IEEE standards for RoF systems.

The goal of our work was presented in the first chapter. We started by defining the figures of merit in RoF systems, such as the phase noise, the signal to noise ratio (SNR) and the stability of the generated carrier. Then, the most commonly used techniques for mm-wave generation have been listed. The advantages and disadvantages of each of them were highlighted. In our work, we chose to combine the ion-exchanged glass technology with the heterodyning of single mode lasers technique for its simplicity. For that, we presented briefly the previously fabricated glass single mode lasers. They have been fabricated during the works of Sylvain Blaize and Lionel Bastard in IMEP-LAHC laboratory. These lasers emitting few milliwatts of optical power around the 1534nm peak emission of erbium have an ultra-narrow linewidth which is attractive for RoF systems. The first goal of this work was defined in the end of the chapter as the fabrication of single mode lasers with an accurate control of the laser wavelength difference to adjust the possible generated frequencies. The second goal was the generation of stable mm-wave carrier that fulfills the standards in term of stability, to finish with the evaluation of the generated carriers in RoF systems.

In chapter two, the fabrication and the characterization of a DFB laser have been carried out. A DFB laser is composed of two elements, the amplifying medium and the feedback element. An in-house developed diffusion model has been used combined to the diffusion coefficients determined during the works of Bertrand Charlet in IMEP-LAHC to design our amplifiers on IOG1 co-doped Er/Yb glass. The fabricated amplifiers are single mode at the signal wavelength and they have a net gain of 4dB/cm. The feedback element in our DFB lasers is a Bragg grating. We used a process that was previously elaborated in the laboratory to start the study. Then, some optimizations in the process have been accomplished. After fixing all the required parameters for the amplifier and the grating, the first lasers have been fabricated and then connectorized. The characterized laser has a 7 µm aperture width, it emits at 1533.3 nm at 20 °C with a fiber coupled optical power of 41mW for 560 mW of pump optical power. The laser has a linewidth of 2 kHz and a RIN below -145 dB / Hz after 50 MHz.

Mm-wave generation was performed in chapter three. At first, the results of some simulations using the diffusion model used in chapter 2 were presented to show the capability of glass integrated technology in mm-wave and THz generation. Then, the accuracy of the fabrication process was studied by simulating the impact of each parameter fabrication tolerance on the possible generated frequency. The thermal sensitivity of the lasers has been measured equal to 1.49 GHz / °C. A similar behavior has been observed for the lasers at low (10 °C) and high (70 °C) temperatures. The first generated carrier at 54 GHz was obtained by thermally tuning the wavelengths of the two-independent free-running lasers emitting at the same wavelength installed on separate heat sinks. The generated carrier is as narrow as 10 kHz and it has a frequency deviation equal to 36 MHz / 7 s. Using this carrier data transmission have been performed for data rates up to 900 Mbps for BPSK and 1000 Mbps for QPSK formats respectively. The measured deviation corresponds to a variation of the relative temperature equal to $2.4x10^{-2}$ °C between the two lasers, which is lowest than the temperature controller's accuracy (0.1 °C) so, we suspected that the measured deviation is caused by the temperature controllers. For that, we did our study with a second configuration consisted of stopping the thermal control while letting the two lasers on separate heat sinks. For this configuration, we used lasers having distinct aperture widths in order to generate a carrier at 60.3 GHz. The measured deviation using this carrier was reduced to 10 MHz / 7 s. This result proves that, at first, the measured deviation was mostly caused by the thermal control. Data transmission using the carrier of this configuration were performed. Data rates up to 1500 Mbps for BPSK, 3000 Mbps for QPSK and 3000 Mbps for 16QAM have been reached. The 10 MHz/7s deviation corresponds to a relative temperature variation equal to 6.7×10^{-4} °C between the two lasers. Given that the two lasers are on two heat sinks, a slight thermal fluctuation can cause this deviation. That's why we decided to use a new configuration consisted of installing the two lasers on the same heat sink. Using this configuration, a deviation equal to 2 MHz/7s compliant with the IEEE standards was measured. The same behavior at different frequencies was measured. The frequency thermal sensitivity was measured to be $\approx$ 10.9 MHz/°C. The system evaluation was again conducted, improvements in the measured EVM values between 2 points and 7.5 points, 2 points and 6 points and 1.7 points and 3.7 points for BPSK, QPSK, and 16QAM modulations formats respectively have been measured.

In chapter four, three co-integrated designs for DFB lasers for mm-wave generation have been presented. The first design is the "co-integrated lasers" in which the two lasers are just separated by 127 µm. Using co-integrated lasers, carriers at frequencies between 5 GHz and 164 GHz have been generated. A deviation of 1.6 MHz / 14 s was measured for a carrier at 52 GHz. Data transmission have been done to prove that the generated carrier fulfills the standards. The second co-integrated design is the "asymmetric Y-junction". Using this design, the setup was notably simplified. The two

lasers are pumped using only one LD, and there is no need for the 3-dB coupler. Carriers at two frequencies were generated using this design, at 5.3GHz and at 36.5 GHz. Short-term and long-term deviations were measured to be 1.8 MHz/30s and < 5 MHz per 90 minutes. The frequency thermal sensitivity was measured to be 0.7 MHz/°C showing that this design is relatively immune to external thermal variations. Data transmission have been performed and data rates up to 1500 Mbps for BPSK, 2800 Mbps for QPSK and 4000 Mbps for 16QAM respectively have been reached. The third design is the glass dual mode laser. We presented the principal of the design and the preliminary results we already have. Using this design, a carrier at 6.1 GHz was generated and evaluated. Data transmission with rates up to 1500 Mbps for BPSK, 2800 Mbps for QPSK, 4400Mbps for 16QAM and 2000Mbps for 64QAM have been reached. Thermal behavior of this design should be studied, and the design should be adjusted to generate high frequencies.

Publications of the author

Journal articles

N. Arab, L. Bastard, J. Poëtte, J.-E. Broquin and B. Cabon, "Thermal Coupling Impact on MMW Carrier Generated using Two Free Running DFB Lasers on Glass", Optics Letters, vol. 43, no. 22, 2018

International Conferences

N. Arab, L. Bastard and J. Poëtte, "Co-integration of two DFB lasers on glass for millimeter-wave generation", Proc. SPIE 10106, Integrated Optics: Devices, Materials, and Technologies, Photonics West, Sna Francisco, 2017

N. Arab, L. Bastard, J. Poëtte and J.-E. Broquin, "Heterodyne Generation of Ultra-Narrow Millimeter-Wave Carriers with Er-doped glass integrated DFB lasers", ECIO, Valencia, 2018

N. Arab, L. Bastard, J. Poëtte, R. Horváth and J.-E. Broquin, "Tunability of millimeter wave carriers generated by optically mixing two DFB lasers on glass", 11th IEEE/IET International Symposium on Communication Systems, Networks and Digital Signal Processing, Budapest, 2018

R. Horvath, **N. Arab**, J. Poëtte, J.-F. Roux, L. Bastard and B. Cabon, "High bandwidth photoswitch for heterodyne detection of optically generated mmW signals using 1.5µm integrated glass lasers", in Microwave Photonics (MWP), 2018 International Topical Meeting, Toulouse, 2018

N. Arab, L. Bastard, D. Bucci, E. Ghibaudo, J.-E. Broquin and J. Poëtte, "Integrated optics DFB lasers on glass for high frequency generation", in Microwave Photonics (MWP), 2018 International Topical Meeting, Toulouse, 2018

N. Arab, L. Bastard, J. Poëtte and J.-E. Broquin, "Glass dual-mode laser for ultra-narrow radio frequency generation", Photonics West, San Francisco, 2019 (submitted)

National Conferences

N. Arab, L. Bastard et J. Poëtte, "Génération et modulation des signaux millimétriques avec des lasers DFB co-intégrés sur verre", Journée du Club Optique et Microondes (JCOM), Limoges, 2017

N. Arab, D. Bucci, E. Ghibaudo, J.-E. Broquin, L. Bastard et J. Poëtte, "Battement de lasers DFB co-intégrés sur verre pour la génération de porteuses millimétriques", Journées Nationales d'Optique Guidée (JNOG), Limoges, 2017

N. Arab, L. Bastard, J. Poëtte, J.E. Broquin, "Optique intégrée sur verre pour la génération de fréquences millimétriques", GDR Ondes, Nice, 2017

N. Arab, L. Bastard, J. Poëtte et J.-E. Broquin, “Lasers sur verre pour la génération de fréquences par hétérodynage“, Journée du Club Optique et Microondes (JCOM), Toulouse, 2018

N. Arab, D. Bucci, E. Ghibaudo, J.-E. Broquin, L. Bastard and J. Poëtte, “Lasers intégrés sur verre pour la génération de fréquences radio Optique Toulouse“, Toulouse, 2018

References

[1] "FIWIN5G," [Online]. Available: http://fiwin5g.eu/. [Accessed 13 2 2018].

[2] Cisco, "Cisco webpage," 6 6 2017. [Online]. Available: https://www.cisco.com/c/en/us/solutions/collateral/service-provider/visual-networking-index-vni/mobile-white-paper-c11-520862.html. [Accessed 13 2 2018].

[3] Q. Zhao and J. Li , "Rain attenuation in millimeter wave," in *Proceedings of the IEEE international Symposium*, 2006.

[4] R. J. Humpleman and P. A. Watson, "Investigation of attenuation by rainfall at 60GHz," in *Proceedings of the Institution of Electrical Engieneers*, 1978.

[5] J. Capmany and D. Novak, "Microwave photonics combines two worlds," *Nature Photonics*, vol. 1, no. 6, pp. 319-330, 2007.

[6] N. J. Gomes, M. Moran, A. Alphones, B. Cabon, J. E. Mitchell, C. Lethien,, "Radio-over-fiber transport for the support of wireless broadband services," *Journal of Optical Networking*, vol. 8, no. 2, pp. 156-178, 2009.

[7] [Online]. Available: http://www.konure.com/it/2014/03/electrical-power-over-fiber-optics.html. [Accessed 01 07 2018].

[8] S. Koenig, J. Antes, D. Lopez-Diaz, I. Kallfass, T. Zwick, C. Koos,W. Freude, and J. Leuthold, "High-Speed Wireless Bridge at 220 GHz Connecting Two Fiber-Optic Links Each Spanning up to 20 Km," in *Optical Fiber Communication Conference (OFC)*, 2012.

[9] R. Sambaraju, J. Herrera, J. Marti, D. Zibar, A. Caballero, J. B. Jensen,Idelfonso, and T. Monroy, "Up to 40 Gb/s Wireless Signal Generation and Demodulation in 75-110 GHz Band using Photonic Techniques," in *IEEE Topical Meeting on Microwave Photonics (MWP)*, 2010.

[10] "Attenuation by Atmospheric Gases," ITU-R Standard P.676-6, 2005.

[11] S. K. Yong and C. C. Chong, "An Overview of Multigigabit Wireless through Millimeter Wave Technology: Potentials and Technical Challenges," in *EURASIP J. Wireless Communaications and Networking*, 2007.

[12] "ECMA Standard ECMA-387. High Rate 60GHz PHY, MAC and PALs, 2nd edition.," 2010.

[13] "IEEE 802.15.06-0474-00-003c," *IEEE Computer Society*, 2009.

[14] F. C. Brendel, "Etude système de diode lasers à verrouillage de modes pour la radio-surfibre en bande millimétrique.," Université de Grenoble, Grenoble, 2014.

[15] Y. Matsui, H. Murai, S. Arahira, S. Kutsuzawa, and Y. Ogawa, "30GHz Bandwidth 1.55-μm Strain-Compensated InGaAlAs-InGaAsP MQW Laser," *IEEE Photonics Technology Letters,* vol. 9, pp. 25-27, 1997.

[16] Jianjun Yu et al., "Optical millimeter-wave generation or up-conversion using external modulators," *IEEE Photonics Technology Letters,* vol. 18, no. 1, pp. 265-267, 2006.

[17] T. Kuri, K. ichi Kitayama, and Y. Takahashi, "A single light-source configuration for full-duplex 60GHz band radio-over-fiber system," *IEEE trans. Microw. Tech.,* vol. 51, pp. 431-439, 2003.

[18] Janjun et al., "DWDM optical millimeter-wave generation for radio-over-fiber using an optical phase modulator and an optical interleaver," *IEEE Photonics Technology Letters,* vol. 18, no. 13, pp. 1418-1420, 2006.

[19] Guhua et al., "Optical generation and distribution of continuously tunable millimeter-wave signals using an optical phase modulator," *Journal of Lightwave Technology,* vol. 23, no. 9, pp. 2687-2695, 2005.

[20] A. Ng'oma, "Radio-over-Fibre Technology for broadband wireless communication systems," Eindhoven univeristy of technology, 2005.

[21] J. O'Reilley and P. Lane, "Remote delivery of Video Services Using mm-Waves and Optics," *Journal of Lightwave Technology,* vol. 12, pp. 369-375, 1994.

[22] P. Shen, N. Gomes, P. Davies, W. Shillue, P. Huggard and B. Ellison, "High-purity millimeter-wave photonic local oscillator genenration and delivery," in *International Topical Meeting on Microwave Photonics* , 2003.

[23] E. P. Martin, T. Shao, V. Vujicic, P. M. Anandarajah, C. Browning, R. Llorenyte and L. Barry, "25-Gb/s OFDM 60-GHz Radio Over Fiber System Based on a Gain Switeched Laser," *Journal of Lightwave Technology,* vol. 33, no. 8, pp. 1635 - 1643, 2015.

[24] X. S. Yao and L. Maleki, "Optoelectronic oscillator for photonic systems," *IEEE Journal of Quantum Electronics,* vol. 32, pp. 1141-1149, 1996.

[25] V. Auroux, R. Khayatzadeh, A. Fernandez and O. Llopis, "Génération millimétrique à 90 GHz à partir d'un oscillateur optoélectronique couplé à 30 GHz," in *20èmes Journées Nationales Micro-ondes,* Limoges, 2017.

[26] G. J. Foschini, L. J. Greenstein, and G. Vannucci, "Noncoherent detection of coherent lightwave signals corrupted by phase noise," *IEEE Trans. Commun,* vol. 36, pp. 306-314, 1988.

[27] F. Timofeev, S. Bennett, R. Griffin, P. Bayyel, A. Seeds, R. Wyatt, R. Kashyap and M. Robertson, "High spectral purity millimeter-wave modulated optical signal generation using fiber grating lasers," *Electronic Letter,* vol. 34, pp. 668-669, 1998.

[28] Braun, P. P., Grosskopf, G. and Rohde, D., "Optical millimeter-wave generation and transmission technologies for mobile communications, an overview," in *Microwave Systems Conference,* 1995.

[29] Gliese, U., Nielson, Torben Norkov, Brunn, Marlene, Christensen, E. Lintz, Stubkjaer, K. E., Lindergren, S. and Broberg, B., "A wideband heterodyne optical phase-locked loop for generation of 3-18 GHz microwave carriers," *Photonics Technology Letters,* vol. 4, no. 8, pp. 936-938, 1992.

[30] Thaniyavarn, Suwat, Abbas, Gregory L. and Dougherty, William A., "Millimeter-wave signal generation and control using optical heterodyne techniques and electro-optic devices," in *SPIE Microelectronic Interconnect and Integrated Processing,* San Jose, 1991.

[31] L. N. Langley et al., "Optical phase locked loop (OPLL) module for use as a 9 GHz source in phased array communications antennas.," in *International TopicalMeeting on Microwave Photonics,* 1998.

[32] I. Aldaya, G. Campuzano and G. Castanon, "Analysis of the modulation impairements in optical sideband injection locking for millimeter-wave signal generation," *Optics & Laser Technology,* vol. 56, pp. 167-176, 2014.

[33] G. Grosskopf, D. Rohde, R. Eggemann, S. Bauer, C. Bornholdt, M. Mohrle, and B. Sartorius, "Optical Millimeter-Wave Generation and Wireless Data Transmission Using a Dual-Mode Laser," *IEEE Photonics Technology Letters,* vol. 12, pp. 1692-1694, 2000.

[34] F. van Dijk, A. Enard, X. Buet, F. Lelarge, and G.-H. Duan, "Phase Noise Reduction of a Quantum Dash Mode-Locked Laser in a Millimeter-Wave Coupled Opto-Electronic Oscillator," *Journal of Lightwave Technology,* vol. 26, pp. 2789-2794, 2008.

[35] F. Brendel, J. Poëtte, B. Cabon, T. Zwick, F. van Dijk, F. Lelarge and A. Accard, "Chromatic Dispersion in 60 GHz Radio-Over-Fiber Networks Based on Mode-Locked Lasers," *Journal of Lightwave Technology,* vol. 29, pp. 3810-3816, 2011.

[36] X. Chen, J. Yao, and Z. Deng, , "Ultranarrow dual-transmission-band fiber Bragg grating filter and its application in a dual-wavelength single longitudinal-mode fiber ring laser," *Optics letters,* vol. 30, pp. 2068-2070, 2005.

[37] M. J. Fice, E. Rouvalis, F. van Dijk, A. Accard, F. Lelarge, C. C. Renaud, G. Carpintero, and A. J. Seeds, "146-GHz millimeter-wave radio-over-fiber photonic wireless transmission system," *Optics Express,* vol. 20, pp. 1769-1774, 2012.

[38] C. Zhang, S. Liang, H. Zhu, and W. Wang, "Widely tunable dual-mode distributed feedback laser fabricated by selective area growth technology integrated with Ti heatrers," *Optics Letters,* vol. 38, pp. 3050-3053, 2013.

[39] P. Hartmann, X. Qian, A. Wonfor, R. V. Pent and I. H. White, "1-20 GHz directly modulated radio over MMF link," in *Microwave Photonics,* 2005.

[40] S. Blaize, "Etude et réalisation d'un microlaser à contre-réaction répartie en optique intégrée sur verre.," INPG, Grenoble, 2001.

[41] L. Bastard, "Matrice de lasers à haute cohérence en optique intégrée sur verre," INPG, Grenoble, 2003.

[42] M. Casale, "Réalisation d'un laser DFB hybride sur substrat de verre," Université de Grenoble, Grenoble, 2014.

[43] D. L. Veasey, D. S. Funk, P. M. Peters, N. a. Sanford, G. E. Obarski, N. Fontaine, M. Young, A. P. Peskin, W.-C. Liu, S. Houde-Walter, and J. S. Hayden, "Yb/Er-codoped and Yb-doped waveguide lasers in phosphate glass," *Journal of Non-Crystalline Solids*, vol. 263, pp. 369-381, 2000.

[44] S. Blaize, L. Bastard, C. Cassagnetes, and J. Broquin, "Multiwavelengths DFB waveguide laser arrays in Yb-Er codoped phosphate glass substrate," *IEEE Photonics Technology Letters*, vol. 15, pp. 516-518, 2003.

[45] "IOG-1 Phosphate Laser Glass," SCHOTT AG, 2013. [Online]. Available: http://www.schott.com/d/advanced_optics/7dbb44af-30f8-4aec-868d-371de845d532/1.2/schott-iog-1-phosphate-laser-glass-may-2013-eng.pdf. [Accessed 13 2 2018].

[46] S. Miller, "Integrated Optics : An introduction," *The Bell System Technical Journal*, vol. 48, no. 7, pp. 2059-2069, 1969.

[47] J. Phalippou, "Veeres: Aspects théoriques," vol. 7, pp. AF3600-1, 2001.

[48] A. Bunde, K. Funke and M. D. Ingram, "Ionic glasses: History and challenges," *Solid state ionics*, vol. 105, pp. 1-13, 1998.

[49] Z. W.H., "The atomic arrangement in glass," *Journal of the American Chemical society*, vol. 54, no. 10, pp. 3841-3851, 1932.

[50] Hwang, B., Jiang, S., Luo, T. Le Neidre, L., Watson, J., Peyghambarian, N., Jiang, S. and Honkanen, S., "Characterization of cooperative upconversion and energy transfer of Er3+ and Yb3+/Er3+ doped phosphate glasses," in *Proc. SPIE 3622, Rare-Earth-Doped Materials and Devices III*, San Jose, California, 1999.

[51] Izawa, Tatsuo; Nakagome, Hiroshi, "Optical waveguide formed by electrically induced migration of ions in glass plates," *Applied Physics Letters*, vol. 21, no. 12, pp. 584-586, 1972.

[52] J.-E. Broquin, "Ion-exchanged Integrated devices," in *Photonics West*, San Jose, 2001.

[53] A. Lupascu, A. Kevorkian, T. Boudet, F. Saint-Andre´, D. Persegol, and M. Levy,, "Modeling ion exchange in glass with concentration-dependent diffusion coefficients and mobilities," *Optical Engineering*, vol. 35, no. 6, p. 1603, 1996.

[54] B. Charlet, "Etude et réalisation de sources laser impulsionnelles en optique intégrée sur verre: Application à la génération du supercontinuum," INPG, Grenoble, 2011.

[55] H. Ouslimani, "Intégration de lasers impulsionnels monofréquences sur verre phosphate dopé ytterbium," Université de Grenoble, Grenoble, 2014.

[56] G. Della Valle, S. Taccheo, G. Sorbello, E. Gianci, V. Foglietti and P. Laporta, "Compact high gain erbium-ytterbium doped waveguide amplifier fabricated by Ag-Na ion exchange.," *Electronic Letters,* vol. 42, no. 11, 2006.

[57] Hill, K.O., Malo, B., Bilodeau, F., Johnson, D.C. and Albert, J, "Bragg gratings fabricated in monomode photosensitive optical fiber by UV exposure through a phase mask," *Applied Physics Letters,* vol. 62, no. 10, pp. 1035-1037, 1993.

[58] Bastard L, Blaize S, Broquin J, "Glass integrated optics ultranarrow linewidth distributed feedback laser matrix for dense wavelength division multiplexing applications," *Optical Engineering,* vol. 42, no. 10, pp. 2800-2804, 2003.

[59] F. Gardillou, L. Bastard, and J.-E. Broquin, "Integrated optics bragg filters made by ion exchange and wafer bonding," *Applied Physics Letters,* vol. 89, no. 10, 2006.

[60] L. Bastard J-.E. Boquin, "Realization of a distributed phase shifted glass DFB laser," in *SPIE, Photonics West*, San Jose, 2005.

[61] S. Yliniemi, J. Albert, Q. Wang and S. Honkanen, "UV-exposed Bragg gratings for laser applications in silver-sodium ion-exchanged phospahte glass waveguides," *Optics Express,* vol. 14, no. 7, 2006.

[62] J. Beas, G. Castanon, I. Aldaya, A. Aragon-Zavala and G. Campuzano, "Millimeter-Wave Frequency Radio over Fiber Systems: A Survey," *IEEE Communications Surveys & Tutorials,* vol. 15, no. 4, pp. 1593-1619, 2013.

[63] al., Janjun at, "DWDM optical millimeter-wave generation for radio-over-fiber using an optical phase modulator and an optical interleaver," *IEEE Photonics Technology Letters,* vol. 18, no. 13, pp. 1418-1420, 2006.

[64] H. Chen, F. Babin, M. Leblanc and G. W. Schimn, "Widely tunable single-frequency erbium-doped fiber lasers.," *IEEE Photonics Technology Letters,* vol. 15, no. 2, pp. 185-187, 2003.

[65] S.Ventouras, S.A. Callaghan, I.Clark, A.Burges, G.Porter, J.R.Norbury, S.M. Feeny and S.Salous , "Introduction This is the final report for a study for OFCOM to investigate the current state and future bands above 60 GHz in terms of devices, systems, applications, sharing and regulations.," OFCOM, 2006.

[66] H. Shams, K. Balakier, M. J. Fice, L. Ponnampalam, C. S. Graham, C. C. Renaud, A. J. Seeds and F. van Dijk,, "Coherent frequency tuneable thz wireless signal generation using an optical phase lock loop system.," in *Microwave Photonics (MWP), 2017 International Topical Meeting*, 2017.

[67] S. E. Alavi, M.R.K Soltanian, I.S. Amiri, M. Khalily, A.S.M. Supa'at, and H. Ahmad, ",Towards 5G: A photonic based millimeter wave signal generation for applying in 5G access fronthaul," Nature, 2016.

[68] H. Shao, S. Keyvaninia, M. Vanwolleghem, G. Ducournau, X. Jiang, G. Morthier, J. F. Lampin and G. Roelkens, "Heterogeneously integrated III–V/silicon dual-mode distributed feedback laser array for terahertz generation," *Optics Letters,* vol. 39, no. 22, pp. 6403-6406, 2014.

[69] C. Graham, R. Gwilliam, and A. Seeds, "Nitrogen ion implanted InP based photo-switch," *Optics Express,* vol. 20, pp. 26696-26703, 2012.

[70] R. Horvath, J.F. Roux, J.L. Coutaz, J. Poëtte, B. Cabon and C. Graham, "Ultrafast InGaAs photoswitch for RF signal processing.," in *Optical Network Design and Modeling (ONDM)*, Budapest, 2017.

[71] C. Jansen et al., "Terahertz imaging: applications and perspectives," *Applied optics,* vol. 49, no. 10, p. E48, 2010.

[72] J. F. Frederici, B. Schulkin, F. Huang, D. Gale, R. Barat, F. Olivieira and D. Zimdars, "THz imaging and sensing for security applications—explosives, weapons and drugs," *Semiconductor Science and Technology,* vol. 20, no. 7, 2005.

[73] D. G. e. al., "19.7 A 79GHz binary phase-modulated continuous-wave radar transceiver with TX-to-RX spillover cancellation in 28nm CMOS," in *International Solid-State Circuits Conference*, 2015.

[74] F. D. Lucia, "Science and Technology in the Submillimeter Region," *Optics and Photonics news,* vol. 44, no. 8, 2003.

[75] R. Brown, W. Wild ans C. Cunningham, "ALMA - the Atacama large millimeter array.," *Advances in space research,* vol. 34, no. 3, pp. 555-559, 2004.

[76] G. Kervella, M. Chitoui, M. Lampini, R. Yannick, E. Vinet, D. Make, M.J. Fice, C.C. Renaud, G. Carpintero and F. van Dijik, "Monolithically integrated tuneable photonic source for the generation and modulation of millimetre-wave," in *Photonics Conference (IPC), 2014 IEEE*, 2014.

[77] F. Van Dijik et al., "Integrated InP heterodyne millimeter wave tarnsmitter," *IEEE Photonics Technology Letters,* vol. 26, no. 10, pp. 965-968, 2014.